

**APPLICATION SPECIFIC METAMATERIAL
STRUCTURES, DEVICES AND
COMPONENTS**

by

NISHANT SHANKHWAR
DEPARTMENT OF APPLIED PHYSICS

Submitted

in fulfilment of the requirements of the degree of

DOCTOR OF PHILOSOPHY

to the



DELHI TECHNOLOGICAL UNIVERSITY
DELHI 110042, INDIA
NOVEMBER, 2019

©DELHI TECHNOLOGICAL UNIVERSITY-2019
ALL RIGHTS RESERVED



DELHI TECHNOLOGICAL UNIVERSITY

CERTIFICATE

This is to certify that the Ph.D. thesis entitled “**APPLICATION SPECIFIC METAMATERIAL STRUCTURES, DEVICES AND COMPONENTS**” submitted to the Delhi Technological University, Delhi for the award of Doctor of Philosophy is based on the original research work carried out by me under the supervision of Prof. Ravindra Kumar Sinha and Dr. Yogita Kalra, Department of Applied Physics, Delhi Technological University, Delhi, India. It is further certified that the work embodied in this thesis has, neither partially nor fully, been submitted to any other university or institution for the award of any degree or diploma.

Nishant Shankhwar

Candidate

Enrolment No: 2K13/PHD/AP/03

Prof. Ravindra Kumar Sinha

(Supervisor)

Director, CSIR-CSIO, Chandigarh

Professor (*on lien*)

Department of Applied Physics

Delhi Technological University

Dr. Yogita Kalra

(Supervisor)

Assistant Professor

Department of Applied Physics

Delhi Technological University

Prof. Rinku Sharma

Head

Department of Applied Physics

Delhi Technological University

Dedicated to my parents for their love and support & to all my teachers for the knowledge and motivation I received from them.

Acknowledgements

This thesis is an outcome of 6 years of hard-work, which has been possible because of a constant support and encouragement from many people, towards whom, I would like to take the opportunity to express my gratitude.

First and foremost I express immense gratitude towards my supervisors, Prof. Ravindra Kumar Sinha and Dr. Yogita Kalra, for their enlightened guidance while dealing with scientific problems, towards the accomplishment of this work. I am thankful to them for their advices, knowledge augmenting discussions, quality enhancing inputs, constructive criticism and constant motivation. Above all, the research ethics I learnt from Prof. Sinha, shall always be a guiding light for me in choosing and practicing trues ways of science throughout my life and career.

Furthermore, I express reverence towards the Honorable Vice Chancellor, Delhi Technological University and Head, Department of Applied Physics, Delhi Technological University for providing the basic infrastructural facilities for carrying out the research work. I further place on record, obligation to SRC and DRC members – Professor S. C. Sharma (Chairman, DRC), Prof. Shyama Rath (External Expert), Prof. R. P. Sharma (External Expert), Prof. S. K. Sharma (External Expert), Dr. M. S. Mehata (Internal Expert) and Dr. Ajeet Kumar (Internal Expert) for taking their time serving in the committees and giving valuable suggestions on the thesis.

Additionally, I am sincerely grateful to Dr. Alexander Krasnok, Dr. Sergey Makaraov and Prof. Pavel Belov of the ITMO University, St. Petersburg, Russia and Prof. Qiang Li of the College of Optical Science and Engineering, Zhejiang University, Hangzhou, China for their collaboration in the research work and their valuable inputs in improving quality of the manuscripts.

I am deeply indebted to my family for always having faith in me and motivating me for perseverance during tough times. I am also thankful to my colleagues - Dr. Kamal Kishor, Dr. Than Singh Saini, Ritika Ranga, Reena Dalal, Pooja Chauhan, Dr. Rachna Sharma, Dr. Venus Dillu and Dr. Preeti Rani, for harboring a positive and progressive environment in the laboratory, and to my friends - Kamal Arora, Rahul Pandey, Jaya Madan, Vipin Dahiya, Sonia Tomar, Shubhanshi Sharma, Nisha Chaudhary, Prashant Karmakar and Harpreet Kaur, in the presence of whom, I stayed happy and exuberant despite all odds and disappointments.

Finally, I acknowledge the initiatives and support from the establishment of TIFAC-Centre of Relevance and Excellence in Fiber Optics and Optical Communi-

cation at Delhi Technological University (Formerly Delhi College of Engineering) Delhi, through the Mission REACH program of Technology Vision-2020 of the Government of India. I also acknowledge the support through Junior Research Fellowship awarded by University Grants Commission (India) under UGC-NET-JRF scheme, and the travel grant provided by SPIE- The international society for optics and photonics to attend Optics+Photonics 2017 in San Diego, USA.

Date:
Place:

Nishant Shankhwar

Abstract

This thesis presents a detailed account of the research work conducted by the author in the area of metamaterials which includes certain novel application-specific designs, as well as, a few unanticipated applications of the existing designs of metamaterials. In this work a broad spectrum of metamaterials ranging from positive to negative through zero refractive index have been explored and employed for useful applications.

An all-dielectric metasurface has been used to make high quality laser cavity by reducing the losses due to finite reflectivity. Besides high quality factor, the metasurface cavity has a compact design which improves its practicality. The metamaterial used here is a purely dielectric perfect reflector having near zero impedance. Secondly, a novel design of a lossy dielectric based metamaterial perfect absorber has been proposed whose working principle is substantially different from existing and commonly used metallic patch type metamaterials absorbers. Both these metamaterials lie in positive refractive index domain.

In the negative index domain, a novel design of split-nanotube based negative index metamaterial has been proposed which is an extruded version of a conventional split ring resonator. The split-nanotube has an upper hand over a split ring resonator in terms of both – strength of magnetic resonance and ease of fabrication on a substrate.

Between positive and negative index, lies the zero index region. The recent development of zero refractive index metamaterials (ZIMs) have unfolded multiple unprecedented properties leading to astonishing applications like wavefront engineering, electromagnetic cloaking, zero phase transfer, etc. This thesis includes two major works on zero index metamaterials, first is a zero index metamaterial based unidirectional nanoantenna which makes use of the well acknowledged dielectric rods-in-air type ZIM. The second one is a novel design of zero index metamaterial suitable for both TE and TM polarization which is an improvement over the existing ZIM designs which are suitable for only one type of polarization.

Metamaterials hold tremendous possibilities for broad range of applications from medicine to optical computing, communication, energy harvesting, defense, imaging, etc. In this research work almost all the types and domains of metamaterials have been ventured, explored & analyzed, and attempts have been made to suggest novel designs and applications.

List of publications

International Journals

1. **Nishant Shankhwar**, Ravindra Kumar Sinha, Yogita Kalra, Sergey Makarov, Alexander Krasnok, Pavel Belov, "High Quality Laser Cavity based on All-Dielectric Metasurfaces ", Photonic and Nanostructures- Fundamentals and Applications 24 (2017): 18-23.
2. **Nishant Shankhwar**, Yogita Kalra and Ravindra Kumar Sinha, "Split-nanotube based negative index metamaterial at mid infrared wavelengths ". Journal of Nanophotonics 11.2 (2017):026014.
3. **Nishant Shankhwar**, Yogita Kalra and Ravindra Kumar Sinha, "LiTaO₃ based metamaterial perfect absorber for terahertz spectrum", Superlattices and Microstructures, 111 (2017): 754-759 - Elsevier.
4. **Nishant Shankhwar**, Yogita Kalra and Ravindra Kumar Sinha, "All dielectric zero-index metamaterial for TE/TM polarization", Journal of Optics 20.11 (2018): 115101, IOP.
5. **Nishant Shankhwar**, Yogita Kalra, Qiang Li and Ravindra Kumar Sinha, "Zero-index metamaterial based all-dielectric nanoantenna." AIP Advances 9.3 (2019): 035115.

International conferences

1. **Nishant Shankhwar**, Ravindra Kumar Sinha, "Design of Near-field Superlens with silver multilayer in silicon host", Proceedings of International OSA Network of Students Asia 6, 10 -12 December 2014, Kharagpur, West Bengal , India.
2. **Nishant Shankhwar**, Ravindra Kumar Sinha, "Design and analysis of near perfect metamaterial reflector in visible range." Metamaterials, Metadevices, and Metasystems 2015. Vol. 9544. International Society for Optics and Photonics, 2015.

3. **Nishant Shankhwar**, Ravindra Kumar Sinha, Yogita Kalra, "Controlling the evanescent waves using metamaterials." *Metamaterials, Metadevices, and Metasystems 2016*. Vol. 9918. International Society for Optics and Photonics, 2016.
4. **Nishant Shankhwar**, Ravindra Kumar Sinha and Yogita Kalra, "Magnetic response of split-nanotube type metamaterial at near infrared frequency." *Frontiers in Optics*. Optical Society of America, 2016.
5. **Nishant Shankhwar**, Yogita Kalra, and Ravindra Kumar Sinha, "LiTaO₃ microcubes based metamaterial perfect absorber." *Metamaterials, Metadevices, and Metasystems 2017*. Vol. 10343. International Society for Optics and Photonics, 2017.
6. Shubhanshi Sharma, **Nishant Shankhwar**, Yogita Kalra, Ravindra Kumar Sinha, "Design and analysis of tip slotted square patch nano-antenna." *Metamaterials, Metadevices, and Metasystems 2017*. Vol. 10343. International Society for Optics and Photonics, 2017.
7. Sonia Tomar, **Nishant Shankhwar**, Yogita Kalra, Ravindra Kumar Sinha, "Plasmonic waveguides based optical AND gate." *Plasmonics: Design, Materials, Fabrication, Characterization, and Applications XV*. Vol. 10346. International Society for Optics and Photonics, 2017.
8. Reena Dalal, **Nishant Shankhwar**, Yogita Kalra, Ajeet Kumar, Ravindra Kumar Sinha, "All-dielectric cylindrical nanoantennas in the visible range." *Nanophotonic Materials XIV*. Vol.10344. International Society for Optics and Photonics, 2017.
9. **Nishant Shankhwar**, Ravindra Kumar Sinha and Yogita Kalra, "Magnetic response of split-nanotube type metamaterial at near infrared frequency." *Frontiers in Optics*. Optical Society of America, 2016.
10. **Nishant Shankhwar**, Yogita Kalra, Ravindra Kumar Sinha, "Dielectric veins type photonic crystal as a zero-index-metamaterial." *Frontiers in Optics*. Optical Society of America, 2017.
11. Parul Goyal, **Nishant Shankhwar**, Yogita Kalra, Ravindra Kumar Sinha, "Design of a cross structure nanoantenna." *AIP Conference Proceedings*. Vol. 2009. No. 1. AIP Publishing, 2018.
12. **Nishant Shankhwar**, Yogita Kalra, Ravindra Kumar Sinha, " All Dielectric Zero Index Metamaterial Based Beam Splitter", *AIP conference proceedings* Vol. 2009, for AMN-2018, 15-17 March 2018 in Jaypee Institute of Information Technology, Noida.

13. Nishant Shankhwar, Yogita Kalra, Ravindra Kumar Sinha, "Highly reflective broadband dielectric metasurface for terahertz applications", IEEE International Conference on Photonics & High Speed Optical Networks (ICPHON 2018), 12-13 April 2018, S. A. Engineering College, Chennai.
14. Parul Goyal, **Nishant Shankhwar**, Yogita Kalra, Ravindra Kumar Sinha, "Field enhancement in Victoria cross type nanoantenna", IEEE International Conference on Photonics & High Speed Optical Networks (ICPHON 2018), 12-13 April 2018, S. A. Engineering College, Chennai.
15. Parul Goyal, **Nishant Shankhwar**, Yogita Kalra, Ravindra Kumar Sinha, "Design and Analysis of a Polarization Independent Flower Shaped Nanoantenna", International Conference on Advances in Science & Technology (ICAST-2018), 04-05 May 2018, Swami Keshavananda Institute of Technology, Management and Gramothan, Jaipur.
16. Parul Goyal, **Nishant Shankhwar**, Yogita Kalra, "Design and analysis of a hollow bowtie nanoantenna." Plasmonics: Design, Materials, Fabrication, Characterization, and Applications XVI. Vol. 10722. International Society for Optics and Photonics, 2018.
17. **Nishant Shankhwar**, Yogita Kalra, Ravindra Kumar Sinha, "Dielectric zero-index metamaterial filled photonic crystal defect waveguide: design and analysis." Metamaterials, Metadevices, and Metasystems 2018. Vol. 10719. International Society for Optics and Photonics, 2018."
18. Ritika Ranga, **Nishant Shankhwar**, and Yogita Kalra. "Design and Analysis of Broadband Square Spiral Shaped Nanoantenna." Frontiers in Optics. Optical Society of America, 2018.
19. Parul Goyal, **Nishant Shankhwar**, and Yogita Kalra. "Near Field Enhancement in a Hollow Flower Shaped Nanoantenna." Laser Science. Optical Society of America, 2018.
20. **Nishant Shankhwar**, Yogita Kalra, and Ravindra Kumar Sinha. "Honeycomb photonic crystal as a zero index metamaterial." Laser Science. Optical Society of America, 2018.
21. **Nishant Shankhwar**, Ritika Ranga, Yogita Kalra and Ravindra Kumar Sinha, "Controlling the radiation pattern of a microstrip patch antenna using a checkerboard patterned metasurface." AIP Conference Proceedings. Vol. 2136. No. 1. AIP Publishing, 2019.
22. Ritika Ranga, **Nishant Shankhwar**, Yogita Kalra and Kamal Kishor, "Design of hexameric flower shaped nanoantenna for energy harvesting." AIP Conference Proceedings. Vol. 2136. No. 1. AIP Publishing, 2019.

23. **Nishant Shankwar**, Ritika Ranga, Yogita Kalra and Ravindra Kumar Sinha, "Dielectric ring based metamaterial perfect reflector." *Metamaterials, Metadevices, and Metasystems 2019*. Vol. 11080. International Society for Optics and Photonics, 2019.

List of Figures

1.1	(a) Circular magnetic field lines around a current carrying conductor; (b) force exerted by two parallel current carrying conductors on each other depending upon the direction of current flow in them; (c) the first electric motor invented by Faraday.	2
1.2	The electron cloud shifts according to the magnitude and direction of electromagnetic wave. Illustrated here, is the displacement of electron cloud throughout one complete cycle of oscillation of the electric field.	5
1.3	Qualitative variation of real and imaginary part of relative permittivity with respect to frequency for (a) dielectrics and (b) metals (assuming $\omega_0 = 0$)	7
1.4	Calculation of scattering cross section for a silicon sphere w.r.t wavelength of incident light	9
1.5	(a) Angular distribution of Rayleigh scattered light for different polarization; (b) Degree of polarization of scattered light for unpolarized incident light.	12
1.6	Unit cells of (a) real lattice and (b) reciprocal lattice.	13
1.7	Unit cells of (a) real lattice and (b) reciprocal lattice.	14
2.1	Classification on the basis of dimensions of inhomogeneity	17
2.2	Two types of metasurfaces	18
2.3	Two categories on the basis of constituent materials	18
2.4	Categorization on the basis of resonance	19
2.5	Refraction of light by positive, negative and zero index metamaterial	20
2.6	Schematic illustration of metal-dielectric layers based electric metamaterials for parallel and perpendicular polarization.	21
2.7	Dependence of (a) real and (b) imaginary part of effective permittivity on dielectric filling fraction for perpendicular polarization . . .	22
2.8	Dependence of (a) real and (b) imaginary part of effective permittivity on dielectric filling fraction for parallel polarization	23
2.9	An array of metal wires	24
2.10	Real and imaginary part of permittivity (a) pure silver and (b) wire mesh type metamaterial made up of silver wires	25
2.11	Evolution from a simple circular disc to double split ring resonator .	26

2.12	LCR equivalent circuit for single and double split ring resonator. . .	27
2.13	Effective magnetic permeability of an SRR	28
2.14	Goos Hanchen shift in case of, (a) positive index and (b) negative index metamaterials	29
2.15	Perfect lensing by a negative index metamaterial	30
2.16	Electromagnetic cloaking using zero index metamaterials.	31
2.17	Electromagnetic cloaking using zero index metamaterials.	32
3.1	(a) Schematic illustration of laser cavity based on all-dielectric metasurfaces. (b) Design of the first reflector. (c) Design of the second reflector based on a disordered metasurface.	36
3.2	Reflection and transmission taking place at the interface of air and a semi-infinite medium due to the impedance mismatch between the two media.	37
3.3	(a) Scattering cross-section vs wavelength for the silicon cylinder with diameter $D = 420$ nm and height $H = 525$ nm. Inset: geometric dimensions of the cylinder and the direction of incidence of the external wave; (b) real and imaginary parts of the effective permittivity $'\epsilon'$ and the effective permeability $'\mu'$; (c) real part of the effective impedance $'z'$ and imaginary part of the effective refractive index $'n'$	39
3.4	(a) Reflectance vs wavelength for first metasurface reflector. (b) Reflectance vs wavelength plot for second reflector.	40
3.5	(a) Distribution of the normalized electric field inside the cavity at $\lambda = 1500$ nm and (b) variation of normalized E^2 along the length of the cavity. (c) Quality factor and (d) threshold gain coefficient of Metamaterial Laser Cavity at different wavelength.	42
3.6	(a) Design of Bragg Cavity. (b) Reflectance for both Bragg mirrors, (c) quality factor and (d) threshold gain coefficient for the laser cavity at different wavelengths.	43
3.7	Optimization plots for geometrical parameters corresponding to 6 different values of refractive index of the surrounding medium (the color bar indicates reflectance R).	45
4.1	Two types of orientations of an SRR to be fabricated on a substrate by lithography: (a) shows strong response but is difficult to fabricate and (b) shows weak response but is easy to fabricate. . . .	48
4.2	(a) Schematic diagram of the proposed metamaterial made up of a two-dimensional array of split-nanotubes and nanowires and (b) three-dimensional unit cell used for numerical analysis.	49

4.3	(a) A split ring of a finite thickness with equivalent LCR circuit. (b) Cross-sectional view of a unit cell of the proposed metamaterial displaying all the geometrical and material parameters. (c) Variation of resonant wavelength with thickness t keeping l_x a constant. (d) Variation of S_{21} parameter with respect to wavelength showing a dip at the resonant wavelength	51
4.4	Contour plots of—(a) x component of \vec{J} and (b) z component of \vec{J} , flowing in the split-nanotube. Blue color indicates negative value and red color indicates positive value.	52
4.5	Effective material parameters obtained. Real part is shown in blue solid curve and imaginary part is shown in red dashed line.	53
4.6	Condition of negative refraction [21]	54
4.7	Contour plots of x-component of the electric field for—(a) Negative refraction as light travels from a wedge of proposed metamaterial. (b) Normal refraction in case of a similar positive index dielectric wedge	55
5.1	Different types of absorbers	58
5.2	Schematic illustration of two layers acting as perfect absorber	60
5.3	Refractive index of Lithium Tantalate between 60 and 100 μm	61
5.4	(a) Unit cell of the proposed metamaterial structure, (b) array of the LiTaO_3 cylinders over silver substrate.	62
5.5	Dependence of resonant wavelength on (a) the radius and (b) the aspect ratio. The blue solid curve represents equation 5.13 and markers represent discrete data obtained on computation	63
5.6	(a) absorbance vs aspect ratio curve (b) absorbance vs radius of the cylinder. These graphs show that absorbance is maximum for $a = 1.9$ and $r = 3.75 \mu\text{m}$	63
5.7	Absorption, scattering and extinction cross-section at different wavelengths with maxima at 88 μm . Inset: orientation of electric and magnetic fields with respect to the particle during calculation of the extinction cross section.	64
5.8	(Reflectance, transmittance and absorbance of an array of LiTaO_3 cylinders (a) with and (b) without including metal (silver) substrate. A small absorption peak shows that LiTaO_3 itself absorbs some amount of light in the absence of silver substrate.	65
5.9	Variation of absorbance with respect to angle of incidence. Absorbance remains greater than 0.9 upto 55°	66
5.10	(a) Distribution y component of magnetic field (color contours) and rotating electric field (arrows) in xz plane. (b) distribution of power loss density at 88 μm	66
5.11	A unit cell of metallic patch type metamaterial perfect absorber resonant at 88 μm , inspired from Hao et al. (2010) [33]	67

5.12	Comparison of the proposed the LiTaO ₃ absorber with the work of Hao et al. [33]	68
6.1	Fishnet metamaterial	71
6.2	A Dirac like dispersion in a negative zero positive index metamaterial	72
6.3	Photonic band structure of the ZIM. The inset shows the square shape of the array. The region around the Dirac point has been zoomed to show the linear dispersion in its neighborhood.	73
6.4	3D dispersion surfaces displaying the formation of Dirac cones . . .	74
6.5	Dispersion analysis of a rectangular waveguide indicates zero phase at the cut-off frequency ω_{10}	75
6.6	Illustration of how critical the r/a ratio is for Dirac like dispersion .	76
6.7	(a) Magnitude and phase of scattering parameter S_{21} . (b) Effective material parameters retrieved by s-parameter inversion	77
6.8	Demonstration of the capability of a homogeneous ZIM slab to generate highly directional beams of light. (a) Geometry of the slab with an embedded current line source, (b) Electric field distribution around it, and (c) farfield plot to display the amount power flow w.r.t. the azimuthal coordinate at 193.4 THz (1550 nm).	78
6.9	(a) Design of ZIM based nanoantenna. (b) radiation pattern of the emitter alone (left), and radiation pattern of the emitter with nanoantenna (right)	79
6.10	Directivity D in H plane - (a) Cartesian plot and (b) Polar plot. Directivity in E plane - (c) Cartesian plot and (d) Polar plot.	80
6.11	(Left) Dependence of required r/a ratio and normalized frequency (a/λ) on the refractive index of the chosen surrounding medium, (Right) Variation of periodicity of the rods with respect to the refractive index of the chosen surrounding medium.	81
6.12	Schematic illustration of the design of the nanoantenna showing various geometrical parameters	83
6.13	Variation of output field with respect to the gap parameter g . . .	83
7.1	Design of the proposed metamaterial (a) Unitcell, (b) two dimensional array	86
7.2	(a) TM mode Photonic band structure of proposed ZIM, (b) zoomed-in image of the band structure to get a better view of intersection of bands, (c) band structure in terms of 3D dispersion surfaces & (d) zoomed-in version of 3D surfaces of for closer look of the Dirac cone. (e)-(h) similar band plots for TE mode.	87
7.3	Distribution of normalized E_z and H_z at the triple degenerate Dirac point for TM and TE polarization respectively.	88

7.4	Calculation of effective material parameters by s-parameter inversion technique [89]. (a) Two dimensional unit cell used for s parameter calculation. Effective material parameters calculated for (a) TM and (b) TE polarizations. In both the cases ϵ , μ and n tend to zero at $1.55 \mu\text{m}$	89
7.5	Demonstration of normal emergence of light from a prizm of the proposed zero index metamaterial in TM and TE mode at $1.54 \mu\text{m}$	90

Contents

Certificate	i
Dedication	ii
Acknowledgements	iii
Abstract	v
List of publications	vii
List of figures	x
1 A few prerequisite concepts	1
1.1 Evolution of electrodynamics	1
1.2 Maxwell's equation	3
1.3 Origin of refractive index	4
1.4 Scattering	8
1.4.1 Mie Scattering	8
1.4.2 Rayleigh Scattering	10
1.5 Reciprocal lattice and Brillouin zone	13
2 Introduction to metamaterials	17
2.1 Classification of metamaterials	17
2.1.1 Classification on the basis of dimensions of inhomogeneity . .	17
2.1.2 Classification on the basis of constituent materials	18
2.1.3 Classification on the basis of resonance	19
2.1.4 Classification on the basis of refractive index	20
2.2 A few important and commonly used metamaterials	21
2.2.1 Metal dielectric layers	21
2.2.2 A periodic array of metallic wires	23
2.2.3 Split ring resonator - a magnetic meta-atom	25
2.3 A few interesting manifestations and applications of metamaterials .	29
2.3.1 Negative Goos-Hanchen shift	29
2.3.2 Perfect lensing	30

2.3.3	Electromagnetic cloaking using zero index metamaterials . . .	31
2.3.4	Wavefront engineering	31
3	All-dielectric metasurface perfect reflectors as cavity resonator	35
3.1	Introduction	35
3.2	Fundamental principle of perfect reflection	37
3.3	Design and numerical analysis of metasurface based cavity	39
3.4	Comparison with Bragg reflector based cavity	42
3.5	Effect of Substrate	44
3.6	Conclusion	44
4	Split-nanotube based negative index metamaterial for midinfrared wavelengths	47
4.1	Introduction	47
4.2	Design	49
4.3	Numerical Analysis and Results	52
4.4	Conclusion	55
5	All dielectric metamaterial perfect absorber for terahertz spectrum	57
5.1	Introduction	57
5.2	Fundamental principle of perfect absorption	59
5.3	Design and numerical analysis	61
5.4	Comparison with a metallic patch type metamaterial perfect absorber	67
5.5	Conclusion	68
6	An all-dielectric zero-index metamaterial based nanoantenna	69
6.1	Introduction	69
6.2	The fundamental concept of zero refractive index	71
6.2.1	Zero index metamaterial systems	71
6.2.2	Rectangular waveguide: A zero index system other than metamaterials	74
6.3	Design of zero index metamaterial	76
6.3.1	Calculation of effective material parameters	77
6.4	Principle of directional radiation by ZIM	77
6.5	Design and operation of ZIM nanoantenna	78
6.6	Effect of the surrounding material	81
6.7	Effect of the gap between ZIM and Bragg mirror	82
6.8	Conclusion	84
7	All dielectric zero index metamaterial for TE/TM polarization	85
7.1	Introduction	85
7.2	Design and Numerical Analysis	86

7.2.1	Calculation of band structure	86
7.2.2	Interpretation of fields	87
7.2.3	Calculation of effective parameters	89
7.2.4	Verification by Snell's Law	90
7.3	Result and Discussion	91
7.4	Conclusion	91
8	Summary and future scope	93

Chapter 1

A few prerequisite concepts

1.1 Evolution of electrodynamics

Nineteenth century witnessed a tremendous progress in Electromagnetism, prior to which, electricity and magnetism were not perceived as the two sides of the same coin, as they are today. It all started in 1820, when Hans Christian Ørsted demonstrated for the first time, that an electric current flowing in a wire generated a circulating magnetic field around it (figure 1.1(a)). In the following year, André-Marie Ampère took things further by showing that two parallel current carrying wires exert attractive or repulsive force on each other depending upon the direction of current in one with respect to the other (figure 1.1(b)). Besides, he also presented a theoretical explanation of the phenomenon and established a mathematical relation between the magnitude of the current flowing and the intensity of magnetic field generated. As the news about Ørsted's experiment reached Michael Faraday in the Royal Society, he immediately conceived the idea of a device that could harness the magnetic energy and furnish some mechanical work. This led to the invention of primordial electric motor by him in the year 1821 (figure 1.1(c)). Moreover, Faraday envisioned the possibility of realizing an absolutely reverse phenomenon. He ardently believed that symmetry was nature's innate property, hence, if electricity could produce magnetism, the vice-versa must be true as well. A series of painstaking experiments during next 10 years led to the discovery of electromagnetic induction in 1831. By this time, the coalition between electricity and magnetism had been established. Another significant milestone in this arena was set by James Clerk Maxwell, who established light as a manifestation of the principles of electrodynamics. He argued that a varying electric field generated a varying magnetic field which, in turn generated another varying electric field and the phenomenon perpetuated. He brilliantly condensed entire electromagnetic theory into four simple equations, now referred to as, Maxwell's Equation. These equations are the most generalized mathematical representations of the Gauss' Law for electricity and magnetism, the Faraday's Law and the Ampere's Circuital Law. He also introduced a significant correction

factor in the Ampere's law which facilitated the comprehension of electromagnetic waves.

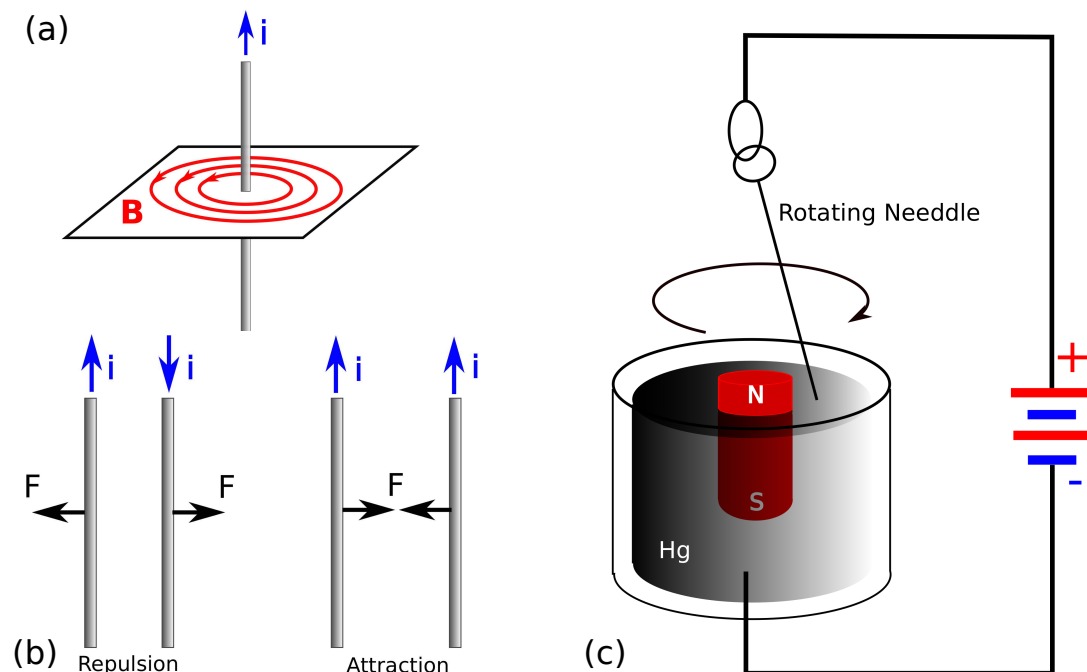


Figure 1.1: (a) Circular magnetic field lines around a current carrying conductor; (b) force exerted by two parallel current carrying conductors on each other depending upon the direction of current flow in them; (c) the first electric motor invented by Faraday.

Having physical and mathematical understanding of electromagnetic waves, made it easier to interpret their interaction with matter. The response of a material to an electromagnetic wave is linked to the redistribution of charges inside it, upon being subject to the electric and magnetic field of the wave. This knowledge about light-matter interactions led to the development of numerous devices working in different parts of spectrum, during the entire twentieth century. The transition period from the twentieth to the twenty first century, i.e. late 1990 and early 2000s, marked the beginning of a new era of electromagnetics by the advent of a special class of man-made materials called *Metamaterials*, which have several abnormal and unnatural properties like negative refraction, electromagnetic cloaking, perfect lensing, etc,. Their interesting and intriguing properties drew a lot of attention from the scientific community and for the same have been chosen by the author of this thesis as his area of research. The working of metamaterials is completely based on the principles of *Classical Electrodynamics*. An elaborate account of metamaterial is present in chapter 2, but for understanding them and this research work, one needs a few basic concepts in hand. This chapter presents

all those fundamental principles of electrodynamics which are needed as a prerequisite for efficient comprehension of advanced concepts spread throughout the rest of the thesis. It includes Maxwell's equations, the origin of refractive index with detailed account of its dispersive nature, two main types of scatterings– Mie and Rayleigh scattering and the concept of reciprocal lattices and Brillouin zones. Keeping these in mind, understanding the metamaterials and the work proposed in the thesis becomes easy.

1.2 Maxwell's equation

Maxwell's equations are a brilliant example of unification and generalization. Entire electrodynamics is packed into a simple set these four mathematical equations. Below are the different variants of Maxwell's equations subject to certain conditions.

Differential Form

$$\nabla \cdot \mathbf{E} = \rho/\epsilon \quad (1.1)$$

$$\nabla \cdot \mathbf{B} = 0 \quad (1.2)$$

$$\nabla \times \mathbf{E} = -\frac{\partial \mathbf{B}}{\partial t} \quad (1.3)$$

$$\nabla \times \mathbf{B} = \mu \mathbf{J}_s + \mu\epsilon \frac{\partial \mathbf{E}}{\partial t} \quad (1.4)$$

Integral Form

$$\oiint \mathbf{D} \cdot d\mathbf{s} = \iiint \rho dv \quad (1.5)$$

$$\oiint \mathbf{B} \cdot d\mathbf{s} = 0 \quad (1.6)$$

$$\oint \mathbf{E} \cdot d\mathbf{l} = -\frac{\partial}{\partial t} \iint \mathbf{B} \cdot d\mathbf{s} \quad (1.7)$$

$$\oint \mathbf{B} \cdot d\mathbf{l} = \mu \iint \mathbf{J}_s \cdot d\mathbf{s} + \mu\epsilon \frac{\partial}{\partial t} \iint \mathbf{E} \cdot d\mathbf{s} \quad (1.8)$$

Special Cases

Static field assumption: On assuming the fields to be invariant with time, i.e. $\partial/\partial t = 0$, equations 1.1 - 1.4 reduce down to

$$\nabla \cdot \mathbf{E} = \rho/\epsilon \quad (1.9)$$

$$\nabla \cdot \mathbf{B} = 0 \quad (1.10)$$

$$\nabla \times \mathbf{E} = 0 \quad (1.11)$$

$$\nabla \times \mathbf{B} = \mu \mathbf{J}_s \quad (1.12)$$

Time harmonic field assumption: On assuming the time-harmonic variation, i.e. field varying as $e^{j\omega t}$ with respect to time, $\partial/\partial t$ can be replaced by $j\omega$ and equations 1.1 - 1.4 reduce down to

$$\nabla \cdot \mathbf{E} = \rho/\epsilon \quad (1.13)$$

$$\nabla \cdot \mathbf{B} = 0 \quad (1.14)$$

$$\nabla \times \mathbf{E} = -j\omega\mathbf{B} \quad (1.15)$$

$$\nabla \times \mathbf{B} = \mu\mathbf{J}_s + \mu\epsilon j\omega\mathbf{E} \quad (1.16)$$

Electromagnetic wave propagation is possible because of an interplay of the equations 1.3 and 1.4, where, varying electric field produces varying magnetic field, which in turn produces varying electric field and the phenomenon perpetuates. The electric permittivity and magnetic permeability offered by different materials depend upon light-matter interaction. The next section throws light on this and explains the cause of refractive index.

1.3 Origin of refractive index

Refractive index offered by a material depends upon how its atoms interact with light which further depends upon how strongly the electrons are bound to the atoms. Different materials have different values of refractive index because the strength by which the electrons are bound to nucleus is different in each one of them. Moreover, for a particular material, refractive index is a strong function of wavelength of incident light, specifically in the optical region [28]. A rigorous analysis of dependence of refractive index on the material specific intrinsic parameters and the wavelength of the incident light is given below.

Let a given medium be exposed to an x polarized light. The electric field associated with the electromagnetic wave is

$$\mathbf{E} = \hat{\mathbf{x}}E_0\cos(kz - \omega t) \quad (1.17)$$

The electric field causes the electron cloud to get displaced opposite to the direction of electric field vector (as shown in figure 1.2). The displacement (say \mathbf{x}) of center of the electron cloud with respect to the nucleus is given by the solution of the differential equation

$$m\frac{d^2\mathbf{x}}{dt^2} + k_0\mathbf{x} = -q\mathbf{E} \quad (1.18)$$

or

$$\frac{d^2\mathbf{x}}{dt^2} + \omega_0^2\mathbf{x} = -\frac{q\mathbf{E}}{m} \quad (1.19)$$

where $-q$ and m are the charge and mass of an electron, k_0 is the restoring force constant and $\omega_0 = \sqrt{k_0/m}$ is the resonant frequency. On solving equation 1.18, we get,

$$\mathbf{x} = -\frac{q\mathbf{E}}{m(\omega_0^2 - \omega^2)} \quad (1.20)$$

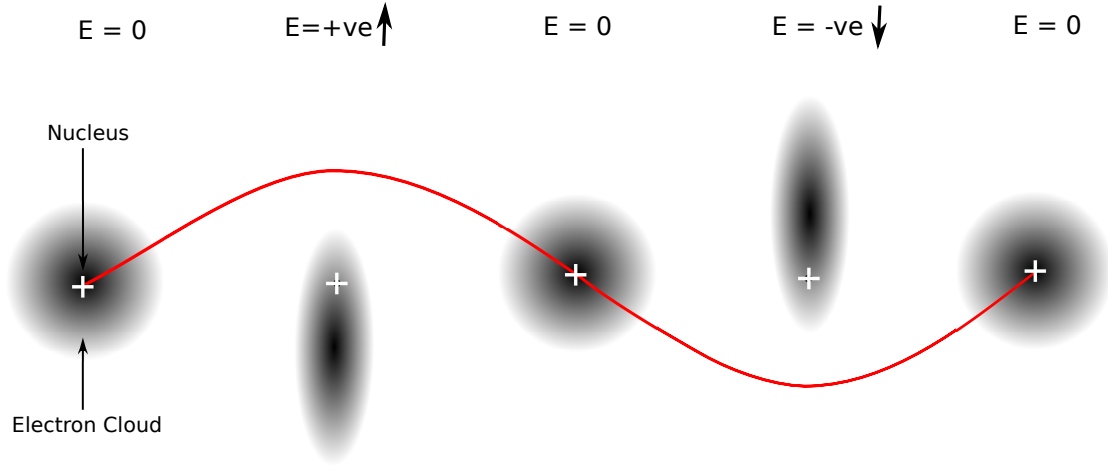


Figure 1.2: The electron cloud shifts according to the magnitude and direction of electromagnetic wave. Illustrated here, is the displacement of electron cloud throughout one complete cycle of oscillation of the electric field.

If there are N electrons per unit volume, then the polarization \mathbf{P} induced in the medium by electric field \mathbf{E} is given by

$$\mathbf{P} = -Nq\mathbf{x} \quad (1.21)$$

$$= \frac{Nq^2}{m(\omega_0^2 - \omega^2)}\mathbf{E} \quad (1.22)$$

$$= \epsilon_0\chi\mathbf{E} \quad (1.23)$$

where

$$\chi = \frac{Nq^2}{m\epsilon_0(\omega_0^2 - \omega^2)} \quad (1.24)$$

is the electric susceptibility and ϵ_0 is the permittivity of free space. Hence the permittivity of the medium is given by

$$\epsilon = \epsilon_0 + \epsilon_0\chi \quad (1.25)$$

$$= \epsilon_0(1 + \chi) = \epsilon_0\epsilon_r \quad (1.26)$$

where ϵ_r is the relative permittivity of the medium given by

$$\epsilon_r = 1 + \chi = 1 + \frac{Nq^2}{m\epsilon_0(\omega_0^2 - \omega^2)} \quad (1.27)$$

Now, it is known that relative permittivity is the square of refractive index,

hence, equation 1.27 can be written as

$$n^2 = 1 + \chi = 1 + \frac{Nq^2}{m\epsilon_0\omega_0^2} \left(1 - \frac{\omega^2}{\omega_0^2}\right)^{-1} \quad (1.28)$$

$$\approx 1 + \frac{Nq^2}{m\epsilon_0\omega_0^2} \left(1 + \frac{\omega^2}{\omega_0^2}\right) \quad (1.29)$$

$$\approx 1 + \frac{Nq^2}{m\epsilon_0\omega_0^2} + \frac{Nq^2}{m\epsilon_0\omega_0^4} \frac{4\pi^2 c^2}{\lambda_0^2} \quad (1.30)$$

$$= A + \frac{B}{\lambda_0^2} \quad (1.31)$$

which is the well known *Cauchy's Formula*. In case of metals, the electrons are free and there is no restoring force acting on them. Hence, equation 1.27 is reduced to

$$n^2 = 1 - \frac{Nq^2}{m\epsilon_0\omega^2} \quad (1.32)$$

$$= 1 - \frac{\omega_p^2}{\omega^2} \quad (1.33)$$

where

$$\omega_p = \sqrt{\frac{Nq^2}{m\epsilon_0}} \quad (1.34)$$

is the plasma frequency of the metal. For $\omega < \omega_p$ refractive index is imaginary which is the reason for ohmic loss associated with metals. Above plasma frequency ($\omega > \omega_p$) refractive index is real and metals behave like a dielectric.

It should be noted that, in the above analysis the damping force has not been considered. Considering the damping factor is necessary because damping factor does become significant in a certain region of spectrum. For example, silicon is a lossy dielectric in visible region but is practically lossless in infrared (eg. 1550 nm) and beyond. Hence, in a more realistic perception, equation 1.18 should be written as,

$$m \frac{d^2 \mathbf{x}}{dt^2} + \Gamma \frac{d\mathbf{x}}{dt} + k_0 \mathbf{x} = -q\mathbf{E} \quad (1.35)$$

and equation 1.19 becomes

$$\frac{d^2 \mathbf{x}}{dt^2} + 2K \frac{d\mathbf{x}}{dt} + \omega_0^2 \mathbf{x} = -\frac{q\mathbf{E}}{m} \quad (1.36)$$

Solving equation 1.36 the accurate expressions for polarization, susceptibility and relative permittivity, inclusive of damping factor are obtained as,

$$\mathbf{P} = \frac{Nq^2}{m(\omega_0^2 - \omega^2 - 2iK\omega)} \mathbf{E}, \quad (1.37)$$

$$\chi = \frac{Nq^2}{m\epsilon_0(\omega_0^2 - \omega^2 - 2iK\omega)}, \quad (1.38)$$

$$(1.39)$$

and

$$\epsilon_r = 1 + \frac{Nq^2}{m\epsilon_0(\omega_0^2 - \omega^2 - 2iK\omega)} \quad (1.40)$$

It can be noticed that the relative permittivity is complex in nature which implies that the refractive index is complex. Let the complex refractive index be represented as

$$n = \eta + i\kappa \quad (1.41)$$

Then,

$$n^2 = \epsilon_r = (\eta + i\kappa)^2 = \eta^2 - \kappa^2 + 2i\eta\kappa \quad (1.42)$$

On comparing equations 1.40 and 1.42 we get,

$$(\eta + i\kappa)^2 = 1 + \frac{Nq^2}{m\epsilon_0(\omega_0^2 - \omega^2 - 2iK\omega)} \quad (1.43)$$

$$= 1 + \frac{Nq^2(\omega_0^2 - \omega^2 + 2iK\omega)}{m\epsilon_0(\omega_0^2 - \omega^2 - 2iK\omega)(\omega_0^2 - \omega^2 + 2iK\omega)} \quad (1.44)$$

or

$$\eta^2 - \kappa^2 = 1 + \frac{Nq^2(\omega_0^2 - \omega^2)}{m\epsilon_0[(\omega_0^2 - \omega^2)^2 + 4K^2\omega^2]} \quad (1.45)$$

and

$$2\eta\kappa = \frac{Nq^2(2K\omega)}{m\epsilon_0[(\omega_0^2 - \omega^2)^2 + 4K^2\omega^2]} \quad (1.46)$$

Figure 1.3 shows the qualitative variation of real and imaginary part of relative

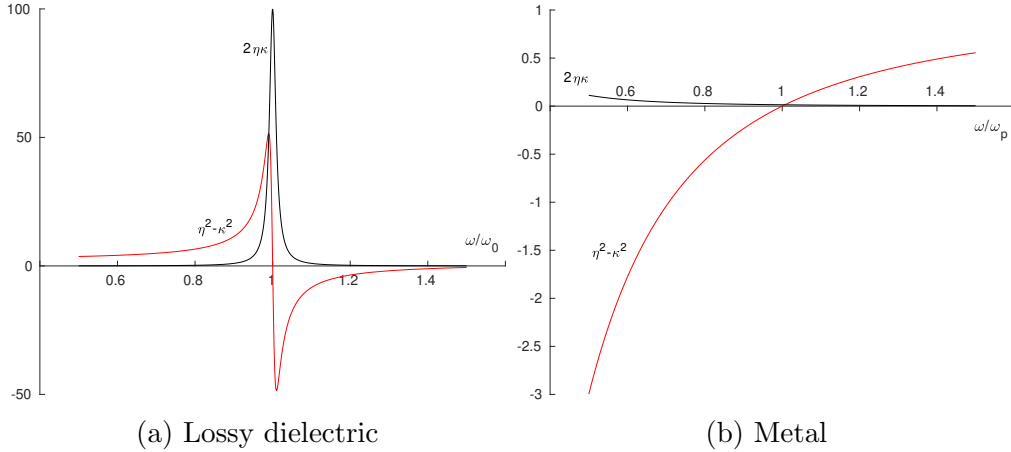


Figure 1.3: Qualitative variation of real and imaginary part of relative permittivity with respect to frequency for (a) dielectrics and (b) metals (assuming $\omega_0 = 0$)

permittivity with respect to frequency for both - dielectrics and metals. Since metals have free electrons, resonant frequency $\omega_0 = 0$. The x-axis of the graph has

been normalized with respect to resonant frequency ω_0 in figure 1.3a and plasma frequency ω_p in figure 1.3b. Below the plasma frequency, $\eta^2 - \kappa^2$ is negative and $2\eta\kappa$ is significantly high, which accounts for the highly reflective and absorptive nature of metals. Above plasma frequency, as $\eta^2 - \kappa^2$ becomes positive, thus, metals begin to acquire dielectric like properties of wave propagation. Additionally, the value of $2\eta\kappa$ also descend to extremely low values which in turn reduces absorption losses. Hence, for $\omega > \omega_p$ metals become transparent to em waves.

1.4 Scattering

1.4.1 Mie Scattering

Scattering of light by particles of size comparable to the wavelength is referred to as Mie scattering, named after Gustav Mie who derived the solution of Maxwell's equations for such a situation in 1908. An absolutely independent study of scattering of light by dielectric spheres was also performed by Ludvig Lorenz. Mie solutions accurately describe the distribution of electric and magnetic field inside and outside the particle. Accurate analytical solution exist for spherical particles which demonstrate the dependence of strength of scattering upon the particles' size and permittivity. A particular particle exhibits strongest scattering at certain values of wavelength (Mie resonance). Some important analytical results of Mie theory for a spherical particle are shown below [9]

Coefficients of field inside the particle:

$$c_n = \frac{\mu_1 j_n(x) [x h_n^{(1)}(x)]' - \mu_1 h_n^{(1)}(x) [x j_n(x)]'}{\mu_1 j_n(mx) [x h_n^{(1)}(x)]' - \mu h_n^{(1)}(x) [m x j_n(mx)]'} \quad (1.47)$$

$$d_n = \frac{\mu_1 m j_n(x) [x h_n^{(1)}(x)]' - \mu_1 m h_n^{(1)}(x) [x j_n(x)]'}{\mu m^2 j_n(mx) [x h_n^{(1)}(x)]' - \mu_1 h_n^{(1)}(x) [m x j_n(mx)]'} \quad (1.48)$$

Coefficients of scattered field:

$$a_n = \frac{\mu m^2 j_n(mx) [x j_n(x)]' - \mu_1 j_n(x) [m x j_n(mx)]'}{\mu m^2 j_n(mx) [x h_n^{(1)}(x)]' - \mu_1 h_n^{(1)}(x) [m x j_n(mx)]'} \quad (1.49)$$

$$b_n = \frac{\mu_1 j_n(mx) [x j_n(x)]' - \mu j_n(x) [m x j_n(mx)]'}{\mu_1 j_n(mx) [x h_n^{(1)}(x)]' - \mu h_n^{(1)}(x) [m x j_n(mx)]'} \quad (1.50)$$

Here, $m = N_1/N$ is the ratio of the refractive index of the particle with respect to that of the surrounding; μ_1 and μ are the relative permeabilities of the particle and the surrounding medium respectively; $x = 2\pi N a / \lambda$; and j_n & $h_n^{(1)}$ are Bessel function and Hankel function of the first kind respectively. The scattering coefficients can be written in simpler version using Riccati-Bessel functions and

assuming $\mu_1 = \mu$, as

$$a_n = \frac{m\psi_n(mx)\psi'_n(x) - \psi_n(x)\psi'(mx)}{m\psi_n(mx)\xi'_n(x) - \xi_n(x)\psi'(mx)} \quad (1.51)$$

$$b_n = \frac{\psi_n(mx)\psi'_n(x) - m\psi_n(x)\psi'(mx)}{\psi_n(mx)\xi'_n(x) - m\xi_n(x)\psi'(mx)} \quad (1.52)$$

where

$$\psi_n(\rho) = \rho j_n(\rho) \quad (1.53)$$

$$\xi_n(\rho) = \rho h_n^{(1)}(\rho) \quad (1.54)$$

are the Riccati-Bessel functions. Using these coefficients, the scattering cross-section C_{sca} , the extinction cross section C_{ext} and the absorption cross-section C_{abs} can be calculated as

$$C_{sca} = \frac{2\pi}{k^2} \sum_{n=1}^{\infty} (2n+1)(|a_n|^2 + |b_n|^2) \quad (1.55)$$

$$C_{ext} = \frac{2\pi}{k^2} \sum_{n=1}^{\infty} (2n+1)Re\{a_n + b_n\} \quad (1.56)$$

$$C_{abs} = C_{ext} - C_{sca} \quad (1.57)$$

where k is the wave vector.

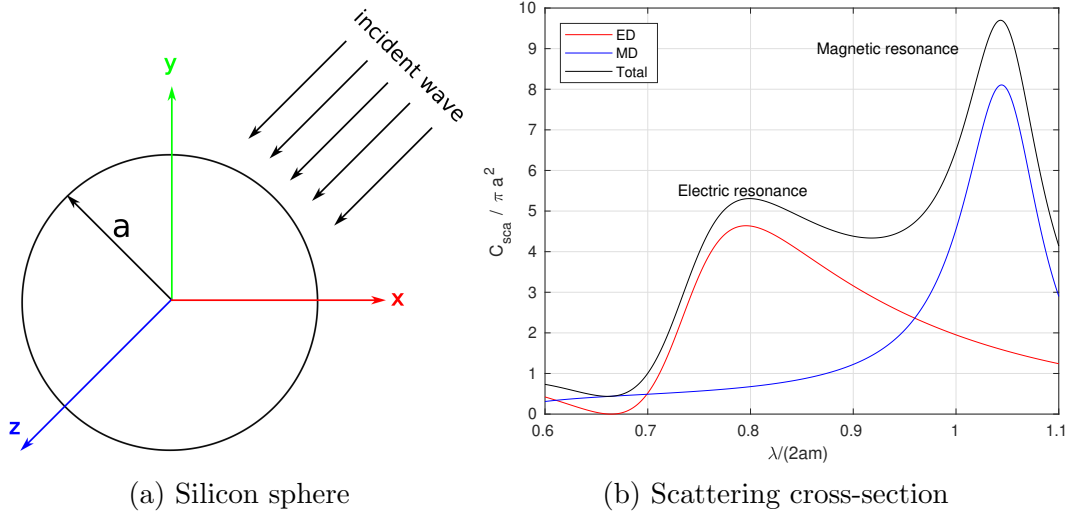


Figure 1.4: Calculation of scattering cross section for a silicon sphere w.r.t wavelength of incident light

Figure 1.4b shows the scattering cross-section for silicon sphere of radius a and refractive index $m = 3.5$, calculated using above mentioned formulae. It should

be noted that the first resonance peak appears at $\lambda/(2am) = 1.04$, which means that the particle resonates at $\lambda \approx 2am$. In other words, for resonance to occur, the wavelength inside the particle should be approximately equal to the diameter of the particle. Second peak is obtained at $\lambda/(2am) = 0.80$.

Calculation of field distribution inside the particles shows that the first resonance corresponds to a magnetic dipole mode while at second resonance it is always an electric dipole mode.

1.4.2 Rayleigh Scattering

Scattering of light by particles very small in size compared to the incident wavelength was first studied by Lord Rayleigh (John William Strutt) in 1871, about three decades prior to Gustav Mie's explanation (Mie theory) for the various colors scattered by colloidal solution of gold particles in water. Rayleigh, in his derivation did not include the absorption of light by particle and focused only on the scattering. However, Mie considered both the phenomena because adsorption spectrum played a pivotal role in deciding the color of the colloidal solution. It should be noted that Rayleigh scattering can be considered as a special case of Mie scattering, when incident wavelength is very larger compared to particle size. For qualitative analysis of Rayleigh scattering, let us expand the Riccati-Bessel functions to first few terms as

$$\begin{aligned}
 \psi_1(\rho) &\simeq \frac{\rho^2}{3} - \frac{\rho^4}{30} \\
 \psi_1'(\rho) &\simeq \frac{2\rho^2}{3} - \frac{\rho^4}{30} \\
 \xi_1(\rho) &\simeq -\frac{i}{\rho} - \frac{i\rho}{2} + \frac{\rho^2}{3} \\
 \xi_1'(\rho) &\simeq \frac{i}{\rho^2} - \frac{i}{2} + \frac{2\rho}{3} \\
 \psi_2(\rho) &\simeq \frac{\rho^2}{15} \\
 \psi_2'(\rho) &\simeq \frac{\rho^2}{5} \\
 \xi_2(\rho) &\simeq -\frac{i3}{\rho^2} \\
 \xi_2'(\rho) &\simeq \frac{i6}{\rho^3}
 \end{aligned} \tag{1.58}$$

where symbols have their usual meaning. Using these formulae in equations 1.51 & 1.52 the scattering coefficients accurate to sixth power of x (i.e. x^6) can be obtained as

$$\begin{aligned}
 a_1 &= -\frac{i2x^3(m^2-1)}{3(m^2+1)} - \frac{i2x^5(m^2-2)(m^2-1)}{5(m^2+2)^2} \\
 &\quad + \frac{4x^6(m^2-1)}{9(m^2+2)^2} + O(x^7) \\
 b_1 &= -\frac{ix^5}{45}(m^2-1) + O(x^7) \\
 a_2 &= -\frac{ix^5}{15} \frac{m^2-1}{2m^2+3} + O(x^7) \\
 b_2 &= O(x^7)
 \end{aligned} \tag{1.59}$$

where we have taken the permeability of the sphere to be equal to that of the surrounding medium. Assuming $|m|x \ll 1$ (i.e. size of the sphere is very small compared to wavelength) we get,

$$a_1 = -\frac{i2x^3(m^2-1)}{3(m^2+2)} \tag{1.60}$$

and $|b_1| \ll |a_1|$.

For an unpolarized incident light of irradiance I_i , the irradiance of scattered light I_s is given by

$$I_s = \frac{8\pi^4 N a^6}{\lambda^4 r^2} \left| \frac{m^2-1}{m^2+2} \right|^2 (1 + \cos^2\theta) I_i \tag{1.61}$$

which means that if the particle is sufficiently small compared to the wavelength of light, the irradiance of the scattered light is inversely proportional to λ^4 and is independent of the shape of the particle. Moreover, the degree of polarization of the scattered light strongly depends on the scattering angle θ . Equation 1.61 is true for unpolarized incident light, but for a polarized incident light the ratio of the scattered to the incident irradiance (I_s/I_i) is given for,

polarization parallel to the scattering plane, as,

$$i_{\parallel} = \frac{9|a_1|^2}{4k^2 r^2} \cos^2\theta, \tag{1.62}$$

polarization perpendicular to the scattering plane, as,

$$i_{\perp} = \frac{9|a_1|^2}{4k^2 r^2}, \tag{1.63}$$

In this way, irradiance for unpolarized incident light becomes,

$$i = \frac{1}{2}(i_{\parallel} + i_{\perp}) \tag{1.64}$$

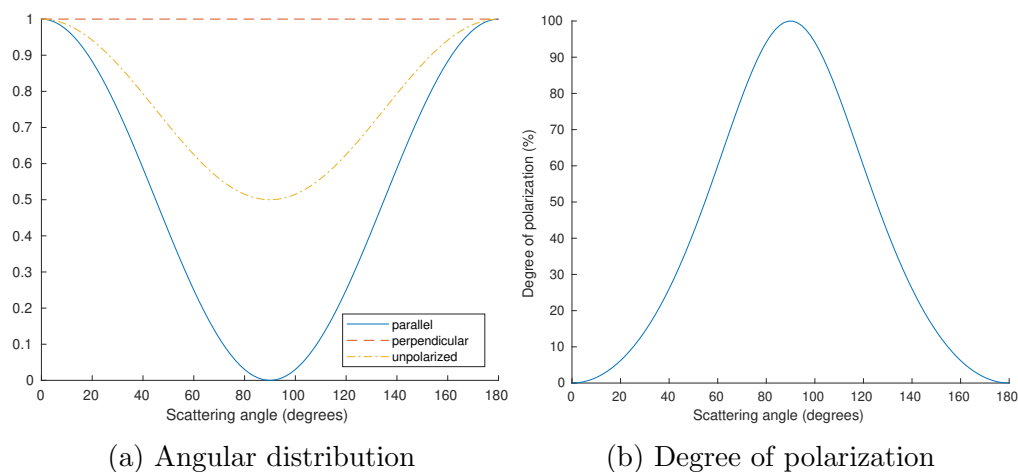
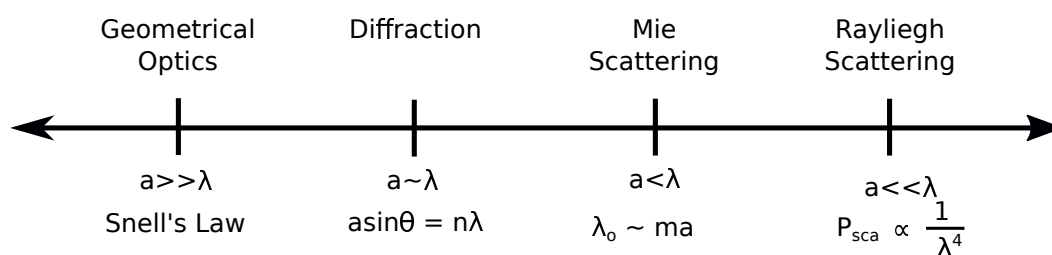


Figure 1.5: (a) Angular distribution of Rayleigh scattered light for different polarization; (b) Degree of polarization of scattered light for unpolarized incident light.

It should be noted that, if the incident light is perpendicularly polarized the scattered light retains the polarization, but for an unpolarized incident light, scattered light becomes partially polarized. This happens because, the polarization perpendicular to scattering plane survives as it is, but the parallel component diminishes with increase in scattering angle θ , as shown in figure 1.5.

Why is the sky blue and the clouds white?

The way light interacts with matter largely depends upon the size of the particle relative to the wavelength as illustrated in the figure below.



Particles which are very small compared to wavelength of the illuminating radiation exhibit Rayleigh scattering in which scattered power is inversely proportional to the fourth power of wavelength ($P_{sca} \propto 1/\lambda^4$). For instance, the red wavelength is 1.5 times the blue wavelength, as a result, the blue color scatters 5 ($= (1.5)^4$) times more strongly than the red color. Azure hue of the sky is attributed to Rayleigh scattering of the visible light primarily by atmospheric gas molecules and to some extent, by sub-micron dust particles. As the particle size increases and becomes comparable to or little less, *i.e.* 3-5 times smaller than wavelength, Mie scattering dominates. In this case the

waves whose wavelength is approximately equal to the particle size times its refractive index ($\lambda_0 = ma$), are scattered the most. White color of the clouds is due to Mie scattering. Water vapour gets precipitated on the dust particles forming scatterers of size beyond Rayleigh scattering regime. As a result all colors get scattered with similar probability and the clouds look white. Rainy clouds are dark because they are substantially thick and absorb huge amount of light. As the particle size increases further and becomes comparable to or even a few times (2-3 times) larger than the wavelength of light, phenomenon of diffraction becomes noticable. For particles which are very large compared to wavelength of light in free space, geometrical optics takes over and incident radiation is reflected according to the Snell's law.

1.5 Reciprocal lattice and Brillouin zone

Every crystal lattice has a reciprocal lattice attached to it whose primitive vectors are reciprocals of the real lattice's primitive vectors. Unit cell of a reciprocal lattice is called a Brillouin zone. If the basis of real lattice is made up of position vectors, the reciprocal lattice is constituted of wave vectors. Reciprocal lattice is basically the diffraction pattern or Fourier transform of real lattice.

A unit cell of a lattice and Brillouin zone of the reciprocal lattice are shown in figure 1.6. From the basic knowledge of vector algebra we know that area of

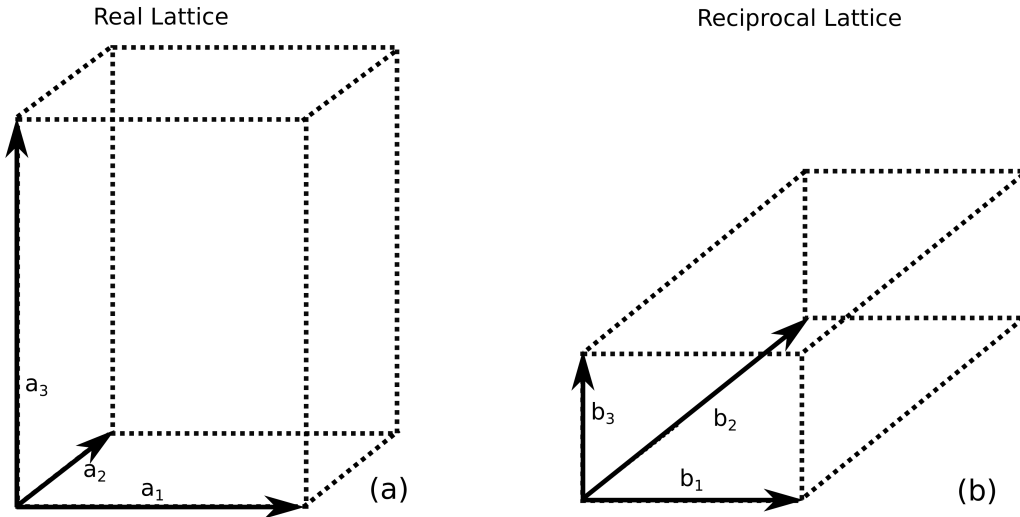


Figure 1.6: Unit cells of (a) real lattice and (b) reciprocal lattice.

the face including a_1 and a_2 is given by $\mathbf{A} = \mathbf{a}_1 \times \mathbf{a}_2$ and volume of the unit cell is given by $V = (\mathbf{a}_1 \times \mathbf{a}_2) \cdot \mathbf{a}_3$. It is understandable that vector \mathbf{a}_3 in terms of V and \mathbf{A} is written as $\mathbf{a}_3 = V/\mathbf{A}$, hence, the reciprocal vector $\mathbf{b}_3 = \mathbf{A}/V = (\mathbf{a}_1 \times \mathbf{a}_2)/(\mathbf{a}_1 \times \mathbf{a}_2) \cdot \mathbf{a}_3$. In this way, all the three primitive reciprocal vectors can

be defined as

$$\begin{aligned} \mathbf{b}_1 &= 2\pi \frac{\mathbf{a}_2 \times \mathbf{a}_3}{\mathbf{a}_1 \cdot \mathbf{a}_2 \times \mathbf{a}_3} \\ \mathbf{b}_2 &= 2\pi \frac{\mathbf{a}_3 \times \mathbf{a}_1}{\mathbf{a}_1 \cdot \mathbf{a}_2 \times \mathbf{a}_3} \\ \mathbf{b}_3 &= 2\pi \frac{\mathbf{a}_1 \times \mathbf{a}_2}{\mathbf{a}_1 \cdot \mathbf{a}_2 \times \mathbf{a}_3} \end{aligned} \quad (1.65)$$

It should be noted that the factor of 2π is included for the sake of convenience so

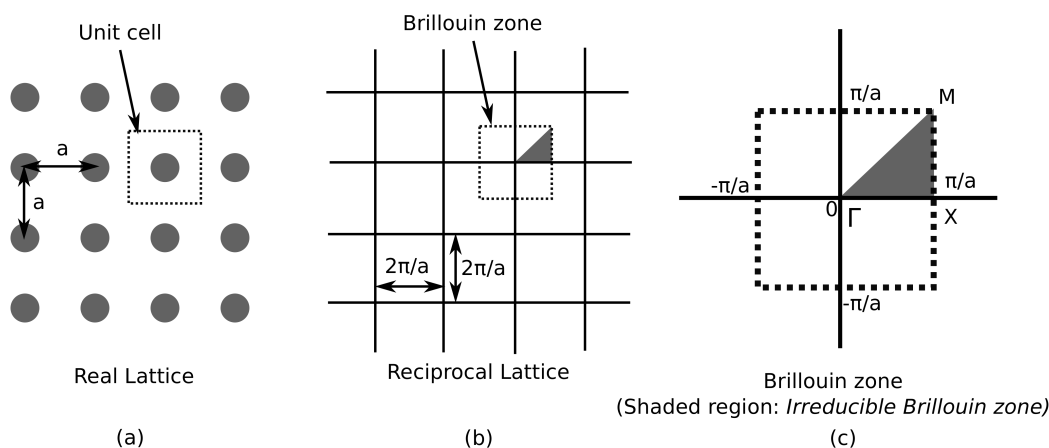


Figure 1.7: Unit cells of (a) real lattice and (b) reciprocal lattice.

that the reciprocal vector can be translated into the wave vector.

A crystal lattice is a periodic arrangement of atoms, which in turn means, a periodic variation of potential. On the similar lines, in a photonic crystal, the refractive index varies periodically. The most common type of photonic crystal is a square array of dielectric rods in air (as shown in figure 1.7(a)). It can be noticed from figure 1.7(b) that reciprocal of a square lattice is also a square lattice with a square Brillouin zone (figure 1.7(b)&(c)). In the Brillouin zone both the components of wave vector (k_x and k_y) vary from $-\pi/a$ to π/a . A closer inspection tells that the Brillouin zone is not the most fundamental unitcell and there is a smaller and more fundamental unit of the of the reciprocal lattice, shown as the wedge shaped shaded area in the figure 1.7(c). The shaded area is referred to as *Irreducible Brillouin zone* and the rest of the region can be obtained by applying mirror and rotation symmetry on it. For the intellectual satisfaction of a more ardent reader, Kittel (2005) presents a more exhaustive explanation of the reciprocal lattice and Brillouin zone for a variety of two and three dimensional crystal structures.

These are the basic concepts on which the peculiar properties of different types of metamaterials, are based. For example, frequency dependence of refractive index leads to the resonant nature of certain metamaterials; the plasmonic properties

APPLICATION SPECIFIC METAMATERIAL STRUCTURES, DEVICES AND COMPONENTS

of metals play pivotal role in achieving negative refractive index; Mie resonance becomes the underlying principle of the all-dielectric metamaterials including both – the positive index and the zero index variants; the zero index nature is attributed to certain specialties in the band structure arising due to symmetry in the Brillouin zone, and so on. In this way, this chapter presents the prerequisite information needed to understand the working of various types of metamaterials, which have been discussed in the next chapter, in detail.

Chapter 2

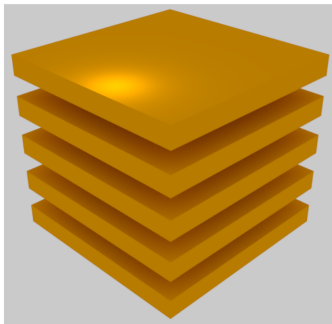
Introduction to metamaterials

Metamaterials are an extraordinary class of artificial materials which possess certain unnatural properties that seem to challenge common sense. These special properties are by the virtue of their structure. The unit cell of the structure is generally very small compared to the wavelength of light so that effective medium theory is applicable and the effective material parameters are considered. This chapter presents a variety of metamaterials, their classifications, working principle, merits & demerits and their potential applications.

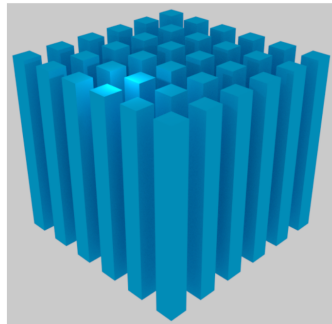
2.1 Classification of metamaterials

2.1.1 Classification on the basis of dimensions of inhomogeneity

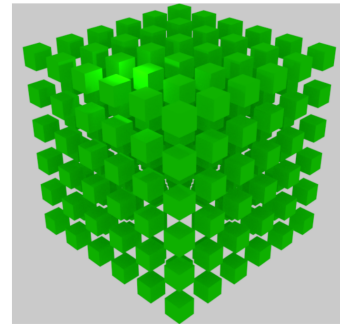
Depending upon the number of dimensions in which the structure is inhomogeneous, the metamaterials can be divided into three categories - one dimensional, two dimensional and three dimensional. Figure 2.1 gives a good visualization of the three categories.



(a) One dimensional



(b) Two dimensional



(c) Three dimensional

Figure 2.1: Classification on the basis of dimensions of inhomogeneity

There is another, a fourth variant, called a *metasurface*. Metasurfaces are two dimensional, planar, sheet type metamaterials whose thickness is very small compared to other two dimensions. There are two types of metasurfaces – metafilms and metascreens. Metafilms are two dimensional periodic arrangement of isolated scatterers, like the one shown in figure 2.2(a). Metascreens, on the other hand, are periodic arrangement of isolated apertures drilled in an otherwise continuous and impenetrable sheet of material, as in figure 2.2(b). A few intermediate structures, such as a parallel wire grating, exhibit both the traits. It behaves like a metafilm for polarization perpendicular to wires and acts as a metascreen for parallel polarization.

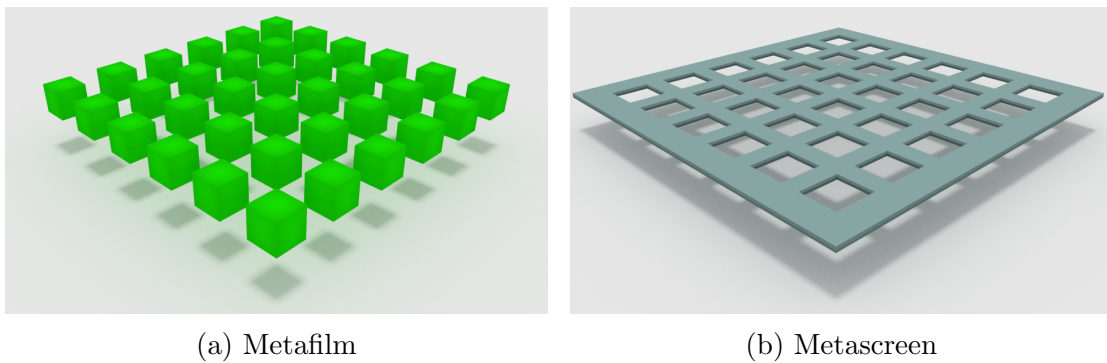


Figure 2.2: Two types of metasurfaces

2.1.2 Classification on the basis of constituent materials

In early stages of development, metamaterials had been metal-dielectric composites. Both the components had a crucial role to play in their functionality. Such designs achieved several interesting phenomena including negative refraction and electromagnetic cloaking. However, a major drawback with them was their significant ohmic loss, which dropped their performance drastically. Serious endeavors

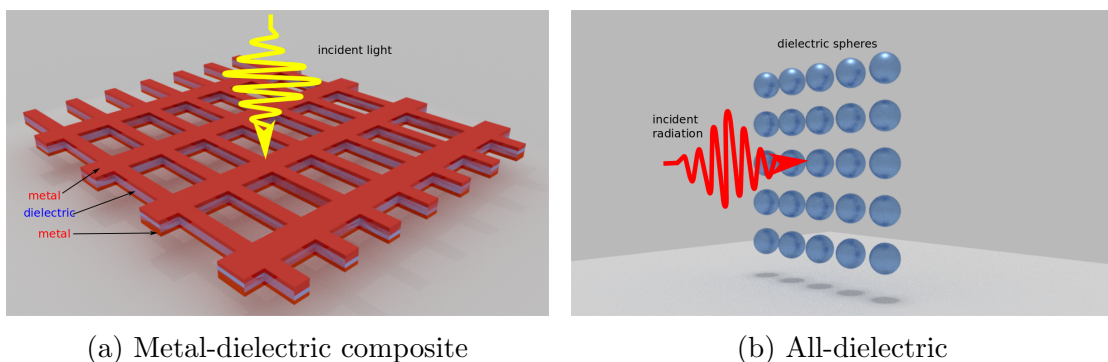


Figure 2.3: Two categories on the basis of constituent materials

seeking low loss alternatives led to the advent of all-dielectric or Mie resonance based metamaterial. Figure 2.3(a) illustrates fishnet type metamaterial which is a very common design to achieve negative refraction at higher frequencies. The other one shown in figure 2.3(b) is the famous Mie resonance based metamaterial structure which is basically a two dimensional periodic arrangement of high permittivity dielectric spheres (mostly silicon). A dielectric sphere is the simplest particle for which solutions of wave equation have already been deduced in terms of Riccati Bessel functions, by Gustav Mie in 1908 [9]. For any other shape numerical methods like finite difference time domain method [94, 74], finite element method [74, 41], etc are needed. All dielectric metamaterials have found applications like perfect reflection, directive radiation, wave shaping etc.

2.1.3 Classification on the basis of resonance

Resonance means the situation when the response of the scatterer is the strongest at one particular frequency of incident wave, and at any other frequency whether higher or lower than the resonant one, the response decreases sharply. Resonance happens when the incident or exciting frequency matches with the natural frequency of vibration of the system. The metamaterial structures which exhibit this property are referred to as resonant metamaterials. Figure 2.4(a) shows a split ring resonator (SRR) which is a resonant structure and a well known magnetic meta-atom, while in figure 2.4(b) a wiremesh structure is shown which is a non resonant metamaterial [35, 5, 88, 70, 13, 86, 84]. Resonant behavior of a split

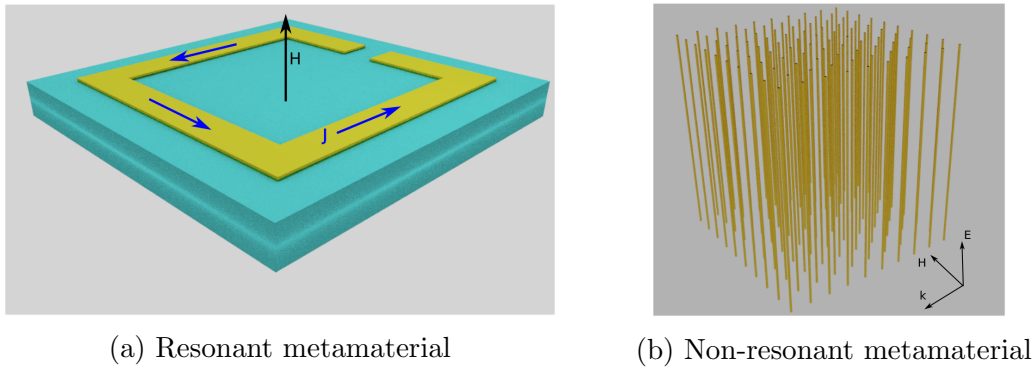


Figure 2.4: Categorization on the basis of resonance

ring resonator is attributed to its LCR circuit like nature. The split in the ring provides that capacitive element while the metal of the ring has some latent inductance and resistive loss associated with it. In this way, it behaves like an LCR circuit having a certain resonant frequency. On the other hand, the wire mesh structure is made up of continuous metal wires which do not have any breaks in them. Hence in the absence of capacitive element they fail to exhibit resonant behavior. Exhaustive details about working of split ring resonator and wire mesh

structures are presented in the later sections of this chapter.

2.1.4 Classification on the basis of refractive index

By definition, the metamaterials are basically the structures whose optical properties or particularly the refractive index can be tailored as desired. On the basis of effective refractive index the metamaterials can be of three types – *positive index*, *negative index* & *zero index metamaterials*. Figure 2.5 shows the refraction of light as it emerges out of the prisms of a positive, a negative and a zero index medium into air. The figure illustrates that while in case of positive index medium the emergent ray is on the other side of the normal, as usual; for negative index prism it lies on the same side of the normal as the incident ray. Although it seems abnormal, it is absolutely in accordance with the Snell's law of refraction.

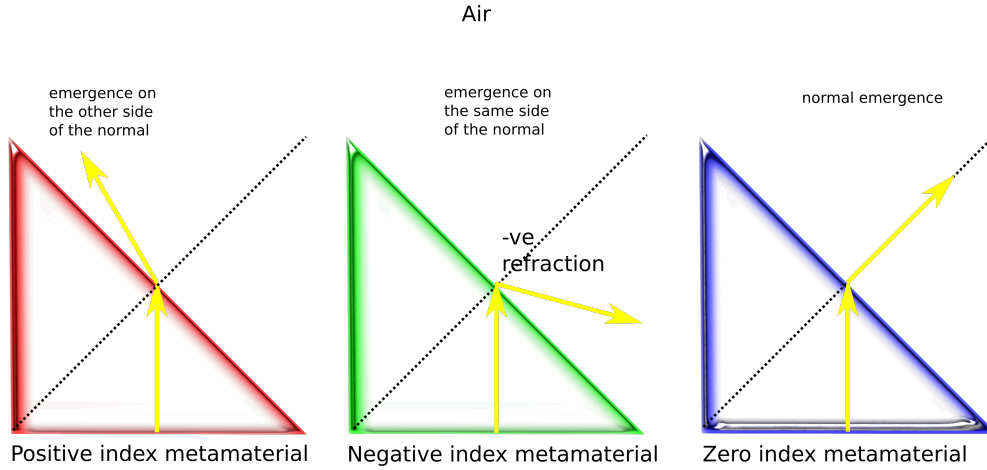


Figure 2.5: Refraction of light by positive, negative and zero index metamaterial

According to the Snell's law,

$$n_1 \sin \theta_1 = n_2 \sin \theta_2 \quad (2.1)$$

where n_1 is the refractive index of prism and n_2 is the refractive index of surrounding (air, in this case), and the angle θ is measured w.r.t the normal and considered positive in clockwise sense. If $n_1 < 0$, $n_2 = 1 (> 0)$ and $\theta_1 > 0$, it is certain that $\theta_2 < 0$. In consequence, emergent ray lies on same side of the normal as incident ray. From the same equation 2.1, it can be deduced that if $n_1 = 0$, for any value of angle of incidence (θ_1), the angle of emergence is inevitably zero. In other words, light always emerges normally (i.e. along the normal) irrespective of the angle of incidence, if it travels from a zero index medium to a positive index medium.

2.2 A few important and commonly used metamaterials

A meta-atom is the structural unit of a metamaterial whose periodic repetition generates the metamaterial structure. Metamaterials can be responsive to either electric or magnetic field depending upon the type of meta-atoms they are made of. A few most significant and commonly used metamaterials have been described in detail, in the following subsections.

2.2.1 Metal dielectric layers

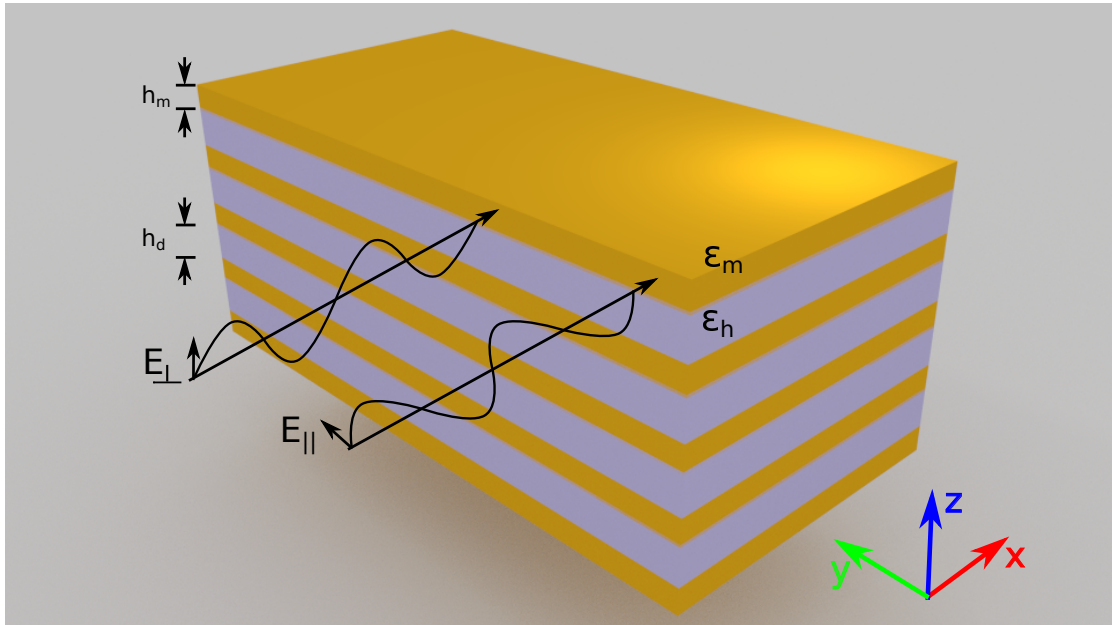


Figure 2.6: Schematic illustration of metal-dielectric layers based electric metamaterials for parallel and perpendicular polarization.

The simplest electric metamaterial (i.e. *responsive to electric field*) is the alternating layers of a metal and a dielectric material, which is the easiest way to achieve the desired permittivity at the wavelength of interest. Metals intrinsically exhibit negative dielectric constant below their plasma frequency due to the presence of free electron in them. This property proves beneficial in realization of negative refractive index where negative permittivity ($\epsilon < 0$) and negative permeability ($\mu < 0$) are required simultaneously. Interleaving dielectric layers in between metals, dilutes the metal in a way and allows the liberty to reduce the permittivity to the desired magnitude. The value of effective permittivity thus obtained depends upon the filling fraction of the metal and the dielectric in a unit cell, as well as, on the polarization of the incident field. For the structure shown

in the figure 2.6, let us suppose that ϵ_m is the permittivity of metal and ϵ_d is the permittivity of the dielectric, and h_m & h_d are their respective thicknesses, and in consequence, $f_m = h_m/(h_m + h_d)$ and $f_d = h_d/(h_m + h_d) = 1 - f_m$ become the filling fractions of metal and dielectric respectively. The incident electric field can either be polarized parallel or perpendicular to the interface. In case of perpendicular polarization, the electric field is discontinuous across the boundary, but the displacement vector is continuous, i.e. $D_m = D_d = D_\perp$. On account of discontinuity, the effective electric field, as a weighted mean, is given as

$$E_\perp = f_m E_m + f_d E_d \quad (2.2)$$

Hence, the effective permittivity ϵ_\perp is given by

$$\frac{1}{\epsilon_\perp} = \frac{E_\perp}{D_\perp} \quad (2.3)$$

$$= \frac{f_m E_m}{D_\perp} + \frac{f_d E_d}{D_\perp} \quad (2.4)$$

$$= \frac{f_m}{\epsilon_m} + \frac{f_d}{\epsilon_d} \quad (2.5)$$

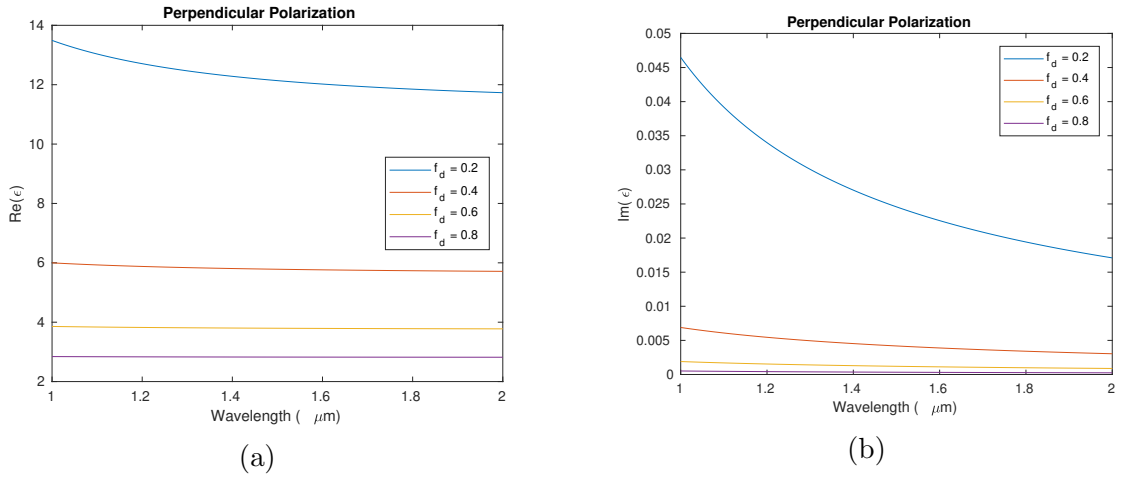


Figure 2.7: Dependence of (a) real and (b) imaginary part of effective permittivity on dielectric filling fraction for perpendicular polarization

On the contrary, for parallel polarization, the electric field is continuous across the interface, i.e. $E_m = E_d = E_\parallel$, while the effective displacement vector is represented in average as

$$D_\parallel = f_m D_m + f_d D_d \quad (2.6)$$

Therefore, the effective permittivity is

$$\epsilon_{||} = \frac{D_{||}}{E_{||}} \quad (2.7)$$

$$= \frac{f_m D_m}{E_{||}} + \frac{f_d D_d}{E_{||}} \quad (2.8)$$

$$= f_m \epsilon_m + f_d \epsilon_d \quad (2.9)$$

The effective permittivity as a function of wavelength, for the perpendicular and

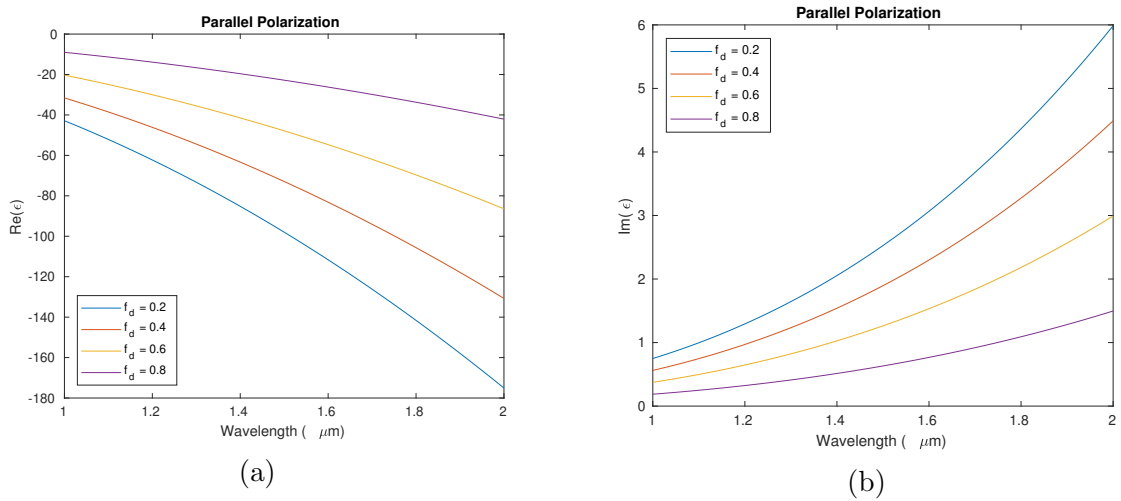


Figure 2.8: Dependence of (a) real and (b) imaginary part of effective permittivity on dielectric filling fraction for parallel polarization

parallel polarization, have been shown in figures 2.7 & 2.8.

2.2.2 A periodic array of metallic wires

A wire mesh structure is a very good and useful artificial medium whose plasma like behavior can be configured for any spectrum of choice, by simply manipulating the geometrical parameters. Rotman [73], in 1961, propounded for the very first time, what he called the *rodded medium*, a periodic array of long metals wires capable of simulating plasma. Since then such media have been used by radio engineers as a simple method to imitate the ionospheric conditions in a laboratory environment. Pendry et al. [67, 66], in 1996, proposed it afresh in his seminal paper which later turned out to be of great significance in the development of negative refractive index metamaterials. They also presented a Drude's model based representation of the effective permittivity of the metamaterial.

Let us consider a square lattice of thin and long metallic wires, shown in figure 2.9, of radius r and periodicity a being illuminated by a z-polarized wave. If

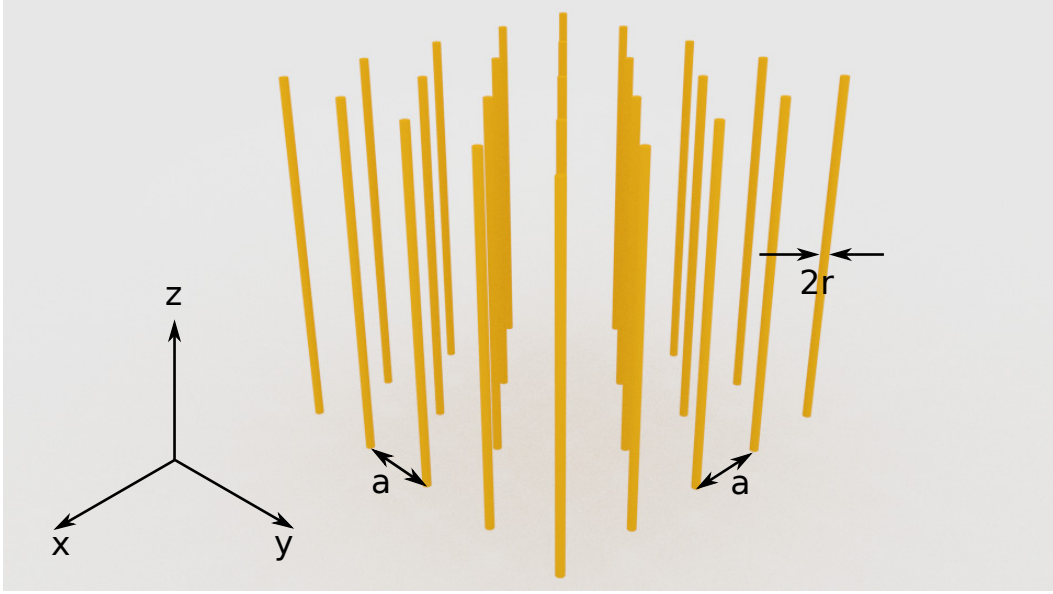


Figure 2.9: An array of metal wires

N is the number density of electrons in the pure metal, then, the effective number density of electrons in the metamaterial is

$$N_{eff} = \frac{N\pi r^2}{a^2} \quad (2.10)$$

and it can be shown that [13, 70]

$$m_{eff} = \frac{\mu_0 r^2 e^2 N}{2} \ln(a/r) \quad (2.11)$$

Hence, the plasma frequency of the metamaterial becomes,

$$\omega_p^2 = \frac{N_{eff} e^2}{\epsilon_0 m_{eff}} = \frac{2\pi c_0^2}{a^2 \ln(a/r)} \quad (2.12)$$

where c_0 is the speed of light in vacuum. Using the plasma frequency ω_p , the conductivity σ of the metal, the radius r and the periodicity a , the Drude's model based effective permittivity ϵ_{eff} can be calculated as,

$$\epsilon_{eff} = 1 - \frac{\omega_p^2}{\omega(\omega + i\epsilon_0 a^2 \omega_p^2 / \pi r^2 \sigma)} \quad (2.13)$$

For a typical metamaterial structure made of up silver wires of radius $r = 0.1$ mm, periodicity $a = 5$ mm and conductivity $\sigma = 6.30 \times 10^7$ (S/m), the Drude model based effective permittivity the metamaterial has been shown in figure 2.10(c) as a function of angular frequency ω , whereas, figure 2.10(b) shows the permittivity

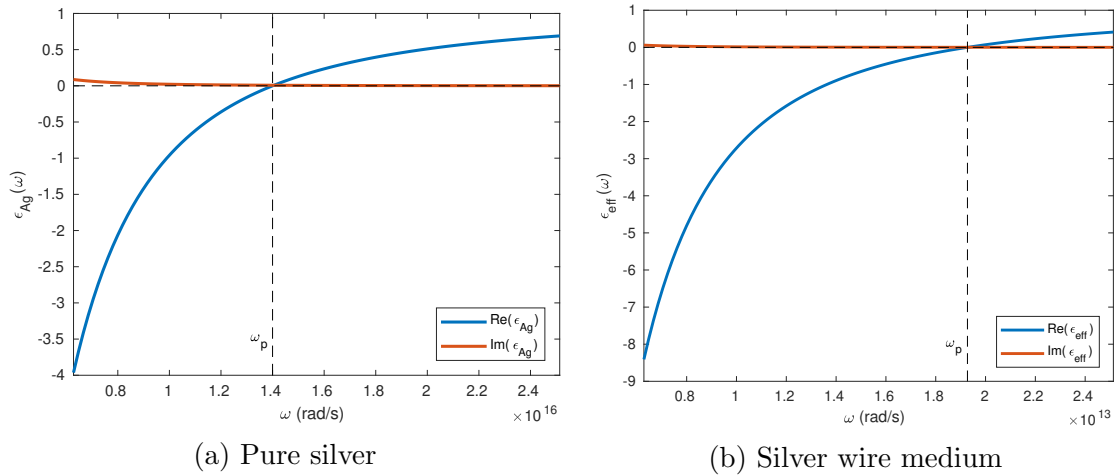


Figure 2.10: Real and imaginary part of permittivity (a) pure silver and (b) wire mesh type metamaterial made up of silver wires

variation of pure silver metal. This is a clear evidence of the fact that wire mesh structures are efficient means to simulate the plasmonic properties in the spectrum of choice. It can be noticed in both the graphs that the permittivity remains negative before plasma frequency and becomes positive above it. It manifests into the behaviour that, the materials remain plasmonic hence reflecting below plasma frequency, but as soon plasma frequency is passed, plasmonic character is redeemed and dielectric like transmitting nature is begun to acquire. However a major contrast visible in the two figures is that the plasma frequency of the metamaterial lies in terahertz spectrum, while that for pure silver lies in petahertz range.

2.2.3 Split ring resonator - a magnetic meta-atom

Naturally occurring materials cease their magnetic activity at high frequencies, hence become unresponsive towards magnetic field component of the incident electromagnetic waves settling the value of relative permeability μ_r to 1. In year 2000, Smith et al. invented a meta-atom which could interact with magnetic field of the incoming radiation and exhibited a magnetic dipole like behavior whose strength was maximum at a certain resonant frequency. They called it a *split ring resonator* (SRR) as the structure was basically a metallic ring with a split on one side. Its working principle is simply the Lenz's law.

Let us consider a metallic disc which is exposed to oscillating magnetic field along the axis. The varying magnetic field induces current in the disc such that the induced flux opposes the applied flux. It is an acknowledged fact that current is mainly confined to the outer boundaries of the disc, the inner region of the disc can be removed turning it into a ring without destroying the inductive characteristics. The disc and the ring are purely inductive elements in which capacitive effects

are absent, hence, they are non-resonant. For resonance to occur, a capacitive element is required to be added, in order to achieve an LCR circuit like system which resonates at a certain frequency. This is accomplished by purposely introducing a split in the ring which harbors charge accumulation and hence provides capacitive element in the system. This type of design has inductance as well as capacitance and considering the resistivity losses of metal, it can be represented by a series LCR circuit whose resonance frequency is given by $\omega_0 = 1/\sqrt{LC}$ where symbols have their usual meaning. In figure 2.11, the complete transformation from a disc to double split ring resonator is shown. It can be seen in the figure that the direction of the induced current is such, that the induced field opposes the applied field. Furthermore, charge accumulates at two ends of the split, which causes existence of electric field in the gap region. It excites an electric dipole mode which can overshadow the desired magnetic dipole and in consequence, the electric field component of the incident wave interacts with the device more strongly compared to the magnetic field. In order to avoid this situation, a double split ring resonator (DSRR), as shown in figure 2.11, is always a preferred choice. A DSRR has two concentric rings with splits deliberately placed opposite to each other, so that the two electric dipoles are anti-parallel and net electric dipole moment is negligible.

Being resonant structures, both - the single and the double split ring resonators, can be electrically represented by equivalent LCR circuits (figure 2.12) whose effective inductance L , effective capacitance C and resistance R decides the systems resonance frequency ω_0 . In figure 2.12, r is the inner radius of smaller ring, w is the linewidth of each ring, d is the gap between the two rings and i denotes induced current. Inductance can be simply estimated as $L \approx 2\mu_0 r$ [13].

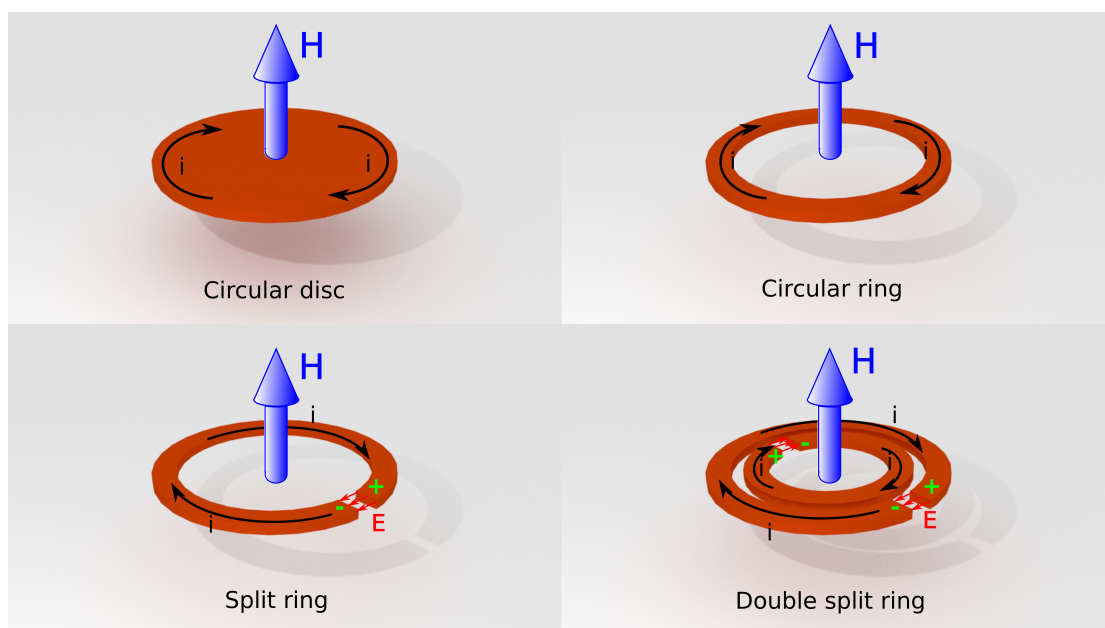


Figure 2.11: Evolution from a simple circular disc to double split ring resonator

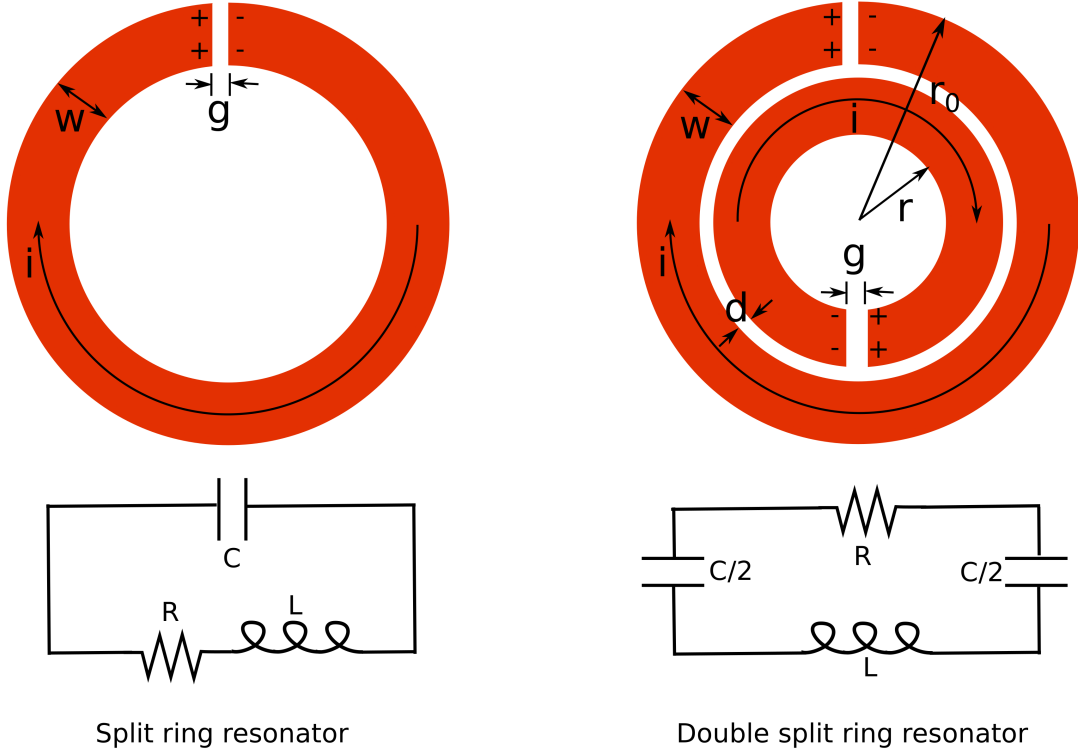


Figure 2.12: LCR equivalent circuit for single and double split ring resonator.

The total capacitance of a DSRR is contributed by two sources - capacitance due to the split g and capacitance due to slot d between the two rings. Out of which the latter is more dominant [6], since circumference of the rings is large compared to the split size g and slot width d is usually smaller. As current flows through the two rings it encounters the gap d in each cycle. More accurately, the resultant capacitance can be thought to be due to two capacitors in series combination, as shown in figure 2.12. Hence, if C is the capacitance between two annular electrodes, then, $C/2$ is the capacitance due to each half of the ring, and $C/4$ is the total capacitance of the DSRR [13, 6].

The purpose of this entire analysis is to calculate the dispersion in effective magnetic permeability of an SRR and to derive a mathematical equation for it. A rigorous analysis has been presented by Ramakrishna (2005) [70] for the artificial magnetic activity of the split cylinders and the split ring resonators. The author shows that for an SRR, effective capacitance $C = \epsilon_0 \epsilon_r \pi r / (3d)$ and its effective magnetic permeability in relation to a split cylinder is given as

$$\mu_{eff} = 1 - \frac{\pi r_0^2 / a^2}{1 - (3d / \mu_0 \epsilon_0 \epsilon_r \pi^2 \omega^2 r_0^3) + i(2\rho / \mu_0 \omega r_0)} \quad (2.14)$$

$$= 1 + \frac{f\omega^2}{\omega_0^2 - \omega^2 - i\Gamma\omega} \quad (2.15)$$

where, ϵ_r is the relative permeability of the material present in the gap, a is the periodicity of the array of SRR, $f = \pi r_0^2/a^2$ is the fill fraction and ω_0 being the resonant frequency is given by

$$\omega_0 = \left(\frac{3d}{\mu_0 \epsilon_0 \epsilon \pi^2 r_0^3} \right)^{1/2} \quad (2.16)$$

Figure 2.13 shows the μ_{eff} versus frequency graph of an SRR having $r_0 = 1$ mm, $a = 5$ mm, $d = 0.1$ mm and $\rho = 1.0 \Omega/\text{m}$. The resonant frequency for the SRR comes out to be 8.317 GHz, and it can be seen in the figure that at resonant frequency that the imaginary part of μ_{eff} becomes maximum while the real part toggles polarity. The real part remains negative beyond ω_0 until a certain value of frequency called magnetic plasma frequency, after which it returns to the positive values. The magnetic plasma frequency, as mentioned by Ramakrishna(2005) [70], is given as,

$$\omega_m = \left(\frac{3d}{(1-f)\mu_0 \epsilon_0 \epsilon \pi^2 r_0^3} \right)^{1/2} \quad (2.17)$$

which in this case is 8.87 GHz. A great advantage of the structure is that it is easily tunable to different frequency ranges by varying the geometrical parameters. The split-ring resonators led to the development of SRR-wire composite type negative index metamaterials which proved to be a great revolution in electrodynamics. Beside SRR a few other interesting magnetic meta-atoms have also been developed

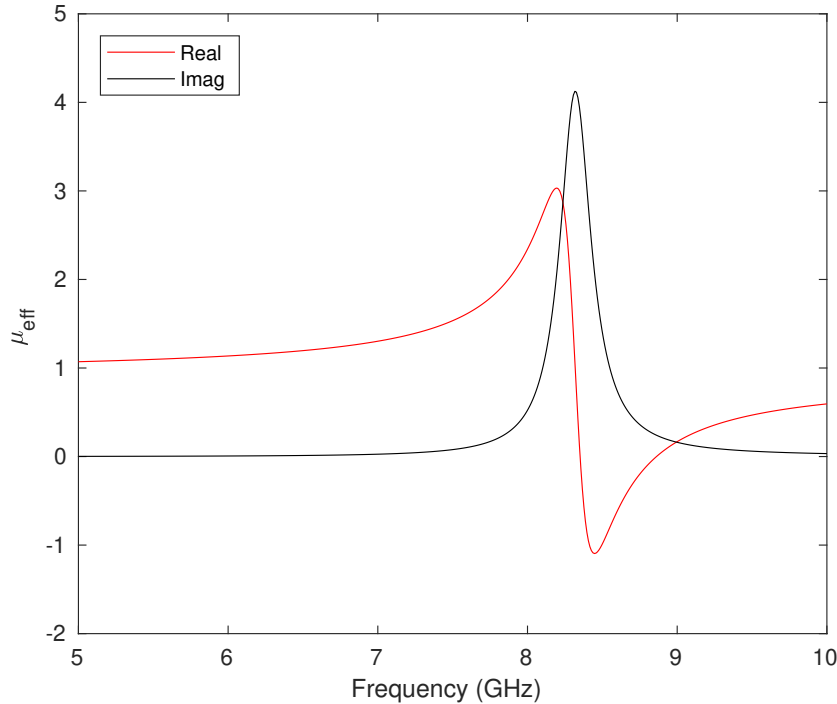


Figure 2.13: Effective magnetic permeability of an SRR

including the couple-rods [12], tunable V-shaped resonator [46], etc, but popularity gained by SRR remains unmatched.

2.3 A few interesting manifestations and applications of metamaterials

Out of numerous interesting application of metamaterials a few interesting ones have been listed here, which include, *negative Goos-Hanchen shift*, *perfect lensing*, *electromagnetic cloaking* and *wavefront engineering*.

2.3.1 Negative Goos-Hanchen shift

Precise investigation show that, in total internal reflection light does not get reflected back into the denser medium from the same point at which the incident ray hits the interface of the two media. The reflected ray is sifted from the incident wave by a minute distance, which is called Goos Hanchen shift [29], as shown in figure 2.14(a). The reason for this shift is the fact that light does not get reflected immediately from the interface, and is able to penetrate into the rarer medium to some extent which causes a slight delay. During this period it happens to travel a little distance along the interface before re-entering the denser medium. The Goos Hanchen shift is calculated as

$$d = \frac{-1}{k_1} \sin\theta \frac{d\phi_R}{dk_x} \quad (2.18)$$

where k_1 is the propagation constant in denser medium, θ is the angle of incidence and $d\phi_R$ is the phase shift in the reflection coefficient. In case of negative index medium (metamaterial), as shown in figure 2.14(b), the phase shift is negative, as a result Goos Hanchen shift is negative as well [8].

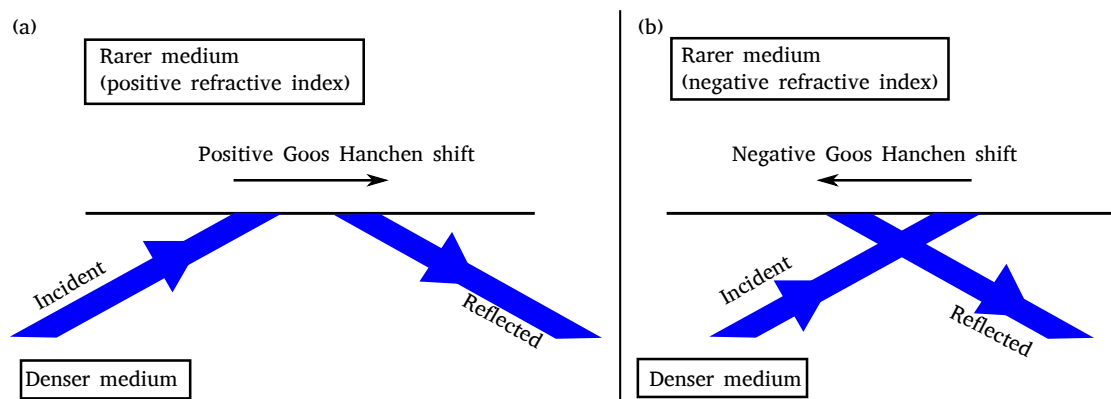


Figure 2.14: Goos Hanchen shift in case of, (a) positive index and (b) negative index metamaterials

2.3.2 Perfect lensing

Light emerging from an object has both – the propagating and the evanescent component. The propagating component is sinusoidal and can be collected by simple optical lenses based instruments, but the evanescent waves are lost because they decay exponentially to immeasurably small magnitudes within close proximity of the source, as illustrated in figure 2.15. Due to the Abbe's diffraction limit, the conventional lenses are unable to resolve objects smaller than the illuminating wavelength λ_0 , hence the subwavelength details of the object remain invisible. However, the negative index metamaterials are capable of collecting evanescent waves which contain subwavelength details of the object, hence defeating the Abbe's diffraction limit. The wave vector in the direction of propagation can be written in terms of Fourier components as

$$k_z = \sqrt{k_0^2 - k_x^2 - k_y^2} \quad (2.19)$$

where k_0 is free space wave vector and k_x, k_y are Fourier components of waves from object. For the propagating wave,

$$k_t = \sqrt{k_x^2 + k_y^2} < k_0 \quad (2.20)$$

Hence, k_z is real and the electric field varies sinusoidally as $e^{ik_z z}$. Where as, for the evanescent component,

$$k_t = \sqrt{k_x^2 + k_y^2} > k_0 \quad (2.21)$$

Hence, $k_z = i\sqrt{k_x^2 + k_y^2 - k_0^2} = i\kappa_z$ (imaginary), and the field is exponentially decaying $e^{-\kappa_z z}$ (see figure 2.15). But inside a negative index metamaterial, the

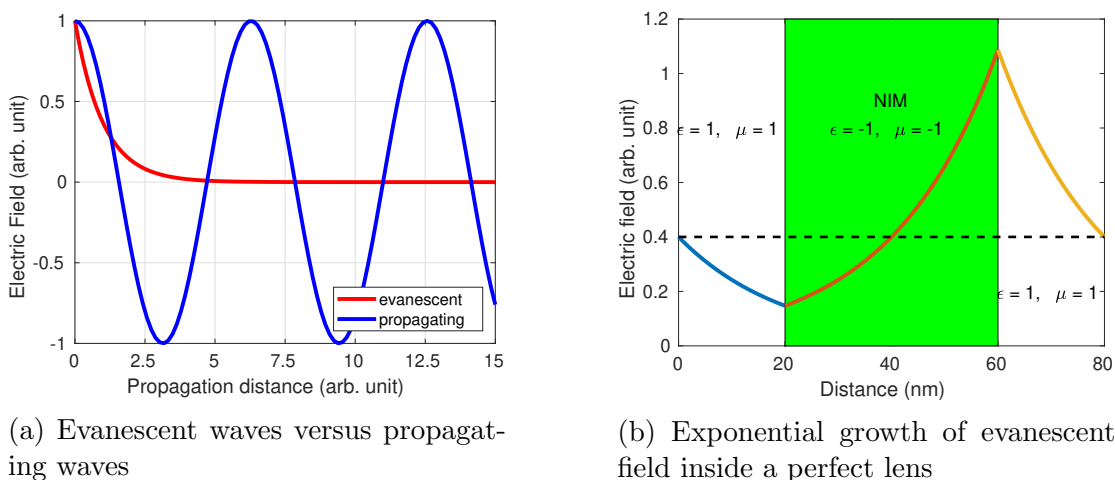


Figure 2.15: Perfect lensing by a negative index metamaterial

field varies as $e^{-(-1)\kappa_z z} = e^{\kappa_z z}$, hence, instead of fading it grows exponentially. In this way a negative index metamaterial is able to collect evanescent waves, which can reveal the subwavelength details of the object.

2.3.3 Electromagnetic cloaking using zero index metamaterials

Huang et al., in 2011 [37], showed that a square lattice of dielectric rods in air of a certain radius to periodicity ratio, acts a low loss zero index medium (ZIM). Being a zero index medium it does not change the phase of incident radiation, which means that, phase of the incident light hitting one end of the ZIM slab is exactly the same as that of the transmitted wave exiting the other side. The wave is apparently tunneled unperturbed through the ZIM slab. In this way, if an object is embedded inside the ZIM slab, it remains undetected as the incoming wave has technically no perception of the space inside the ZIM. This phenomenon challenges common sense, but it can be better understood by means of visualization shown in figure below. Figure 2.16(a) illustrates the zero index property of the Huang's

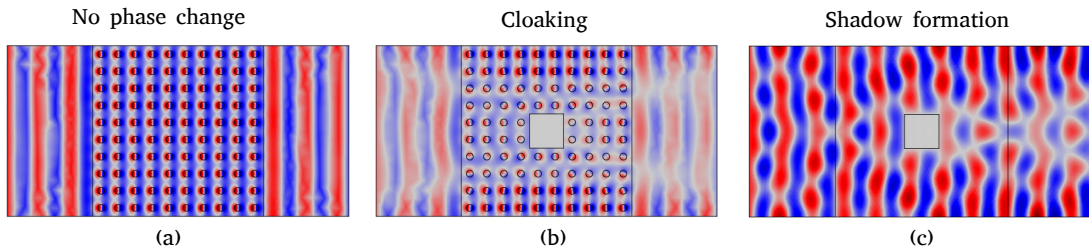


Figure 2.16: Electromagnetic cloaking using zero index metamaterials.

metamaterial. The phase of the wave at the entry is same as that at the exit boundary of the slab. In figure 2.16(b), there is an object embedded in the ZIM, but it does not distort the wavefronts, they pass undisturbed to other side and no shadow is formed. Whereas, in the absence of ZIM (figure 2.16(c)) the object breaks the incident wavefront and shadow region is created.

2.3.4 Wavefront engineering

The interesting applications of zero index metamaterials are as many as a creative mind can think. Another interesting and useful application of a ZIM is wavefront engineering. Similar to the electromagnetic cloaking, this application is also attributed to the *no change in phase* property of ZIM, as discussed above. In zero index medium all the points inside the bulk, as well as, on the boundaries are vibrating in the same phase, hence shape of the boundary is replicated into the shape of the wave front as it is. Figure 2.17 shows that the shape of the exit boundary decides the shape of the wavefront of the exiting wave. Convex

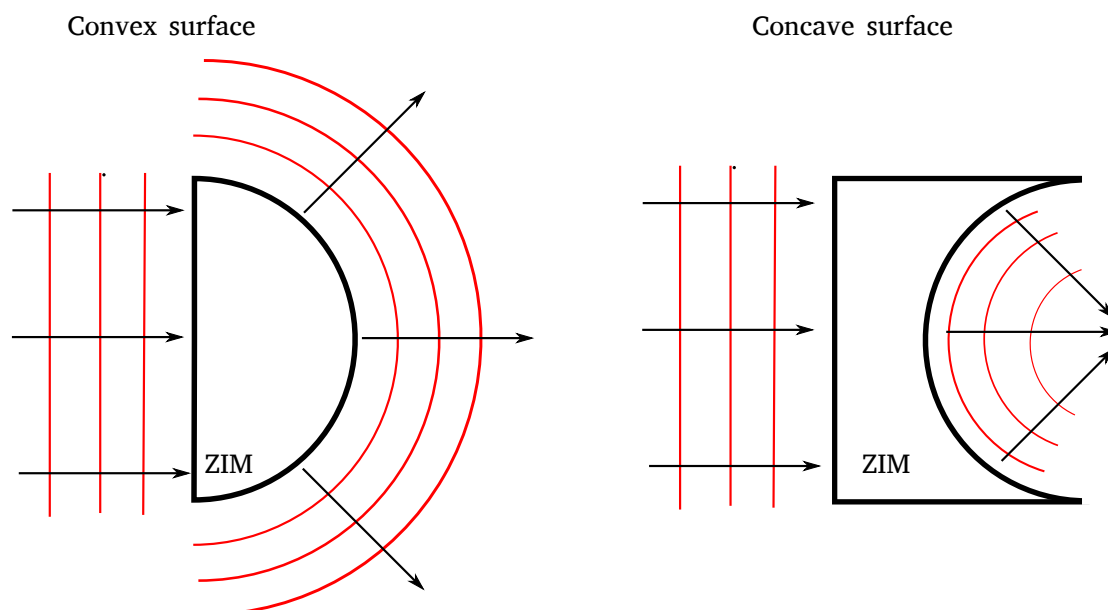


Figure 2.17: Electromagnetic cloaking using zero index metamaterials.

boundary produces diverging wave while concave boundary produces converging wave.

The metamaterial structures and the applications discussed in this chapter are very basic and well-known. The later chapters of the thesis present a rigorous account of a few novel designs of application specific metamaterials. In the next, the chapter 3, a unique design of a high-quality laser cavity based on all-dielectric metasurfaces has been proposed, which is an extremely compact design with high-quality factor. The chapter 4 presents a split-nanotube-based negative index metamaterial (NIM), for which the value of the negative refractive index achieved is as low -2 and the figure of merit (FOM) is as high as 8 in mid infrared spectrum. The proposed design is an elongated version of split ring resonator (SRR), excluding its limitations. A potential application of the proposed negative index metamaterial can be perfect lensing, as discussed above. Chapter 5 is dedicated to a novel design of metamaterial perfect absorber (MPA), which comprises a periodic array of LiTaO_3 microcylinders grown over a silver substrate, shows high absorption coefficient in the said wavelength range with a maximum of 99.9% in terahertz spectrum and is useful in terahertz applications such as thermal imaging. The chapters 6 and 7 deal with a particularly new and intriguing class of metamaterials called *zero index metamaterials* (ZIMs). The chapter 6 presents an interesting application of ZIM, where, a highly directive all-dielectric zero-index metamaterial (ZIM) based nanoantenna has been reported which has the ability to directionally transmit the radiation from an isotropic quantum emitter. It makes use of Huang's rods-in-air type zero index metamaterial. In chapter 7, a novel design of zero index metamaterial has been proposed which can operate

for both – the transverse magnetic TM and the transverse electric TE polarization. The author has tried his best to present a rigorous theoretical explanation and numerical analysis for a potential reader's appetite. In the end, the chapter 8 presents a summary of the entire research work and talks about the future scope in the area of metamaterials.

Chapter 3

All-dielectric metasurface perfect reflectors as cavity resonator

3.1 Introduction

As explained in the previous chapter, metasurfaces are two dimensional sheet type metamaterials having thickness several times smaller compared to the wavelength of operation. Their subwavelength structure spreads in two dimensions in either periodic or aperiodic arrangement. Metasurfaces can be used to provide such peculiar optical properties to a device which cannot be achieved by thin films of naturally occurring materials [105, 45, 36]. Recently, all-dielectric metamaterials and meta-surfaces have been proposed as a more effective counterpart for plasmonic ones [49, 38, 4]. The principle which lies at the heart of the all-dielectric metamaterials and metasurfaces is the optical response of high-index dielectric nanoparticles. The high-index dielectric nanoparticles possess electric and magnetic resonances in the visible range, providing efficient control of light scattering [68, 108, 26, 25, 59, 3, 54] and strong field enhancement [7, 14, 22, 78]. An advantage of choosing dielectric structures is the very low dissipation losses due to their negligibly small extinction coefficient. Today, such all-dielectric metasurfaces have been implemented for wavefront engineering [20, 18], electromagnetically induced transparency [103], high transmission [106], beam collimators [2], and especially for broadband perfect reflectors [85, 61, 10]. The last one opens new & unique opportunities for designing of optical lenses, reflectors and especially cavities for semiconductor lasers. Semiconductor lasers have revolutionized optical communication system. It has been demonstrated that they are excellent power sources for optical fibers, because of which long distance and high speed communication is now possible. Despite the tremendous development in design of lasers in terms of geometry, wavelength of operation, pulse duration, threshold current, etc., attempts are continuously being made to improve their performance [81]. In particular, further miniaturization of the semiconductor lasers is an important issue to create sub-micron thick highly efficient coherent light sources.

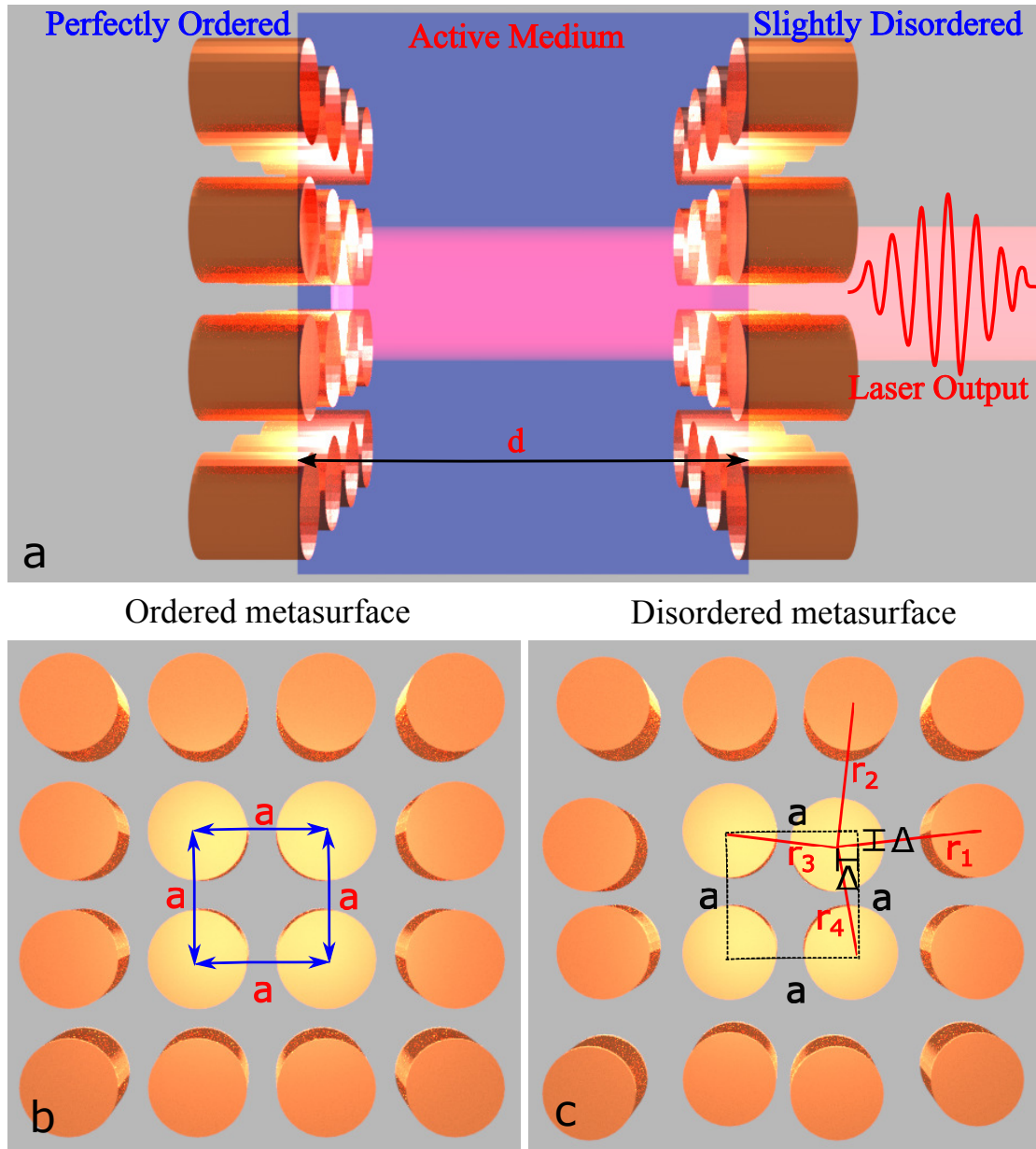


Figure 3.1: (a) Schematic illustration of laser cavity based on all-dielectric metasurfaces. (b) Design of the first reflector. (c) Design of the second reflector based on a disordered metasurface.

In this chapter, a compact design of cavity resonator based on all-dielectric metasurfaces has been reported. In the reported design (see figure 3.1), mirrors are made up of a two dimensional periodic arrangement of silicon (Si) cylindrical particles having wisely chosen diameter, height and periodicity to operate at a particular wavelength. The cylindrical shape of particles was chosen because its performance in perfect reflection is well studied and it is easy to fabricate by

means of electron beam lithography. In Refs. [18, 61, 60, 32, 83] it has been experimentally demonstrated that a perfectly ordered array of the silicon cylinders can reflect nearly 100% of the normally incident radiation. In Ref. [61] it has also been shown that reflectivity is reduced if there is a slight disorder in the periodic arrangement of cylinders. In the reported design, the perfectly ordered dielectric array exhibits property of perfect reflection (reflectance $\approx 100\%$) and hence can be used as the first mirror of a cavity. Any type of disorder slightly reduces the reflectance, hence such an array (reflectance $\approx 99.5\%$) can be used as the second mirror of a cavity i.e. the output coupler. Furthermore, a comparative study between the metasurface reflector type cavity and a Bragg reflector type cavity has been presented, in which the former clearly outshines the 25 pairs thick Bragg mirror due to more compact design, 5 times higher quality factor and 80% lesser threshold gain coefficient.

3.2 Fundamental principle of perfect reflection

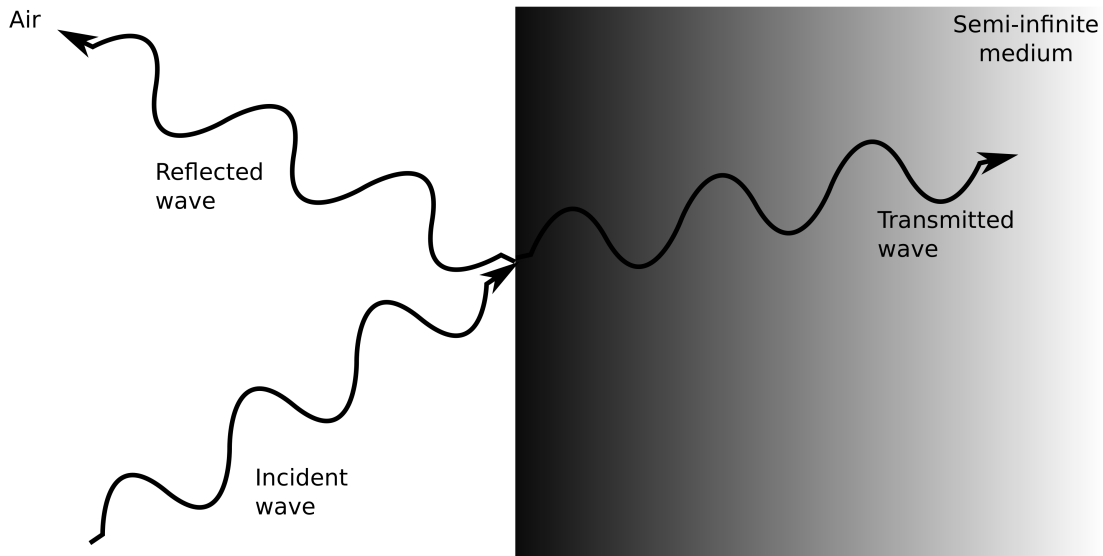


Figure 3.2: Reflection and transmission taking place at the interface of air and a semi-infinite medium due to the impedance mismatch between the two media.

As a wave travels from one medium to another, it undergoes transmission and reflection in parts, depending upon the impedance mismatch between the two media. While small mismatch results in high transmission, high mismatch leads to high reflection. Hence extreme contrast in the impedances of the two media leads to perfect reflection. To derive the conditions of perfect reflection let us assume semi-infinite medium of complex impedance $z = z' + iz''$, into which light enters from air. At the interface between the two media, reflection takes place

whose amplitude reflection coefficient and reflectance are given by,

$$r = \frac{z - 1}{z + 1} \quad (3.1)$$

and

$$R = |r|^2 = \frac{(z' - 1)^2 + z''^2}{(z' + 1)^2 + z''^2} \quad (3.2)$$

where $z = \sqrt{\mu/\epsilon}$, in which, $\mu = \mu' + i\mu''$ and $\epsilon = \epsilon' + i\epsilon''$ are complex relative permeability and permittivity respectively. Perfect reflection means $R = 1$, i.e.

$$\begin{aligned} \frac{(z' - 1)^2 + z''^2}{(z' + 1)^2 + z''^2} &= 1 \\ (z' - 1)^2 + z''^2 &= (z' + 1)^2 + z''^2 \\ (z' + 1)^2 - (z' - 1)^2 &= 0 \\ z' &= 0 \end{aligned} \quad (3.3)$$

without any particular condition on z'' . Considering $z = \sqrt{(\mu' + i\mu'')/(\epsilon' + i\epsilon'')}$, we get

$$\begin{aligned} z^2 &= \frac{\mu' + i\mu''}{\epsilon' + i\epsilon''} \\ z'^2 - z''^2 + 2iz'z'' &= \frac{(\mu' + i\mu'')(\epsilon' - i\epsilon'')}{\epsilon'^2 + \epsilon''^2} \\ &= \frac{(\mu'\epsilon' + \mu''\epsilon'') + i(\mu''\epsilon' - \mu'\epsilon'')}{\epsilon'^2 + \epsilon''^2} \end{aligned}$$

Considering $z' = 0$ according equation 3.3, we obtain that,

$$\mu''\epsilon' - \mu'\epsilon'' = 0 \quad (3.4)$$

and

$$\begin{aligned} \frac{\mu'\epsilon' + \mu''\epsilon''}{\epsilon'^2 + \epsilon''^2} &= -z''^2 \\ \mu'\epsilon' &= -z''^2(\epsilon'^2 + \epsilon''^2) - \mu''\epsilon'' \end{aligned} \quad (3.5)$$

Since z''^2 is certainly a positive number and ϵ'' & μ'' are positive due to the passive nature of medium, therefore it can be concluded that,

$$\mu'\epsilon' < 0 \quad (3.6)$$

Equations 3.4 and inequation 3.6 are the *conditions of perfect reflection* out of which the former is strict and direct while the latter is deductive. First condition is achieved when imaginary part of both μ & ϵ are zero while the second one needs the real parts of ϵ and μ to be of opposite signs.

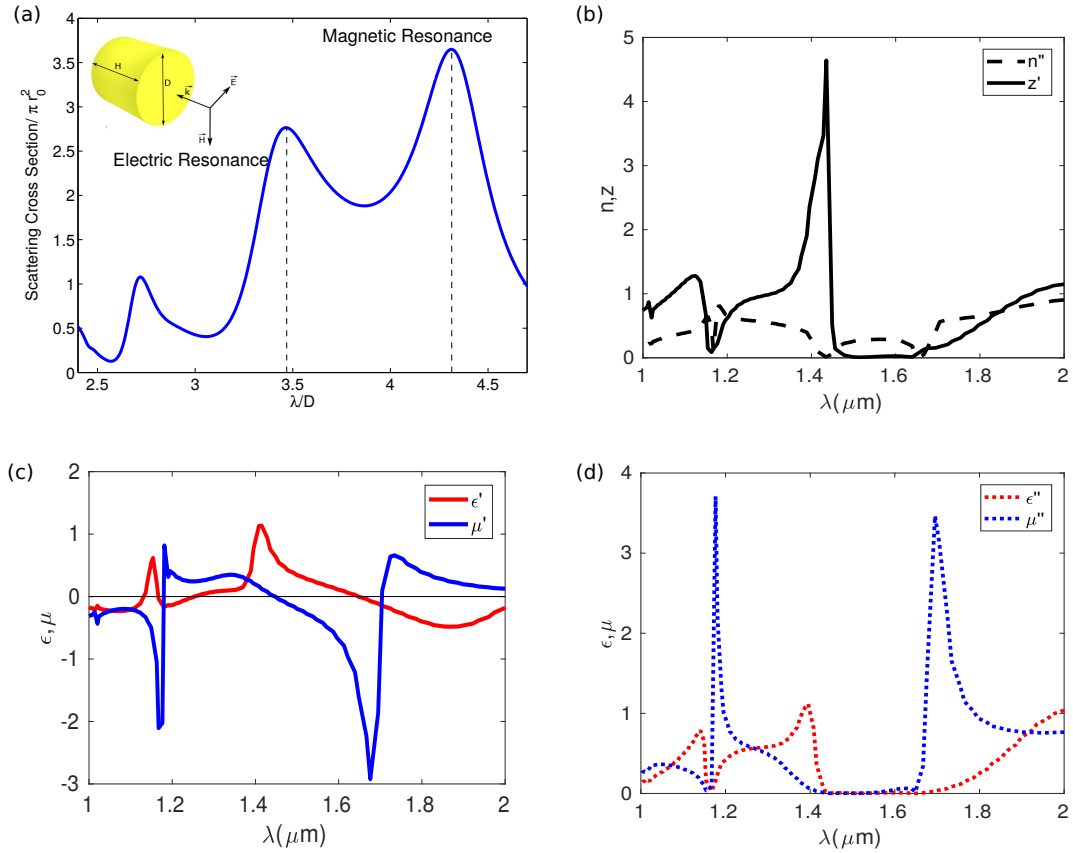


Figure 3.3: (a) Scattering cross-section vs wavelength for the silicon cylinder with diameter $D = 420$ nm and height $H = 525$ nm. Inset: geometric dimensions of the cylinder and the direction of incidence of the external wave; (b) real and imaginary parts of the effective permittivity ϵ' and the effective permeability μ' ; (c) real part of the effective impedance z' and imaginary part of the effective refractive index n''

3.3 Design and numerical analysis of metasurface based cavity

Firstly, to determine the value of diameter of the cylinder (D), in order to achieve resonance at the desired wavelength, scattering cross-sections of the silicon cylinder has been calculated at different values λ/D . The results are shown in figure 3.3. Here, the peaks at $\lambda/D = 3.47$ and $\lambda/D = 4.3$ correspond to electric and magnetic dipole resonances, respectively (according to figure 1(b) in Ref. [61] for the aspect ratio equal to 1.25). The plot indicates that in order to achieve electric resonance at the desired wavelength (1500 nm in this case), the diameter D should be equal to $\lambda/3.5$. The numerical analysis has been performed in COMSOL Multiphysics. Data for permittivity of silicon ϵ has been taken from Palik [63]. The imaginary part of permittivity has been ignored due to its negligibly small value for crystalline

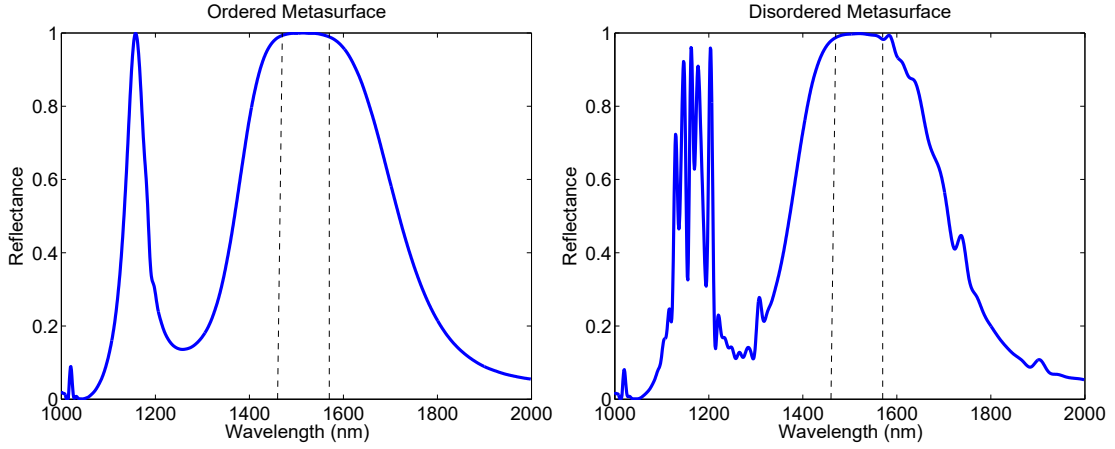


Figure 3.4: (a) Reflectance vs wavelength for first metasurface reflector. (b) Reflectance vs wavelength plot for second reflector.

silicon in the considered spectral range (1000-2000 nm) and only real part has been considered. Figure 3.1(b) shows the scheme of the ordered metasurface. The unit cell of the metasurface is the silicon cylinder designed above. Based on the above analysis, the diameter of the cylinder (D) is chosen to be 420 nm, height (H) is 525 nm (aspect ratio = 1.25) and periodicity (a) of the metasurface is 700 nm. The structure can be tuned to achieve perfect reflection at different wavelengths by varying the height of the cylinder. In figures 3.3(b-d), effective material parameters obtained by field averaging [87] are shown. The results clearly illustrate the presence of the electric resonance around 1600 nm. As a result of which, a region of nearly zero effective impedance is obtained between 1480 nm and 1640 nm. This band of extremely low effective impedance is the main cause of the perfect reflection [85]. Furthermore, a small peak in the imaginary part of the effective refractive index eradicates the possibility of leakage of power through the metasurface. The extremely low effective impedance is attributed to the fulfillment of the two conditions of perfect reflection in the said wavelength range. Figures 3.3(c) & (d) respectively show that between 1480 and 1640 nm real parts of relative permittivity are of opposite signs, satisfying equation 3.6 and imaginary parts are negligibly small validating equation 3.4.

For a laser cavity, the linewidth $\Delta\nu = \nu_0/Q$, and the quality factor Q can be written as (as shown in Ref [28])

$$Q = \frac{4\pi\nu_0 n_0 d}{c(2\alpha d - \ln(R_1 R_2))} \quad (3.7)$$

where ν_0 is the frequency of the mode, n_0 is the refractive index of the medium inside cavity, d is the length of the cavity, R_1 is the reflectance of the first mirror, R_2 is the reflectance of the second mirror, α is the losses due to other factors except finite reflectivity of the mirrors. Thus, to achieve very high values of quality factor

Q the first reflector should have reflectance R_1 as close to 1 as possible (ideally $R_1 = 1$). In other words, it should be a perfectly ordered two dimensional periodic array (see Figure 3.1(b)). Figure 3.4(a) shows the reflectance versus wavelength graph of the metasurface array which shows that $R_1 = 0.9999$ in the wavelength range from 1490 nm to 1530 nm.

Second reflector should be slightly transmitting with reflectance $\sim 99\%$ but not less than it. Because the quality factor depends upon the product of R_1 and R_2 according to Eq. (3.7), lowering R_2 will reduce Q as well. So, the reflectance of second reflector needs to be controlled in a very precise manner. An easy way to do this is to deliberately introduce a small disorder in the periodic arrangement of the structure (as it has been shown in Ref. [61]). The proposed design of second reflector is shown in Figure 3.1(c). Percentage disorder can be defined as standard deviation of the distance of a cylinder from the four neighboring cylinders divided by periodicity a of perfectly ordered array multiplied by 100. In this case, if Δ is the small offset introduced in the position of every 1 out of 4 cylinders, then, $r_3 = \sqrt{(a - \Delta)^2 + \Delta^2}$, $r_4 = r_3$, $r_1 = \sqrt{(a + \Delta)^2 + \Delta^2}$, $r_2 = r_1$. Hence mean $\bar{r} = (r_1 + r_2 + r_3 + r_4)/4$, standard deviation $\sigma = \sqrt{[(r_1 - \bar{r})^2 + (r_2 - \bar{r})^2 + (r_3 - \bar{r})^2 + (r_4 - \bar{r})^2]}/4$, and disorder is $100\sigma/a$. For $\Delta = 70$ nm and $a = 700$ nm, we get $r_1 = r_2 = 773.17$ nm, $r_3 = r_4 = 633.87$ nm, $\sigma = 69.65$ nm and disorder=9.94%. Figures 3.4(a) and 3.4(b) show the reflectance of the first and the second reflector respectively at different wavelengths.

Using the proposed designs of two reflectors it is possible to create a very high quality cavity. Figure 3.1(a) shows the design of proposed metasurface-based cavity. It should be noted that the medium surrounding the cylinders has been intentionally chosen to be air for that sake of computational simplicity, however, low refractive index material like silica can also be used here, with slight modification in design parameters. Thickness of the active medium has been chosen to be $\lambda/2n_0$, where λ (1500 nm in this case) is the wavelength of operation and n_0 is the refractive index of the active medium. According to Ref. [81], for the wavelength range 920 nm – 1700 nm, a double heterostructure of InP/In_{1-x}Ga_xAs_yP_{1-y}/InP can be used as the active medium, where InP is the confining layer and In_{1-x}Ga_xAs_yP_{1-y} acts as the active layer. According to Ref. [39], to minimize lattice mismatch between InP and In_{1-x}Ga_xAs_yP_{1-y}, $x \approx 0.466y$. In this way, beside λ , refractive index depends on y only. For $y = 0.6$, the refractive index (n_0) of intrinsic In_{1-x}Ga_xAs_yP_{1-y} is 3.43 [39]. The refractive index of the confining layer InP is 3.17 [63].

Figure 3.5(a) shows the normalized electric field distribution profile inside the cavity and figure 3.5(b) shows intensity distribution along the length of the cavity. Figure 3.5(c) shows the quality factor of the metasurface laser cavity at different wavelengths with a maximum of 2630 at 1500 nm.

While talking about the performance of a laser it is necessary to discuss its threshold gain coefficient g_{th} . For lasing $g_{th} = \alpha + \alpha_R$, where $\alpha_R = -\ln(R_1 R_2)/2d$

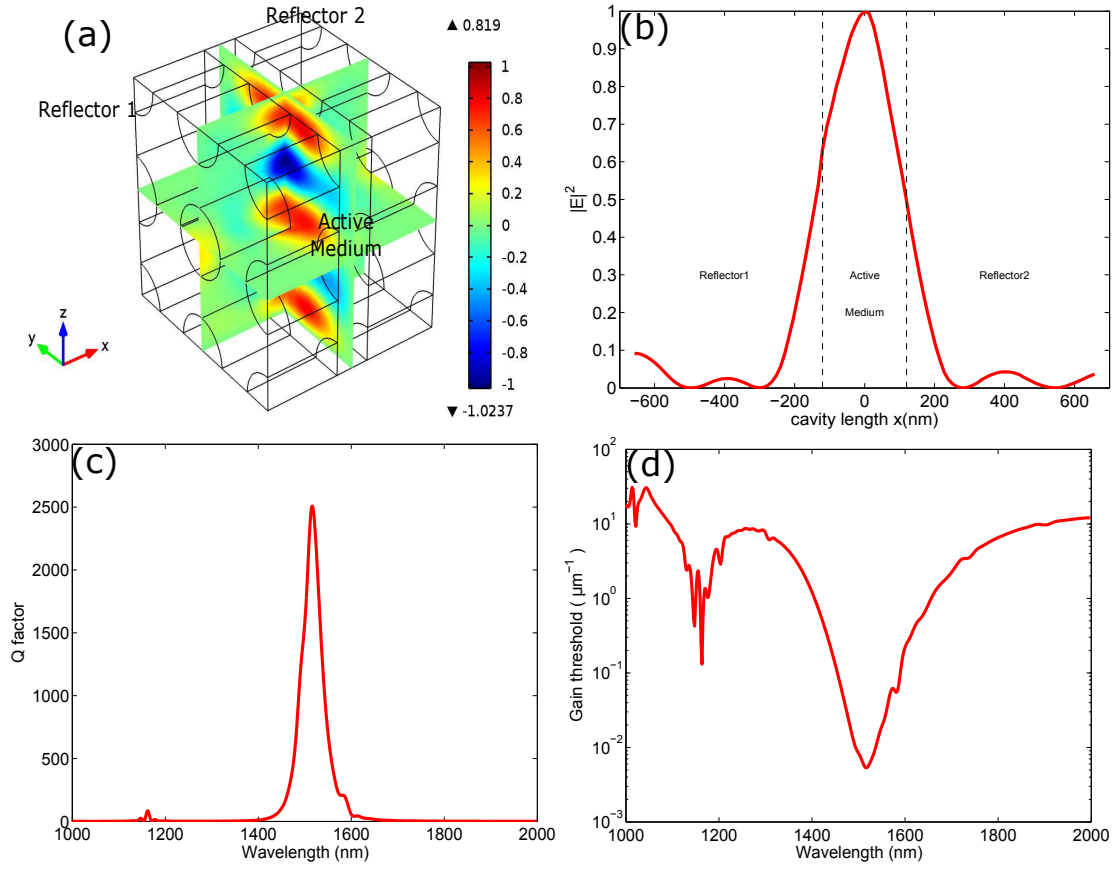


Figure 3.5: (a) Distribution of the normalized electric field inside the cavity at $\lambda = 1500$ nm and (b) variation of normalized E^2 along the length of the cavity. (c) Quality factor and (d) threshold gain coefficient of Metamaterial Laser Cavity at different wavelength.

is the loss due to finite reflectivities of the mirrors and α is loss attributed to other factors (including diffraction, dissipation, etc) which can be ignored for the sake of simplicity. Hence, threshold gain coefficient becomes [81]:

$$g_{\text{th}} = -\frac{\ln(R_1 R_2)}{2d} \quad (3.8)$$

According to Eq. (6.12), at 1500 nm threshold gain coefficient $g_{\text{th}} = 0.00557 \mu\text{m}^{-1}$. In figure 3.5(d), the variation of threshold gain coefficient is shown.

3.4 Comparison with Bragg reflector based cavity

After performing such an involved analysis, it is worthwhile to compare the reported design with a Bragg reflectors based cavity. The Bragg reflector is a stack

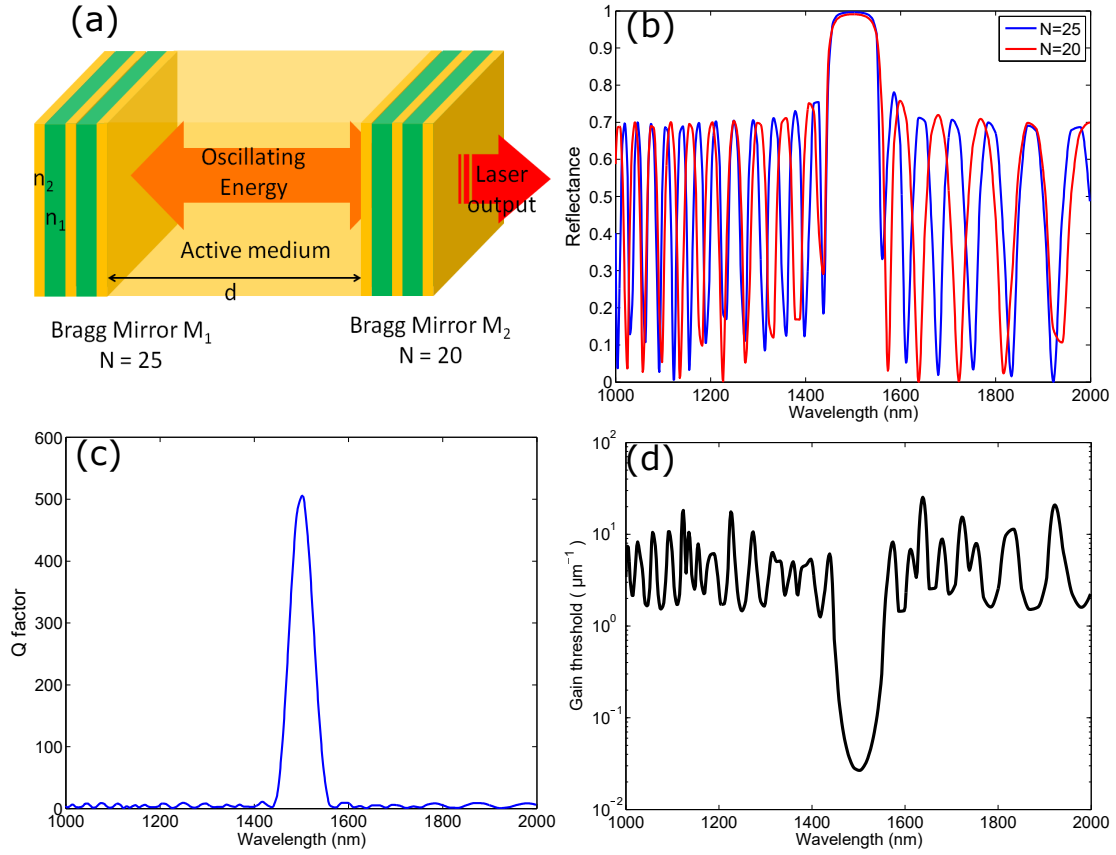


Figure 3.6: (a) Design of Bragg Cavity. (b) Reflectance for both Bragg mirrors, (c) quality factor and (d) threshold gain coefficient for the laser cavity at different wavelengths.

of alternating layers of a high refractive index material and a low refractive index material with high refractive index layers at both the ends. Bragg reflector is an excellent reflector with negligible losses because it is made up of dielectrics only. Here, it has been proven that the metasurface perfect reflector has the upper hand because its single layer can provide reflectance equivalent to what is achieved by >25 layers Bragg mirror.

Let us consider a Bragg mirror made up of alternating layers of AlAs ($n_1 = 2.9$) and $\text{Al}_{0.1}\text{Ga}_{0.9}\text{As}$ ($n_2 = 3.57$). For maximum reflection, quarterwave thickness of AlAs and $\text{Al}_{0.1}\text{Ga}_{0.9}\text{As}$ layers are respectively given by: $t_1 = \lambda_0/4n_1$ and $t_2 = \lambda_0/4n_2$. In this way, we get that $t_1 = 130$ nm and $t_2 = 105$ nm. Active medium is again $\text{In}_{1-x}\text{Ga}_x\text{As}_y\text{P}_{1-y}$ (refractive index $n_0 = 3.43$) and length of the cavity $d = \lambda/2n_0$. Generally, for functionality as a resonator for laser cavity, 25-30 pairs stack is used to make mirror M_1 and 20-25 pairs stack is used to make mirror M_2 . In this case, $N = 25$ for M_1 and $N = 20$ for M_2 have been chosen. Figure 3.6(a) shows the design of the Bragg cavity, figure 3.6(b) shows the reflectance vs wavelength graphs for both mirrors, figure 3.6(c) shows the quality

factor of the cavity and figure 3.6(d) shows variation of threshold gain coefficient at different wavelengths. According to the calculations, at 1500 nm quality factor is 505 and threshold gain coefficient g_{th} is $0.0267 \mu m^{-1}$.

3.5 Effect of Substrate

As it has already been mentioned above, that during the entire analysis the cylinders have been assumed to be surrounded by air, which may not be the case in a practical situation. An experimenter may feel the need of embedding the resonators in a low index medium for practical feasibility. Hence, it is interesting as well important to investigate whether the perfect reflecting properties persist if the refractive index (n_s) of the surrounding is greater than 1. For this purpose, optimization analysis has been performed for the variation of n_s from 1.1 to 1.6 and the corresponding 2D plots have been presented in figure 3.7, which provide a range of values of diameter D and period a to achieve perfect reflection. The color bar in figure 3.7 represents reflectance which can vary from 0.0 to 1.0. The more yellow color means closer to 1 value of reflectance. In all the six plots, it can be seen that there is ample amount of high reflectance region (yellow region) but the range of values on x and y axes is different in each one of them. It implies that 100% reflection is easily realizable for each of the six values of n_s , the only difference being in the range of suitable values of diameter D and period a , which must be appropriately selected.

Besides, if one can get a bit more ambitious, the thin film technology compatible ultra-low refractive index materials can also be employed, which mimic the effect of air as the surrounding medium. These are basically nanorods films which have been reported to exhibit refractive index as low as 1.08 (close to that of air) [79, 80, 102]. They have been strong enough to hold solid layers of homogeneous material on their top, which is a clear indication of their mechanical stability. In spite of all these merits, their utility in the present application is still uncertain and needs experimental verification. Hence, homogeneous materials of low refractive index such as silica (SiO_2 , $n \approx 1.5$) are more reliable choices for fabricating a metasurface perfect reflector based cavity.

3.6 Conclusion

The above analysis clearly shows that quality factor achieved using metasurface reflector is 5 times higher and threshold power is 80% lesser than that using Bragg reflector. Since line-width is inversely proportional to quality factor [28], the higher quality factor also results in reduced line-width and improved monochromaticity. But most importantly, the design of the metasurface cavity is more compact with just a single layer of dielectric cylinders compared to 20-25 layers of dielectric pairs in case of the Bragg cavity. It should be noted that such impressive results

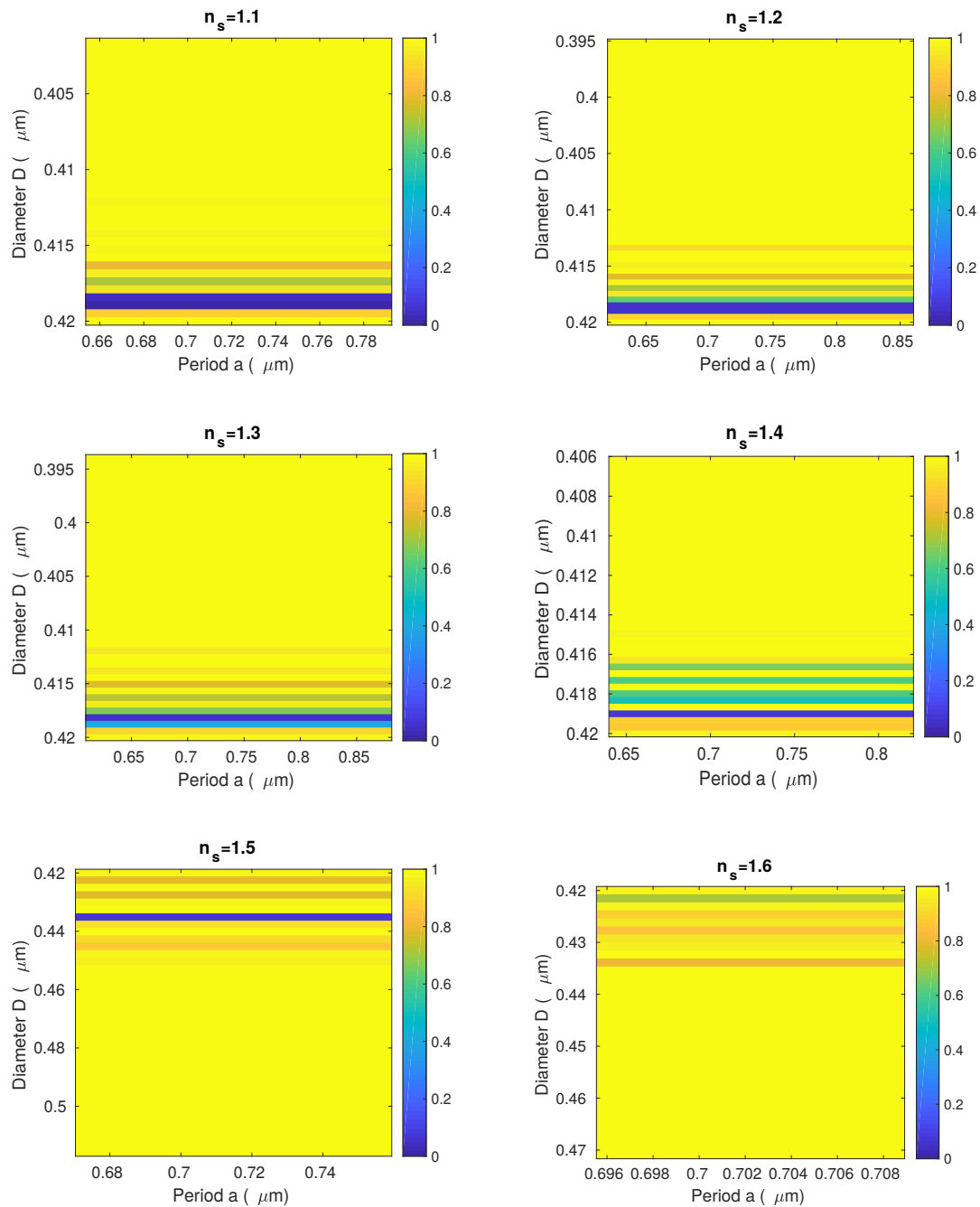


Figure 3.7: Optimization plots for geometrical parameters corresponding to 6 different values of refractive index of the surrounding medium (the color bar indicates reflectance R).

could be seen because the dissipation losses in the Silicon are insignificantly small due to negligible value of its extinction coefficient κ , hence no ohmic loss, around 1500 nm. If the metasurface had been designed for visible spectrum, dissipation

loss would be large enough to deteriorate the ability of perfect reflection. It is believed that these results can be useful for the development of compact laser cavities.

Chapter 4

Split-nanotube based negative index metamaterial for midinfrared wavelengths

4.1 Introduction

IN the previous chapter a purely dielectric metamaterial has been used whose operation is based on Mie resonance and which exhibits effectively positive refractive index. Positive index seems natural and normal, however there is another interesting and attractive category of metamaterials which have effectively negative refractive index. Negative refraction is unusual but achievable if both – the permittivity and the permeability become negative at the same frequency. The idea of negative refraction was first conceived by Veselago in 1967, but his vision [99] remained unrealized for a long time due to the absence of negative permeability in nature. Magnetic response of a material is negligibly small for visible and longer wavelengths [50]. Weak magnetic response is attributed to the fact that, the coupling strength of the magnetic field component of the incident light with the atoms of a material, is $\sim 18,000$ times weaker than that of the electric field component [13]. As a result, permeability is mostly considered to be invariant with frequency. In 1981, Hardy and Whitehead [35] proposed a structure, which they called a *split-ring resonator* (SRR), to achieve magnetic resonance in a frequency range of 200 to 2000 MHz. In 1999, Pendry et al. [65] proposed a planar version of Hardy’s SRR, which showed strong magnetic resonance at low frequencies. In this way, the obstacle of achieving magnetic resonance was overcome. By combining Pendry’s SRR with metallic wire mesh, negative refraction was achieved at microwave frequency [84]. Since then, SRR has been a popular choice as a magnetic meta-atom and has been used in large numbers of metamaterial structures. However, at optical frequencies, SRRs become inefficient due to two main reasons. The first one is the fact that a metal ceases to behave as a perfect conductor at optical frequencies. The second one is the condition that the magnetic field vector should

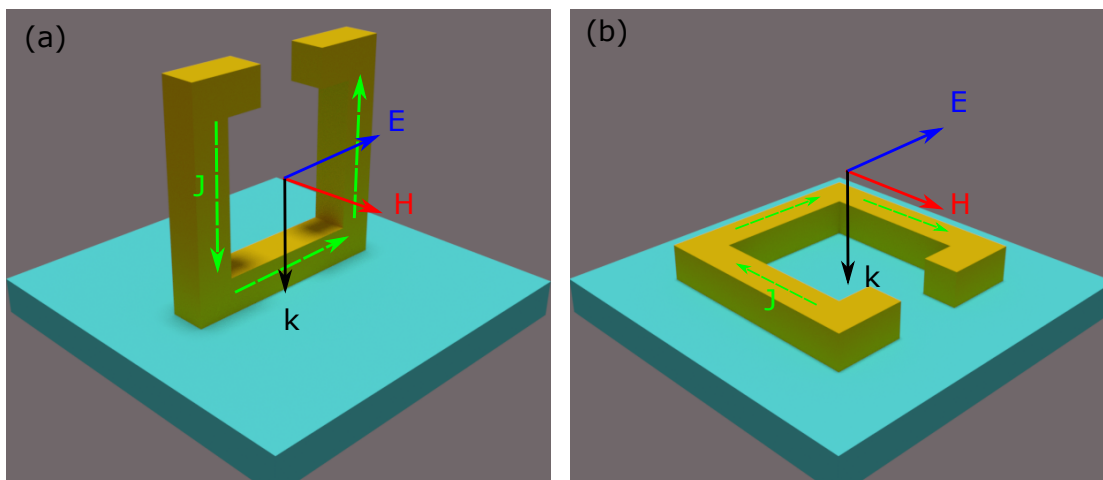


Figure 4.1: Two types of orientations of an SRR to be fabricated on a substrate by lithography: (a) shows strong response but is difficult to fabricate and (b) shows weak response but is easy to fabricate.

be normal to its cross section for proper operation, which is extremely difficult to be met in case of a nanostructure being fabricated on a substrate by lithography (see figure 4.1 for better visualization). The orientation shown in figure 4.1(a) is extremely difficult to realize. But the planar structure shown in figure 4.1(b) can be easily fabricated. In 2004, Yen et al. [104] developed a magnetic metamaterial based on planar SRRs, which resonated at 1 THz. The resonance was not very strong, and maximum value of negative permeability achieved was -1. Later that year, Linden et al. [55] fabricated a similar metamaterial with smaller SRRs and pushed the resonance frequency to 100 THz. The maximum value of negative permeability achieved by them was -0.5. As a result, other types of structures, such as paired nanostrips [107], were explored leading to the development of fishnet type metamaterials [23, 98, 72]. Using fishnet metamaterials, negative index has been achieved at telecom wavelengths. Several works have reported the value of negative refractive index from -0.5 to -2. There is also an entirely different breed of negative index metamaterials (NIMs) whose operation is based on Mie resonance [101]. But magnetic resonance shown by them is weak, the value of negative permeability is humble (~ -0.5) and the negative refractive index achieved is ~ -1 .

In this chapter, a split-nanotube-based NIM (shown in figure 4.2) has been proposed for which the minimum value of the negative refractive index is -2 and the figure of merit (FOM) is 8 at $3 \mu\text{m}$. It is easy to have a magnetic field oriented along the axis of a split-nanotube, hence its resonance is stronger than that of a planar SRR and on account of being tubular in shape, its fabrication is much easier than that of an upright SRR. Hence, the performance of the proposed structure is superior to that of SRR and Mie resonance-based NIMs but comparable to that of fishnet structures. The proposed structure has been designed for infrared

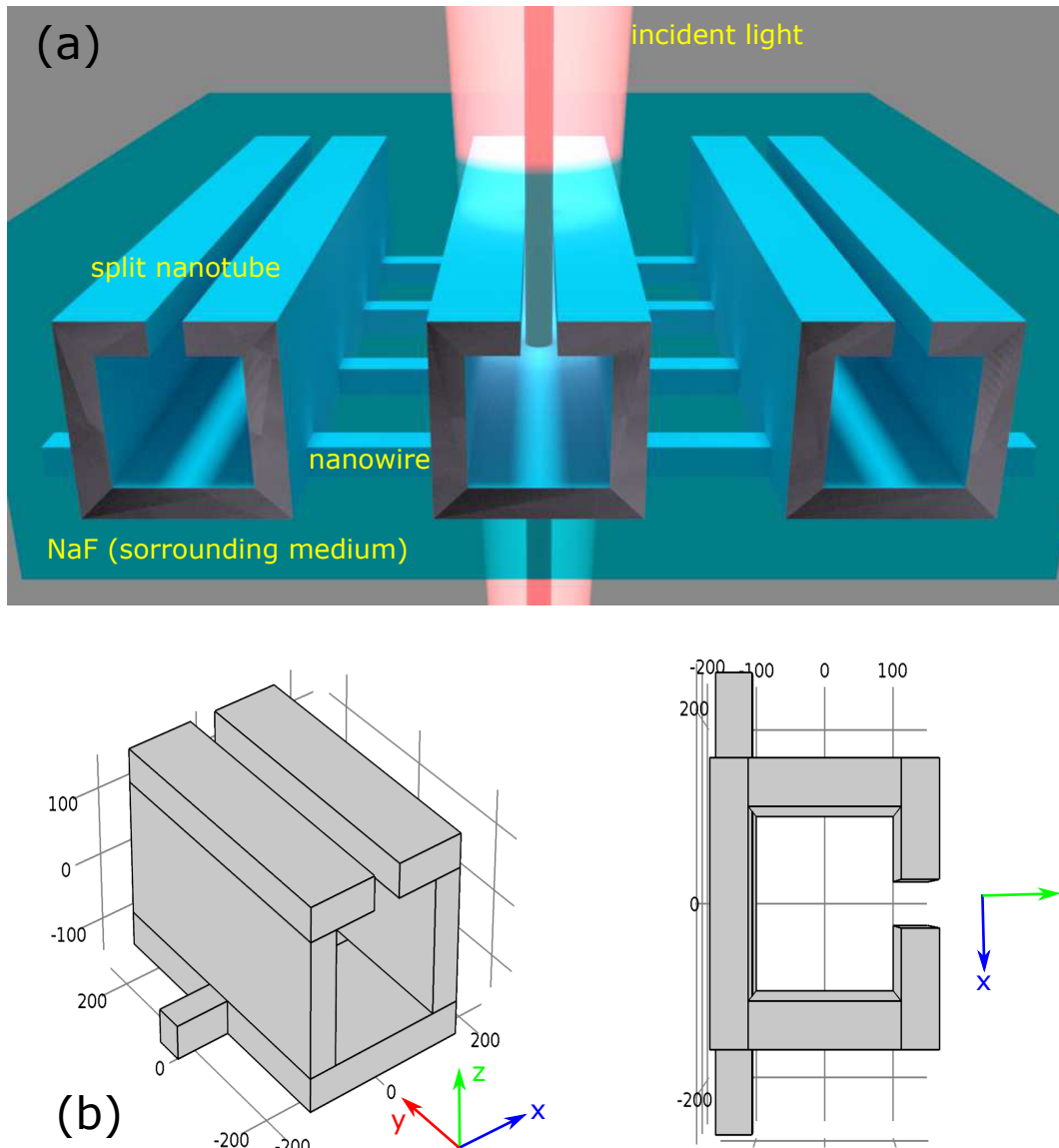


Figure 4.2: (a) Schematic diagram of the proposed metamaterial made up of a two-dimensional array of split-nanotubes and nanowires and (b) three-dimensional unit cell used for numerical analysis.

wavelength because this part of the spectrum is still unused and unexplored. The proposed metamaterial can be a basis for the development of infrared imaging systems, secured wireless communication systems, sensors, perfect lensing, etc.

4.2 Design

It is well known that a split ring can be represented by an equivalent LCR circuit. For split ring of a finite thickness, similar to the one shown in figure 4.3(a), the

capacitance C can be approximately determined by relating it to a parallel plate capacitor and the inductance L can be estimated by relating it to a solenoid [31, 92]. Hence,

$$C = \epsilon_0 \epsilon \frac{wt}{g} + \epsilon_0 \epsilon (t + w + g) \quad (4.1)$$

$$L = \mu_0 \frac{l_x l_y}{t} \quad (4.2)$$

and the resonant frequency,

$$f_0 = \frac{1}{2\pi} \frac{1}{\sqrt{LC}} \quad (4.3)$$

where ϵ stands for the permittivity of the material in the gap. The second term in equation 4.1 represents the fringe capacitance [92]. Equation 4.2 is a bit inaccurate for a split ring whose thickness is small compared to its side length since it is valid only for a long solenoid [31]. However this limitation proves beneficial in our case because for a split nanotube thickness t is very large compared to side length l_x or l_y . Figure 4.2 shows the proposed metamaterial made up of split-nanotube and nanowire mesh. Split-nanotube acts as a magnetic meta-atom and nanowire mesh provides negative permittivity. While deciding the geometrical parameters of splitnanotubes and nanowires, Drude's model of permittivity of metals has been considered. The penetration depth of light in noble metals at optical frequencies is ~ 50 nm. For particles smaller than 50 nm, the damping factor of Drude's model does not remain a constant and a correction factor has to be introduced [13] which makes the damping factor dependent on the size of the particle. Hence for convenience of assuming a constant damping factor, w has been chosen to be 50 nm. The line-width of each nanowire has also been set to 50 nm for the same reason. Besides, a line-width of 50 nm can be accurately achieved by lithography. The gap g has been chosen to be 50 nm, purely on the basis of ease of fabrication using lithography. The side lengths l_x and l_y have been strategically taken to be equal to 300 nm each in order to achieve resonance in mid-infrared region around $3 \mu\text{m}$. Periodicities of both the splitnanotubes and the nanowires have been optimally taken to be 500 nm. The structure has been optimized with respect to periodicity to achieve minimum value of refractive index at $3 \mu\text{m}$. It turns out that for periodicity of 500 nm refractive index is minimum i.e. -2.078 at $3 \mu\text{m}$. Periodicity has been taken to be same in all 3 directions for the sake of simplicity. The splitnanotube and nanowires are made up of silver because it is least lossy among the metals and the surrounding medium is NaF ($n = 1.32$) because it is transparent and practically lossless in the considered wavelength range. Figure 4.3(b) illustrates all the geometrical & material parameters of the proposed metamaterial structure and the polarization & the direction of propagation of the incident wave. Figure 4.3(c) shows the variation of resonant frequency of the split ring with respect to thickness t keeping $l_x = 300$ nm. It should be noted that when $t \gg l_x$ resonant wavelength becomes a constant and independent of t . In this way according to equations 4.1 – 4.3 and figure 4.3(c) the resonant wavelength of the

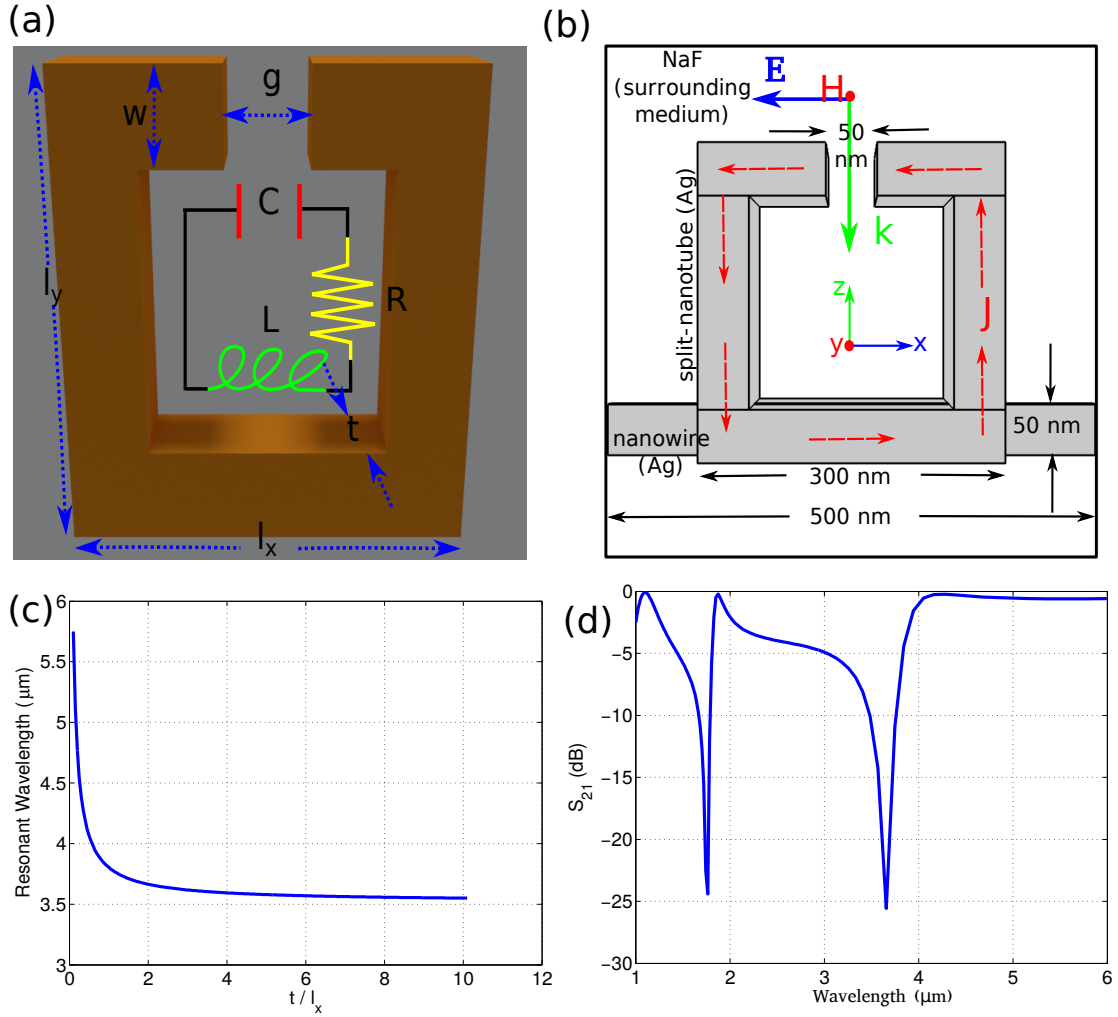


Figure 4.3: (a) A split ring of a finite thickness with equivalent LCR circuit. (b) Cross-sectional view of a unit cell of the proposed metamaterial displaying all the geometrical and material parameters. (c) Variation of resonant wavelength with thickness t keeping l_x a constant. (d) Variation of S_{21} parameter with respect to wavelength showing a dip at the resonant wavelength

splitnanotube is equal to 3.56 μm . For the sake of confirmation, the resonance in splitnanotube has also been analyzed numerically by performing full wave analysis in COMSOL Multiphysics® and S_{21} parameter thus obtained has been plotted with respect to wavelength in figure 4.3(d). A sharp dip is observed at 3.65 μm which indicates resonance. Hence, both the analytical and the numerical methods predict the same value of resonant wavelength i.e $\sim 3.6 \mu\text{m}$.

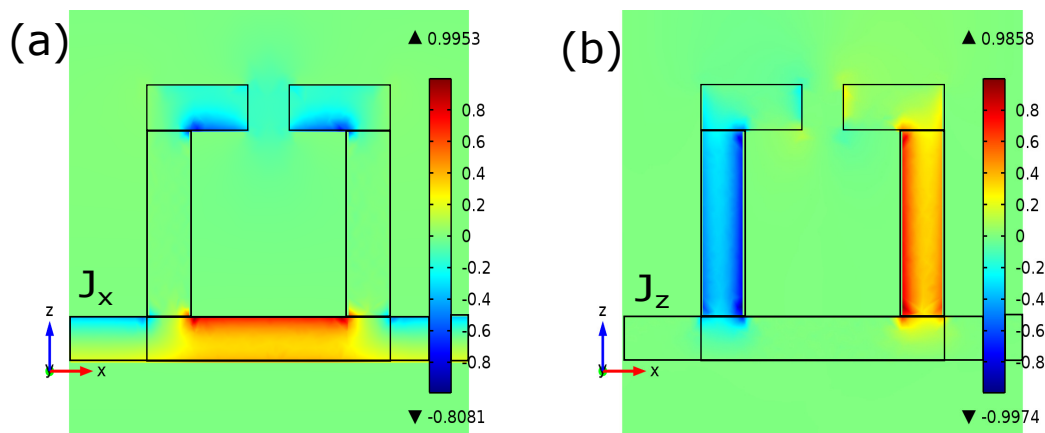


Figure 4.4: Contour plots of—(a) x component of \vec{J} and (b) z component of \vec{J} , flowing in the split-nanotube. Blue color indicates negative value and red color indicates positive value.

4.3 Numerical Analysis and Results

Full wave analysis of the unit cell has been performed in a finite element method based commercial software package COMSOL Multisphysics® and s-parameters have been obtained. Using the s-parameters, the effective material parameters have been calculated using Kramer-Kronig's relation based parameter retrieval technique [93]. During the simulation, the \vec{H} field of the incident wave was parallel to the axis of the tube (y direction), the electric field \vec{E} was aligned along the length of wires (-x direction) and the direction of propagation was along -z direction as shown in figure 4.3.

Figure 4.4 shows the contour plots displaying volume current density \vec{J} flowing in the split-nanotube at $3 \mu\text{m}$, in which, figure 4.4(a) shows the x-component of \vec{J} and 4.4(b) shows the z-component of \vec{J} . Looking at figure 4.4, it is easy to understand that current is circulating in anticlockwise direction which implies that the induced magnetic field \vec{B} is directed along the negative y direction (opposite to the incident \vec{H} field). This behavior obviously gives rise to negative effective permeability at $3 \mu\text{m}$ which is reflected in figure 4.5(c).

For a better understanding of the material properties, effective parameters have been calculated from s-parameters and are shown in figure 4.5. Figures 4.5(a) and (b) respectively show the variation of magnitude and phase of the S_{11} and S_{21} with respect to wavelength. It can be noted that phase of S_{21} is negative at $3.3 \mu\text{m}$ and below, till $1.5 \mu\text{m}$. This means that, light undergoes a negative phase change as it travels through the unit cell which is a good sign for negative refraction to take place. Figures 4.5(c)–(f) show the effective material parameters — permeability (μ_{eff}), permittivity (ϵ_{eff}), refractive index (n_{eff}) and figure of merit ($fom = |Re(n_{eff})/Im(n_{eff})|$) obtained at different wavelengths using the retrieval technique [93]. In the permeability curve, magnetic resonance can be

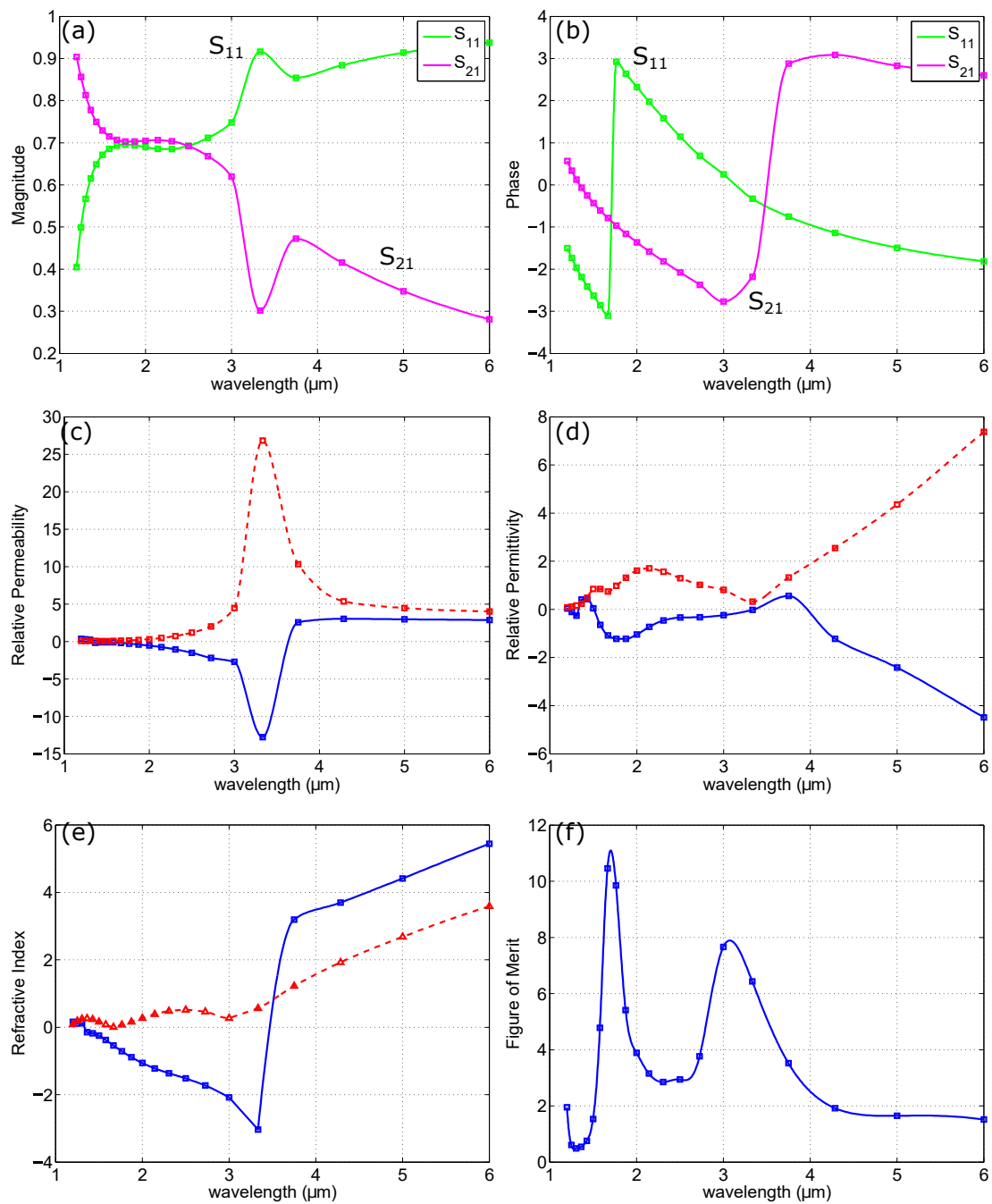


Figure 4.5: Effective material parameters obtained. Real part is shown in blue solid curve and imaginary part is shown in red dashed line.

noticed around $3.3 \mu\text{m}$ with negative permeability between $1.5 \mu\text{m}$ and $3.3 \mu\text{m}$. Minimum negative value of real part of μ_{eff} is -12.77 at $3.3 \mu\text{m}$. However no resonance is observed in the permittivity curve, as the chosen wire mesh structure is non-resonant in the wavelength range under consideration. Nevertheless, negative

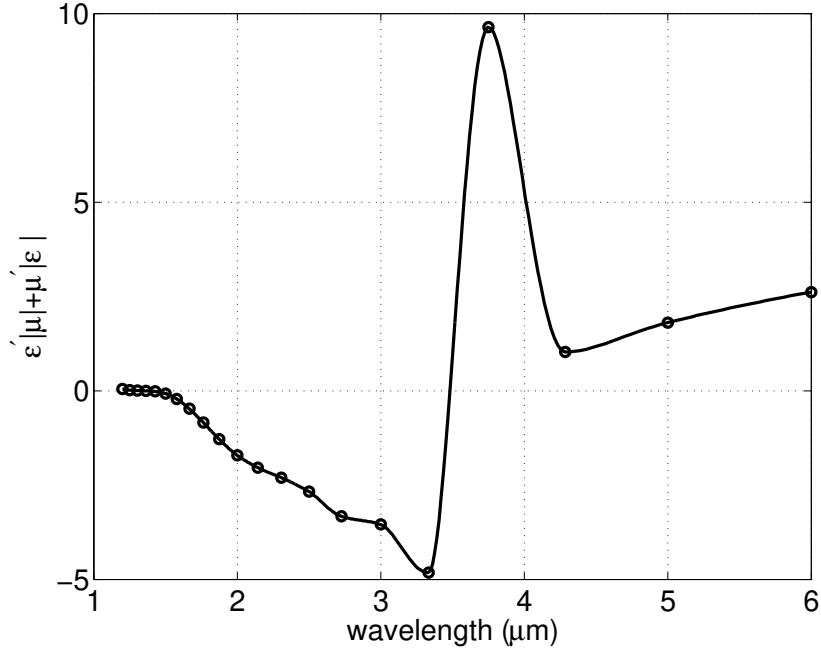


Figure 4.6: Condition of negative refraction [21]

permittivity is achieved owing to the peculiar natural property of metals of showing negative permittivity below their plasma frequency. Now, as a consequence of simultaneously negative μ_{eff} and ϵ_{eff} , refractive index (n_{eff}) of the metamaterial is also negative between $1.5 \mu\text{m}$ and $3.3 \mu\text{m}$ with the maximum negative value equal to -3.03 at $3.3 \mu\text{m}$. At $3 \mu\text{m}$ FOM is high ~ 8 which indicates low extinction coefficient of the metamaterial. It should be noted that though the refractive index is most negative at $3.3 \mu\text{m}$, the metamaterial can perform the best at $3 \mu\text{m}$ due to high value of the figure of merit. At $3 \mu\text{m}$ refractive index is -2.078 . A high value of fom (~ 11) is also observed at $1.7 \mu\text{m}$, but it is insignificant due to the low value of real part of n_{eff} (~ 0.53) at that wavelength. Hence, it is observed that at $3 \mu\text{m}$ the metamaterial exhibits substantially negative refractive index with high figure of merit.

Now, in order to reinforce the above inference, it has been proved that the condition of negative refraction, holds good for the proposed metamaterial. For a metamaterial to have negative phase velocity, $\epsilon'|\mu| + \mu'|\epsilon| < 0$ [21]. Figure 4.6 shows the variation of $\epsilon'|\mu| + \mu'|\epsilon|$ with respect to wavelength and proves that the condition for negative refraction is satisfied between $1.5 \mu\text{m}$ and $3.3 \mu\text{m}$.

Any discussion of NIM is incomplete without the visualization of negative refraction actually taking place. For this purpose a wedge of the metamaterial has been constructed and light ($\lambda = 3 \mu\text{m}$) is launched from one of its sides. As light travels from the metamaterial to air, most of it emerges at the same side of the normal as the incident wave as shown in figure 4.7(a). Moreover, the NIM wedge has been compared with a similar wedge of positive index ($n=2.078$) dielectric

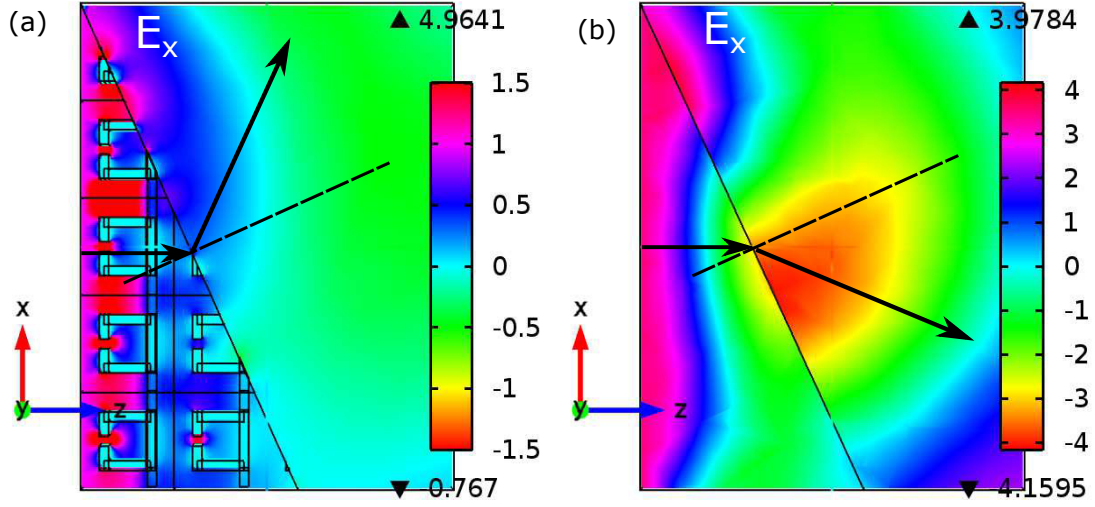


Figure 4.7: Contour plots of x-component of the electric field for—(a) Negative refraction as light travels from a wedge of proposed metamaterial. (b) Normal refraction in case of a similar positive index dielectric wedge

material as shown in figure 4.7(b). In case of positive index material (PIM) wedge intensity on the right-hand side of the normal is greater than that on the left-hand side.

4.4 Conclusion

Based on all the above analysis and results, it can be stated that the proposed metamaterial successfully functions as negative index medium at $3 \mu\text{m}$ (mid-infrared). Split-nanotubes acting similar to SRRs, play a major role in imparting the left-handed functionality to the structure. The value of $Re(n_{eff})$ is significantly negative and fom is sufficiently high. Moreover, in comparison to an upright SRR, split-nanotube is easier to fabricate and its magnetic response is much stronger than that of a planar SRR. All these factors prove that the proposed metamaterial can be a good choice as NIM in mid-infrared spectrum.

Chapter 5

All dielectric metamaterial perfect absorber for terahertz spectrum

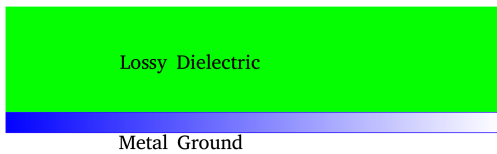
5.1 Introduction

IN the previous two chapters, two distinct types of metamaterials were put to showcase. One of them was purely dielectric and has positive refractive index (chapter 3), the other one is a metal-dielectric composite and shows negative refractive index (chapter 4). A common thing between the two, is the minimization of resistive loss. The purpose of using a purely dielectric metasurface in a laser cavity was to avoid ohmic loss and enhance quality factor. Similarly in the split nanotube metamaterial the frequency corresponding to minimum ohmic loss, hence, highest figure of merit was chosen for operation. In both the designs, the ohmic loss was an impediment in performance, hence undesired. However, in this chapter, the resistive loss becomes useful to achieve high absorption by means of a lossy dielectric whose working is based on the Mie resonance.

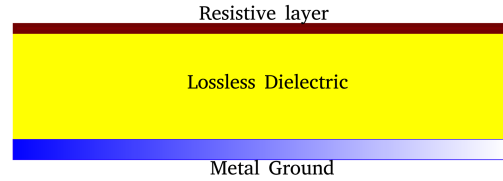
Mie resonance based metamaterials have been deeply explored in the past few years. Particles of high permittivity are suitably arranged to achieve desired functionality at the desired wavelength. Material of the particles is chosen depending upon the wavelength of operation. To achieve Mie resonance at telecom wavelength and in near infrared spectrum silicon is the most common choice. In terahertz spectrum, materials like lithium tantalate (LiTaO_3), silicon carbide (SiC), polycrystalline titanium oxide (poly- TiO_2), cuprous chloride (CuCl), are more suitable. Whereas particles made up of barium strontium titanate ($\text{Ba}_{0.5}\text{Sr}_{0.5}\text{TiO}_3$, BST) have been reported to show Mie resonance in microwave spectrum. Dielectric metamaterials and metasurfaces designed and fabricated so far have a broad range interesting applications including - negative refraction, shaping of the wavefront, electromagnetic transparency, electromagnetic cloaking, perfect reflection, perfect absorption, subwavelength confinement, realization of zero index, etc. Moreover,

highly directive all dielectric nanoantennas including Yagi-Uda nanonantenna, have also been reported in the past few years.

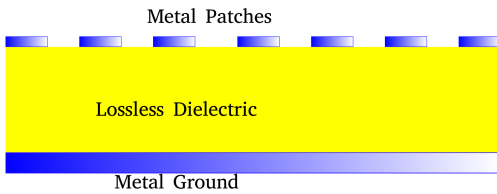
(a) Dallenbach absorber



(b) Salisbury absorber



(c) Conventional metamaterial absorber



(d) Proposed metamaterial absorber

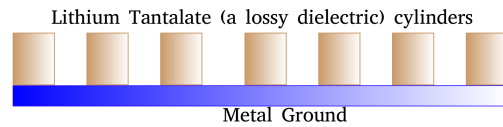


Figure 5.1: Different types of absorbers

This chapter is dedicated to the property of perfect absorption. The concept of electromagnetic wave absorbers is not new. There have been Dallenbach [19] and Salisbury [77] absorbers employed to absorb microwaves, for about a century. Dallenbach absorber is simply made up of a layer of lossy dielectric laid on a metal ground plane while Salisbury absorber consists up of a lossless dielectric layer sandwiched between a resistive layer and a metallic ground plane. Figures 5.1(a) & (b) show the basic design of classical Dallenbach and Salisbury absorbers as an aid to visualization. In recent times, a large number of metamaterial perfect absorbers operating in microwave, visible and near-infrared spectrum have been reported, most of which comprise patterned metallic structures separated from a continuous metallic plane by a thin dielectric spacer layer, as shown in figure 5.1(c). Some other works have reported BST based dielectric metamaterial perfect absorbers whose fundamental principle of operation is the occurrence of Mie resonance and they work in microwave spectrum. In this chapter a LiTaO_3 based metamaterial structure (figure 5.1(d)) has been proposed which shows high absorption in the range $65 \mu\text{m}$ - $100 \mu\text{m}$ (terahertz spectrum) with maximum absorption of 99.9% at $88 \mu\text{m}$. But before getting into the technical details of the design and operation

of the proposed structure, it is necessary to discuss the basic principle of perfect absorption, which has been described in detail in the next section.

5.2 Fundamental principle of perfect absorption

A perfect absorber is the one which neither allows transmission ($T = 0$) nor reflection ($R = 0$) to take place and almost the entire incident wave is absorbed and transformed into other forms of energy such as heat. To meet these restrictions the absorber must be able to radiate only in forward direction and not in backward direction. The forward radiation from the absorber must be able to cancel the incident electromagnetic wave to ensure zero transmission. The simplest picture of an absorber that comes to one's mind is that of an infinitesimally thin sheet of a certain absorptive material. Pozar [69] demonstrated that an array of dipoles (a single layer) can only provide a maximum 50% absorption in free space, but, if it is over a ground plane the absorption efficiency can be as high as 100% for matched load resistance. On the basis of Pozar's findings, it is easy to analogously understand that a single infinitesimally thin layer of material can never act as a perfect absorber, it is bound to have a certain finite thickness.

Ra'Di et al. [71] beautifully described the conditions of perfect absorption in terms of sheet currents. Let us assume a perfect absorber made up of two parallel layers at the distance d from each other (figure 5.2). The incident wave induces current on the two sheets whose current densities are written as \mathbf{J}_1 and \mathbf{J}_2 which generate a plane wave of their own. Let the incident wave approach from the side of the sheet 1, as shown in figure 5.2, with the magnitude of the electric field as \mathbf{E}_{inc} at the sheet 2. The system will exhibit perfect absorption, only if the plane waves due to the two sheets destructively superimpose on the incident wave behind the second sheet (region 3 in figure 5.2) canceling its field and hence nullifying the possibility of transmission,

$$-\frac{\eta_0}{2}\mathbf{J}_1e^{-jk_0d} - \frac{\eta_0}{2}\mathbf{J}_2 = -\mathbf{E}_{inc} \quad (5.1)$$

and the plane waves interfere destructively with each other in front of the first sheet (region 1) to eliminate the possibility of reflection.

$$-\frac{\eta_0}{2}\mathbf{J}_1 - \frac{\eta_0}{2}\mathbf{J}_2e^{-jk_0d} = 0 \quad (5.2)$$

where η_0 is the impedance of the free space and k_0 is the wave propagation constant. On solving the above equations for \mathbf{J}_1 and \mathbf{J}_2 , it is obtained that,

$$\mathbf{J}_1 = \frac{j}{\eta_0 \sin(k_0d)} \mathbf{E}_{inc} \quad (5.3)$$

and

$$\mathbf{J}_2 = -\frac{je^{jk_0d}}{\eta_0 \sin(k_0d)} \mathbf{E}_{inc} \quad (5.4)$$

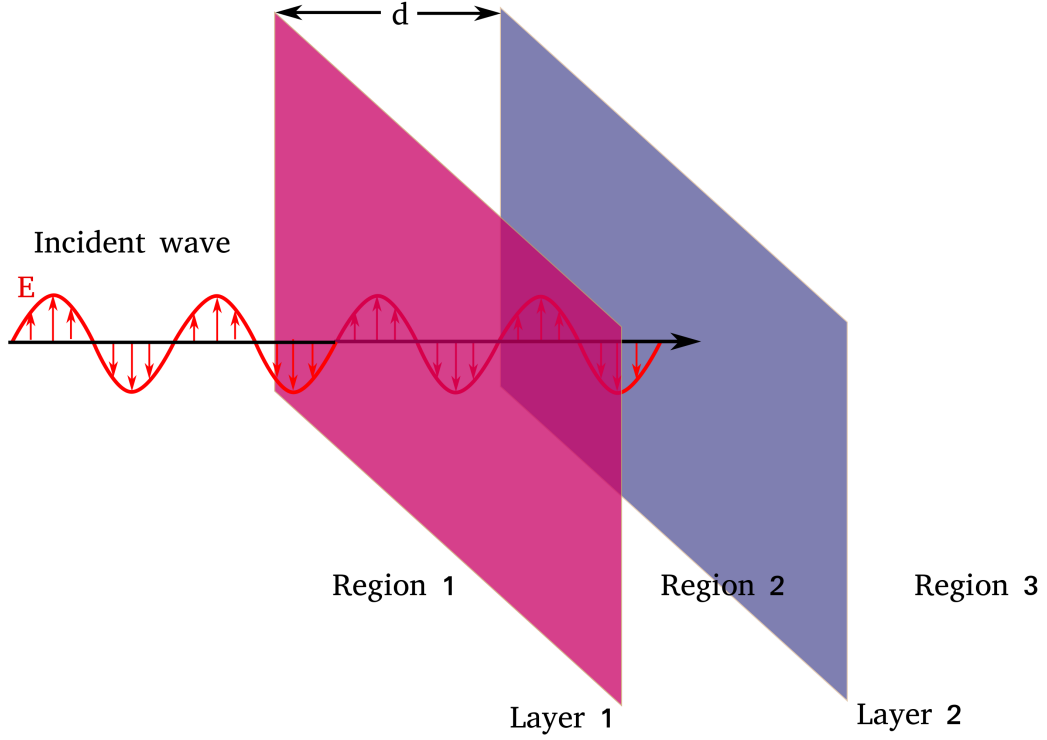


Figure 5.2: Schematic illustration of two layers acting as perfect absorber

In this way, the total field at the second sheet comes out to be

$$\begin{aligned}
 \mathbf{E}_{tot} &= \mathbf{E}_{inc} - \frac{\eta_0}{2} \mathbf{J}_1 e^{-jk_0 d} - \frac{\eta_0}{2} \mathbf{J}_2 \\
 &= \mathbf{E}_{inc} - \mathbf{E}_{inc} \\
 &= 0
 \end{aligned} \tag{5.5}$$

The total field being zero at the second sheet strictly means that the second is sheet is a *perfect electric conductor* (PEC). This is why a ground plane is present in every perfect absorber design shown in figure 5.1. Similarly, the total field on sheet 1, using equation 5.2, is

$$\mathbf{E}_{tot} = \mathbf{E}_{inc} e^{jk_0 d} - \frac{\eta_0}{2} \mathbf{J}_1 - \frac{\eta_0}{2} \mathbf{J}_2 e^{-jk_0 d} \tag{5.6}$$

$$= \mathbf{E}_{inc} e^{jk_0 d} + 0 \tag{5.7}$$

$$= \mathbf{E}_{inc} e^{jk_0 d} \tag{5.8}$$

Substituting the value of \mathbf{E}_{inc} from equation 5.3 into equation 5.8, \mathbf{E}_{tot} can be rewritten in terms of \mathbf{J}_1 as

$$\mathbf{E}_{tot} = -j\eta_0 \sin(k_0 d) e^{jk_0 d} \mathbf{J}_1 \tag{5.9}$$

$$= Z_g \mathbf{J}_1 \tag{5.10}$$

where

$$Z_g = -j\eta_0 \sin(k_0 d) e^{jk_0 d} \quad (5.11)$$

$$= -j\eta_0 \frac{\sin(2k_0 d)}{2} + \eta_0 \sin^2(k_0 d) \quad (5.12)$$

is the complex sheet impedance of the first layer. In a Salisbury absorber, the thickness of the lossless dielectric layer is $\lambda_0/4$. Substituting the value of $d = \lambda_0/4$ in equation 5.12 we get $Z_g = \eta_0 + 0j$ (purely real), which indicates that the first layer in a Salisbury absorber should be purely resistive in nature without any reactive component, which is actually the case. In fact, all the modern designs of metamaterial perfect absorbers similar to the one shown in figure 5.1(c) are advanced versions of Salisbury absorber having patterned resistive layer. However, the metamaterial perfect absorber proposed in this thesis is actually an advanced version of Dallenbach absorber where instead of a continuous layer of lossy dielectric, an array of lossy dielectric microcylinders have been used. The following sections discuss in detail, the design and operation of proposed metamaterial perfect absorber, along with a comparative study of its performance with that of a well known and commonly used high-frequency metamaterial perfect absorber.

5.3 Design and numerical analysis

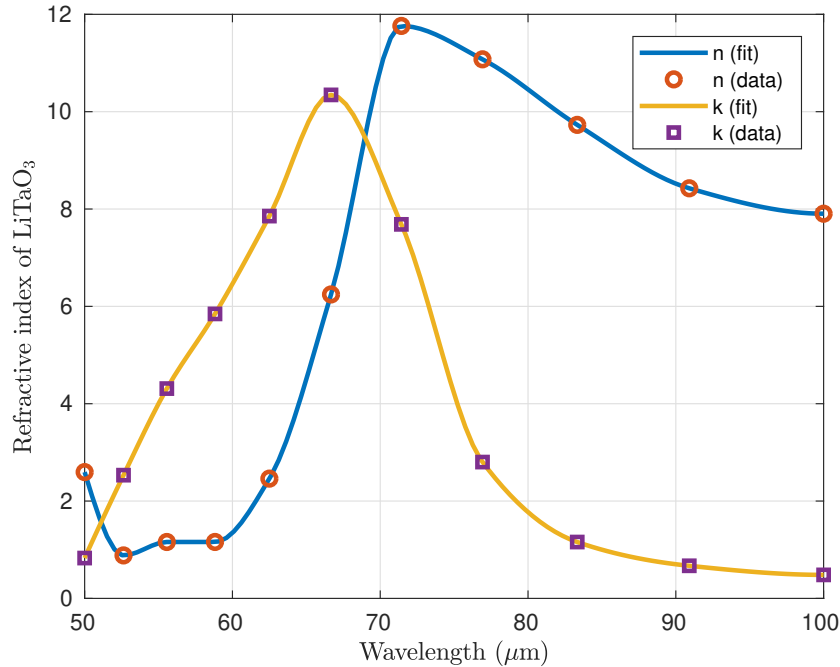


Figure 5.3: Refractive index of Lithium Tantalate between 60 and 100 μm

The high absorbance of the proposed metamaterial structure is attributed to Mie resonance occurring in the particles. Hence a material which has a high value

of refractive index in the terahertz spectrum is needed. LiTaO_3 is one such material, whose refractive index is ~ 10 around $80\mu\text{m}$ (see figure 5.3). Moreover, its extinction coefficient is high as well (~ 3), which acts as an aid to the absorptive properties of the proposed structure. The data for refractive index has been taken from Palik [63], shown as markers in figure 5.3. The proposed structure is basically a two dimensional square array of LiTaO_3 microcylinders grown on a metal substrate which doubles as the ground plane. Despite the existence of complete analytical solutions for a Mie resonant sphere, the cylindrical shape has been chosen for the sake of substrate compatibility. Figure 5.4 shows the design of the proposed metamaterial structure along with its unit cell.

The geometrical parameters of the cylinder viz. the radius r and the height h have been optimized in order to make the structure resonate in the wavelength range $60\text{-}100\mu\text{m}$. The resonant wavelength λ_0 is identified by the position of the peak in the extinction cross-section versus wavelength curve. The dependence of λ_0 on r and h has been studied individually, by varying one at a time while keeping the other a constant. The results of the analysis are shown in figure 5.5. It is seen that resonant wavelength linearly depends on r while it varies non-linearly, w.r.t. the aspect ratio a ($= h/2r$), resembling an error function like behavior. Based on these results, an empirical formula (shown as equation 5.13) has been obtained to express the resonant wavelength as a function of radius and aspect ratio of the cylindrical particles. Hence, the resonant wavelength is given as,

$$\lambda_0 = -7.83\text{erf}(a)r + 16.18r + 56.97\text{erf}(a) \quad (5.13)$$

where λ_0 is the resonant wavelength, a is the aspect ratio, r is the radius and $\text{erf}()$ stands for error function. The blue solid curve in figures 5.5(a)&(b) represents equation 5.13 and markers represent discrete data obtained upon computation. It is clearly visible how well 5.13 fits the computational data in both the curves.

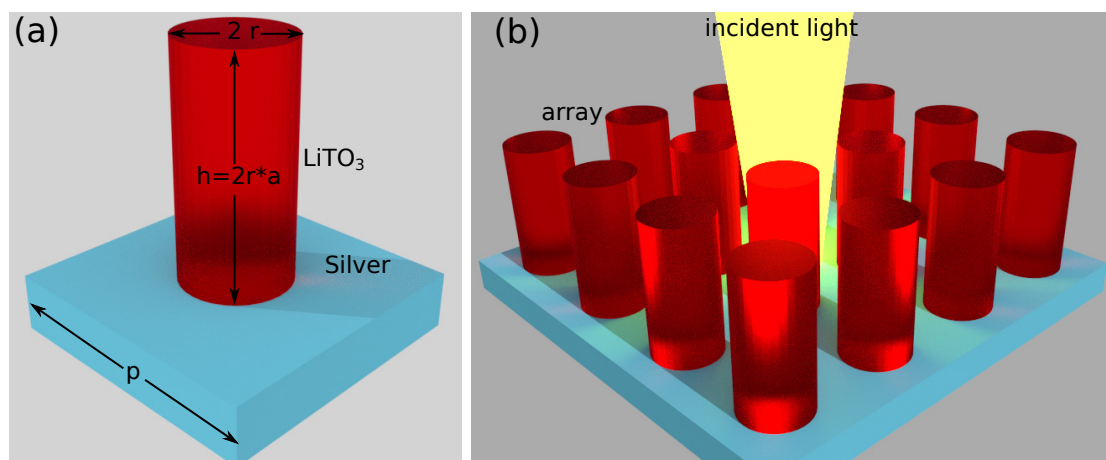


Figure 5.4: (a) Unit cell of the proposed metamaterial structure, (b) array of the LiTaO_3 cylinders over silver substrate.

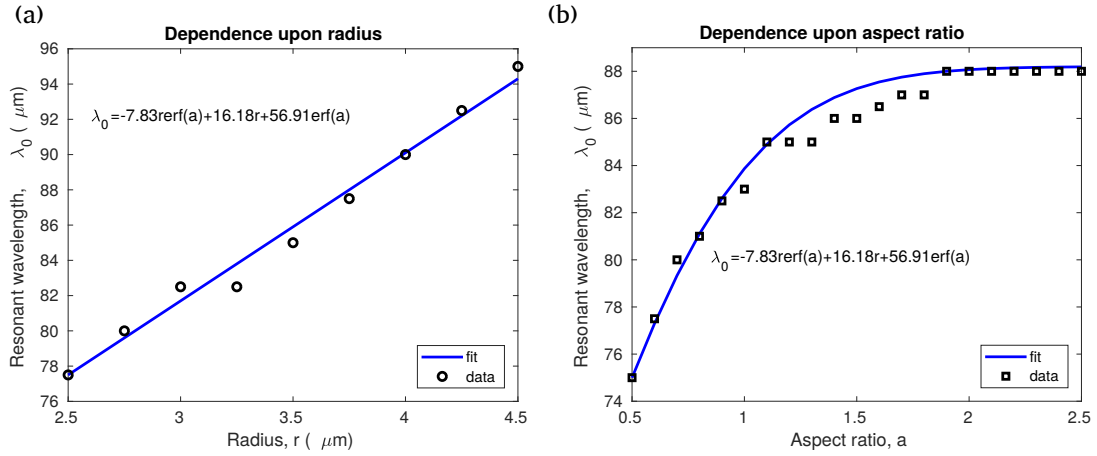


Figure 5.5: Dependence of resonant wavelength on (a) the radius and (b) the aspect ratio. The blue solid curve represents equation 5.13 and markers represent discrete data obtained on computation

It should be noted that the material dispersion has been taken into account during optimization. Hence, though the refractive index is not visible in the above formula, its role is intrinsically included.

Now, to obtain the geometrical parameters which correspond to maximum absorption, the structure has been optimized with respect to radius and aspect ratio independently and the result of optimization are shown in figure 5.6. From figure 5.6(a) & (b) it can be inferred that the absorption is maximum for radius $r = 3.75$ and aspect ratio $a = 1.9$. On substituting these values in equation 5.13,

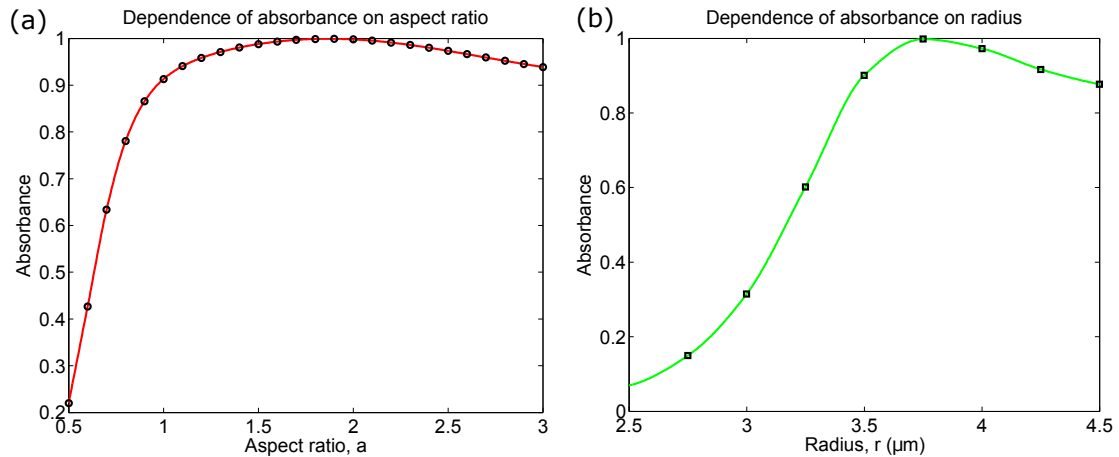


Figure 5.6: (a) absorbance vs aspect ratio curve (b) absorbance vs radius of the cylinder. These graphs show that absorbance is maximum for $a = 1.9$ and $r = 3.75 \mu\text{m}$

the corresponding resonant wavelength which is also the wavelength of maximum

absorption, comes out to be $88 \mu\text{m}$. This is further confirmed by figure 5.7 which shows absorption, scattering and extinction cross-sections for a cylindrical particle of radius $r = 3.75$ and aspect ratio $a = 1.9 \mu\text{m}$ calculated at different wavelengths with a peak at $88 \mu\text{m}$. It is clearly visible that absorption dominates scattering

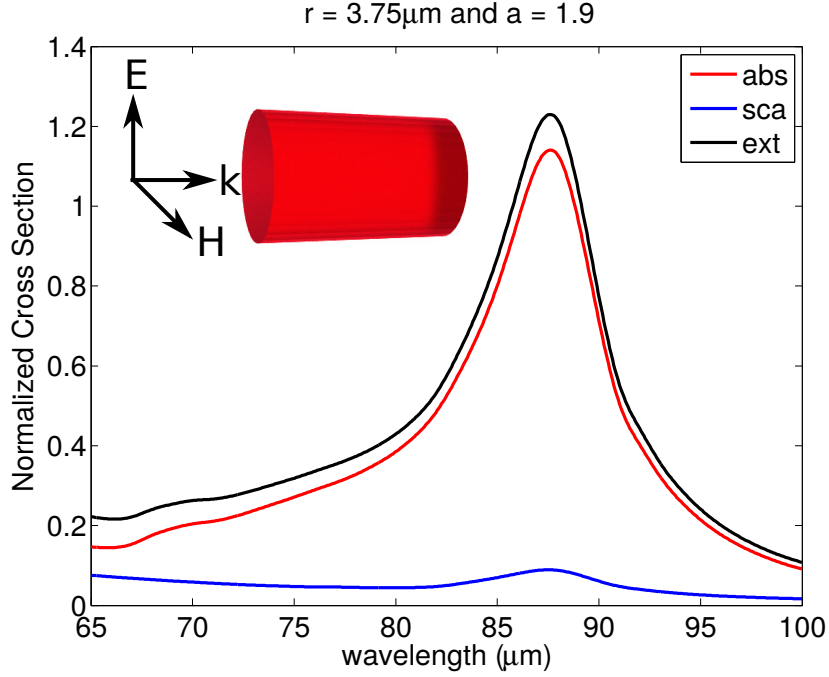


Figure 5.7: Absorption, scattering and extinction cross-section at different wavelengths with maxima at $88 \mu\text{m}$. Inset: orientation of electric and magnetic fields with respect to the particle during calculation of the extinction cross section.

owing to the high value of extinction coefficient of lithium tantalate.

Role of the metallic substrate: In the theory of perfect absorption discussed above, it was established that in the case of two-layer absorber, the second layer has to be a perfect electric conductor (PEC) so as to obliterate the possibility of transmission. Hence the bottom-most layer is always a metallic ground plane. In the proposed design silver has been used to form the ground layer, however, other high conductivity materials like gold and copper can also be used. The thickness of the ground layers is decided by the penetration depth of the em wave into the metal. To ensure negligible transmission, the thickness should be very large compared to the wavelength of the illuminating electromagnetic wave. In electrical engineering, it is a rule of thumb that if one thing has to be very large that another, it should be at least 10 times larger than it. The penetration depth δ of the electromagnetic wave can be known by the formula,

$$\delta = \sqrt{\frac{2}{\omega\mu\sigma}} \quad (5.14)$$

where, ω is the frequency of the electromagnetic wave, μ is the permeability of the metal and σ is the conductivity of the metal. For $\omega = 2.14 \times 10^{13}$ rad/s (*i.e.* $\lambda = 88 \mu\text{m}$), $\mu = 4\pi \times 10^{-7}$ & $\sigma = 6.3 \times 10^7$ S/m, penetration depth $\delta \approx 35$ nm. It should be noted that 5.14 is most suitable for low frequencies (microwaves and radio waves) and tends to give inaccurate results in high frequencies, although, it is useful here because only a vague idea of penetration depth is needed. Based on the above result it is inferred that the thickness of the silver layer should be greater than 350 nm. Hence, for the sake of absolute surety about zero transmission, the thickness has been chosen to 500 nm. The computation of the reflection, transmission and absorption coefficient with and without including silver layers show the significance of the substrate. Figure 5.8(a) shows the reflectance R , transmittance T and absorbance A of an array of LiTaO_3 microcylinders at different wavelengths in the absence of the silver substrate. It can be noticed that while the absorption of light is not more than 50%, the transmission is substantial. The small absorption peak indicates that LiTaO_3 is itself capable of absorbing some amount of incident radiation. Reflection is, however, small due to the negligible scattering of light (blue curve in figure 5.7). In the other situation, where the metallic ground is present, transmission delightfully drops to zero level and absorption peaks to 100% at $88 \mu\text{m}$. With transmission being practically zero for all wavelength, the reflection coefficient (originally given as $R = 1 - T - A$) is now simply calculated as $R = 1 - A$. Hence, as the absorption becomes maximum (100%) at $88 \mu\text{m}$, the reflection becomes minimum.

Now, it is important to mention here, that the 100% absorption observed above is for normal incidence only, and it is necessary to study the impact of oblique incidence as well, without which, the analysis remains incomplete. Hence, the light

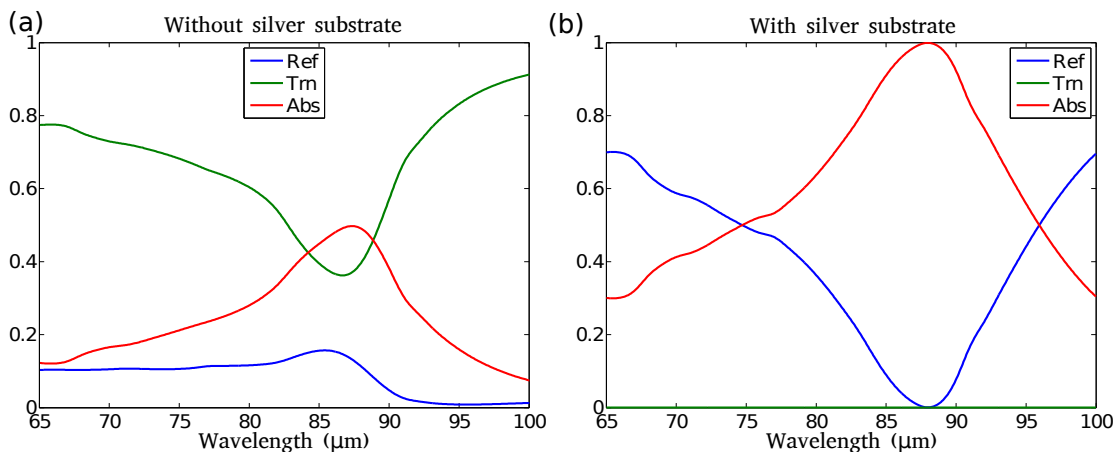


Figure 5.8: (Reflectance, transmittance and absorbance of an array of LiTaO_3 cylinders (a) with and (b) without including metal (silver) substrate. A small absorption peak shows that LiTaO_3 itself absorbs some amount of light in the absence of silver substrate.

was made to fall at different angles varying from -90° to 90° and the corresponding absorption coefficients were calculated. The results have been shown in figure 5.9.

It conveys that absorbance remains above 90% up to 55° . Hence it can be stated

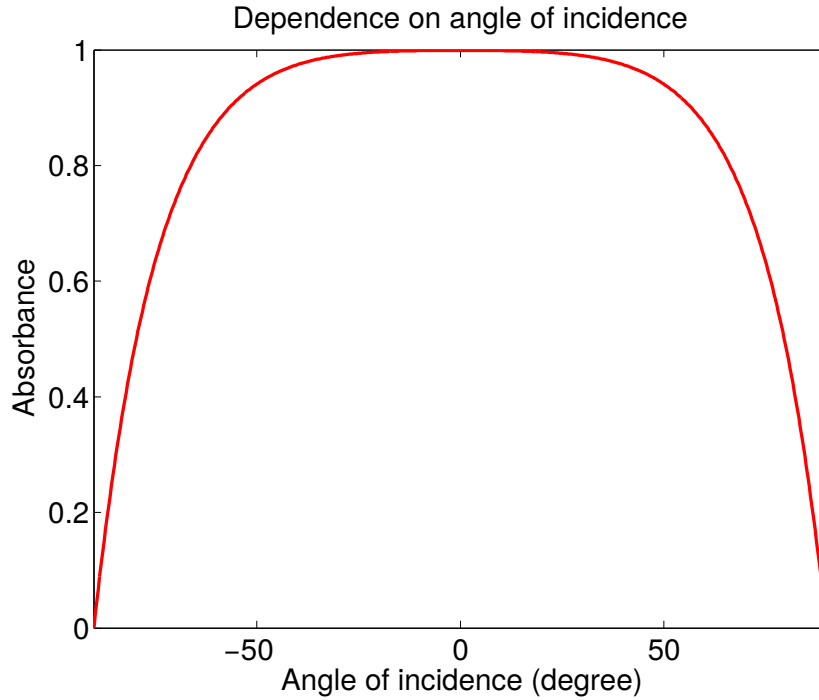


Figure 5.9: Variation of absorbance with respect to angle of incidence. Absorbance remains greater than 0.9 up to 55°

with certainty that the proposed structure is a *broad angle absorber*.

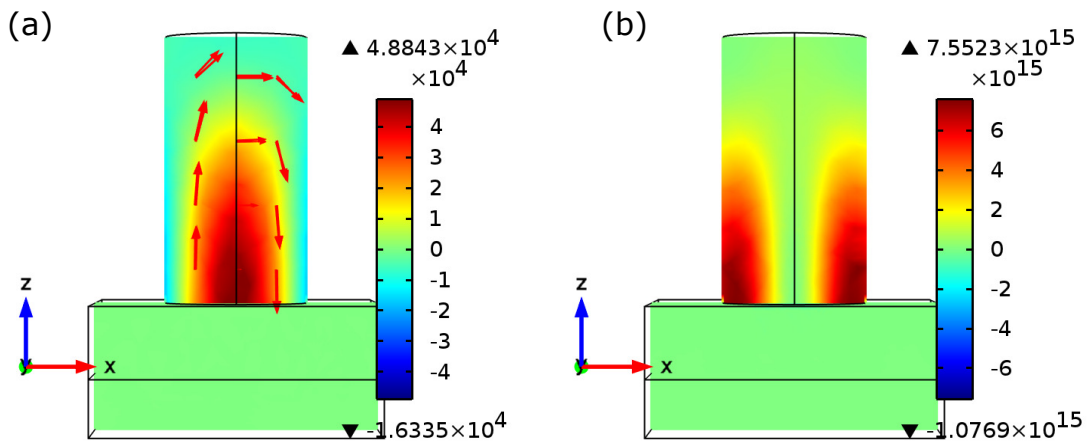


Figure 5.10: (a) Distribution of the y component of the magnetic field (color contours) and rotating electric field (arrows) in the xz plane. (b) Distribution of power loss density at $88 \mu\text{m}$

Finally, the field and power distribution inside the metamaterial unit cell at resonance have been illustrated in figure 5.10. Figure 5.10(a) shows the distribution of y-component magnetic field and the arrows show rotating electric field vector which confirms the magnetic resonance occurring at 88 m m. Figure 5.10(b) shows power loss density inside the cylinder.

5.4 Comparison with a metallic patch type metamaterial perfect absorber

In light of all the above discussion, the excellent absorption capabilities of the proposed metamaterial perfect absorber have been well established. However, for an extra piece of information, it shall be delightful to compare this MMPA with a contemporary design, in terms of bandwidth. For this purpose, the design reported by Hao et al. [33] has been selected, which is a high-performance metamaterial absorber. Its should be noted that though the design was reported to operate in near-infrared spectrum, it has been appropriately scaled up here, in order to shift the resonance to 88 μm for fair comparison with the LiTaO₃ absorber. The unit cell of metamaterial inspired from Hao's work is shown in the figure along with necessary geometrical details. Upon computing the absorption spectrum of

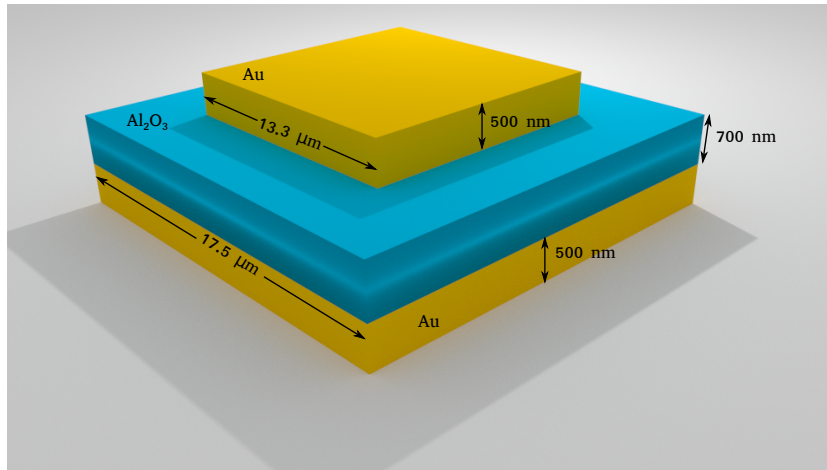


Figure 5.11: A unit cell of metallic patch type metamaterial perfect absorber resonant at 88 μm , inspired from Hao et al. (2010) [33]

the structure shown in figure 5.11 and plotting it along with that of the proposed LiTaO₃ absorber, figure 5.12 was obtained. Even a glance at the figure 5.12 shows that as far as bandwidth is concerned, LiTaO₃ based metamaterial is a clear winner. Hence it can be stated with certainty that the proposed structure is a *broadband absorber*.

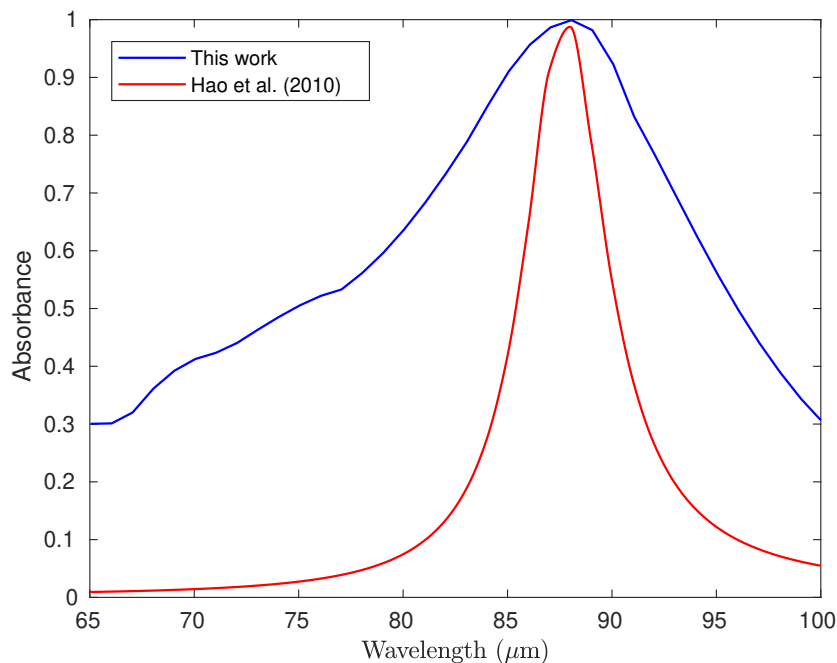


Figure 5.12: Comparison of the proposed the LiTaO₃ absorber with the work of Hao et al. [33]

5.5 Conclusion

From the above analysis, it can be concluded that the proposed metamaterial exhibits perfect absorbance ($A > 99.0\%$) at $88 \mu\text{m}$. The reason behind this extraordinarily high value of absorbance is the fact that, the high value of the extinction coefficient of LiTaO₃ dissipates the field localized inside the cylindrical particle due to Mie resonance. Silver substrate present below the cylinders blocks transmission and as well as reinforces the process of absorption by the virtue of the huge ohmic loss associated with the metal. Hence, perfect absorbance is observed. Furthermore, it has been shown that the proposed metamaterial has absorbance > 0.9 for the angle of incidence up to 55° and beats a contemporary, popular & high-performance MMPA design, which is sufficient to earn for it the title of a broad-angle broadband metamaterial perfect absorber.

Chapter 6

An all-dielectric zero-index metamaterial based nanoantenna

6.1 Introduction

The ability of the metamaterials to show abnormal refractive index has been well exploited in the previous chapters, where both - the positive index metamaterial (chapter 3 and 5) and negative index metamaterial (chapter 4) have been designed, analyzed and put to useful applications. On the similar lines, a metamaterial can also be made to exhibit effectively zero refractive index. A large number of metal-dielectric composites have been proposed in the past [56], which achieve zero refractive index by reducing either the permittivity or permeability or both to zero. An appropriate nomenclature is thus used for their classification as, epsilon-near-zero (ENZ), mu-near-zero (MNZ) and epsilon-and-mu-near-zero (EMNZ) depending upon whether permittivity (ϵ) or permeability (μ) or both are zero [53]. The EMNZ metamaterial can be alternatively called zero-index metamaterials (ZIM). They show a very interesting property of wavefront engineering, which have been extensively utilized in the recent past, for gain and directivity enhancement of antennas [109, 111, 97, 57, 17, 91, 110, 76, 96]. It is understandable that a wave does not undergo any change in phase upon passing through a ZIM. Hence phase matching capability is intrinsic to them. Thus ZIM can also be employed in realization of nonlinear phenomenon like second and third harmonic generation [58, 16, 15], four-wave mixing [90, 11], etc where phase matching is a necessary condition. However, there is an intrinsic and inevitable demerit attached to the metallic inclusions based metamaterials called the ohmic loss. The power dissipation in metallic inclusion at high frequency (visible and near infrared), is substantial and renders such structures unsuitable for high frequency applications. As a result, the all-dielectric route is being adopted for the evolution of ZIM to the next level.

In 2011, Huang et al. proposed a brilliant design of an all-dielectric ZIM [37], which comprised a square lattice of dielectric columns. The rods were made up of

silicon and surrounding medium was air. The authors successfully demonstrated the zero refractive index behavior and interesting phenomena like electromagnetic cloaking and wavefront engineering as its manifestations. Huang et al. argued that the existence of Dirac cones in the photonic band structure of the metamaterial was the underlying principle for the zero-index behavior [64, 100, 82, 1, 34, 75]. The term Dirac cone has been borrow from graphene where a similar feature is observed in the electronic band structure [27, 44]. Though the ZIM proposed by them was brilliant, it was difficult to erect long upright columns on a substrate. Moitra et al., in 2013, came up with a modification, in which horizontal columns instead of vertical, were laid down on a substrate with silica as the spacer between them and PMMA (poly(methyl methacrylate)) as the surrounding medium [62]. Though their ZIM was easy to fabricate, it still lacked compatibility to on-chip operation. This incompatibility was totally removed when in 2015, when Li et al. suggested about confining the dielectric columns between parallel conductors, due to which the dielectric cylinders of finite high behaved like infinitely long columns and TM mode was enforced on them [52, 47]. It is Li's metamaterial on which the nanoantenna reported in this chapter is based. The directional transmission using ZIM has been studies for a long time. Temelkuran et al., in 2000, reported a highly directive photonic crystal based resonant antenna [95]. They used a combination of a monopole source and a layer-by-layer photonic crystal. Enoch et al., in 2002, reported an entirely different structure which had a monopole antenna embedded inside a metamaterial [24]. Metamaterial was made up of multiple layers of copper grids separated from each other by foam. The monopole operated near the plasma frequency of the metamaterial and ENZ behaviour resulted in directivity enhancement. This was followed by several other works which employed ENZ or ZIM structures to enhance directivity and gain of different types of gigahertz antennas [40, 96, 76, 110, 91, 57, 97, 111, 109]. All these structures were basically made up of metallic resonators and hence had intrinsic ohmic losses. For nanoscale application, all-dielectric ZIMs are more suitable option, as they are free from ohmic losses. Dielectric ZIMs are basically photonic crystals having Dirac like dispersion at Γ point [27, 82, 100, 37]. Besides effectively zero refractive index, Dirac dispersion has many other interesting applications as well [64, 44].

The aim of this chapter is to propose a ZIM based all-dielectric nanoantenna to directionally radiate emissions from an isotropic nanoscale emitter. Though the directional radiation using ZIM has been reported in the past, non of them has design compatible to on-chip fabrication techniques. In the following sections, the fundamental principle of zero refractive index, the conditions of zero index behaviour, critical role of the design parameters, effect of materials and the surrounding media, etc, have been presented in rigorous detail. The ZIM used here is the one proposed by Huang (2011) and improved by Li (2015). As the chapter unfolds, the reader comes to realize that the zero index property is absolutely natural and in terms with the laws of physics.

6.2 The fundamental concept of zero refractive index

6.2.1 Zero index metamaterial systems

Basically, any medium whose effective refractive index exhibits transition from negative values to positive values, is bound to exhibit effective index at the frequency of transition i.e. the frequency at which the refractive index curve cuts the x-axis. This type of dispersive property is abnormal for natural materials but can be easily achieved by metamaterials. For example, let us consider a well acknowledged fishnet type negative index metamaterial. Its typical unitcell and effective refractive index ($n + ik$) are shown in figure 6.1. It can be seen that as

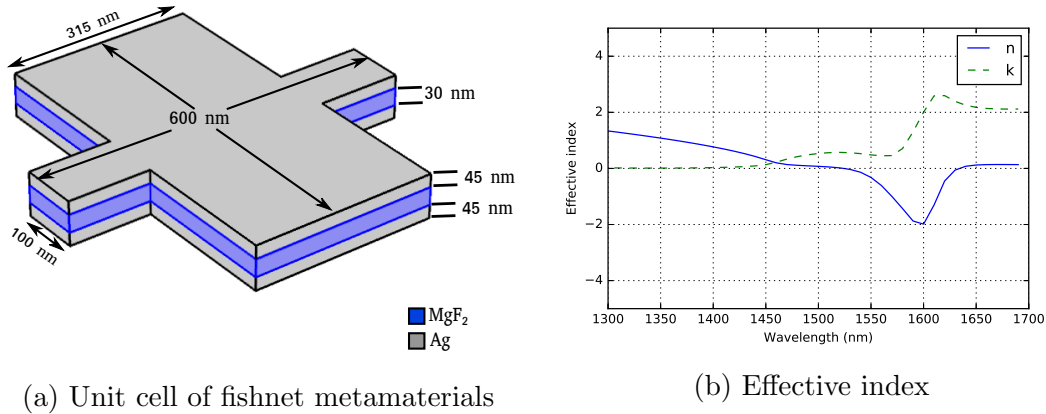


Figure 6.1: Fishnet metamaterial

the wavelength is increased, the refractive index transits from positive to negative values, continues to remain negative for a range of wavelengths and returns to the positive domain. And the two points of transition, corresponding to 1530 nm and 1630 nm, are the points of zero refractive index behavior. Investigation of optical properties at these two wavelengths can pave way for several interesting applications. However, a major drawback is that the fishnet metamaterial has huge ohmic loss attached to it, hence is a poor choice as a zero index metamaterial.

In their seminal paper, Wang et al. [100] suggested that an optical system that sustains double Dirac cones i.e. exhibits Dirac-like linear dispersion (see figure 6.2(a)), is ideal for realization of zero refractive index. They formulated the dispersion relation for a double Dirac system in the vicinity of the Dirac point, which can be derived as follows. Let us write the wave vector k as a function of angular frequency ω in Taylor series form about the Dirac point as,

$$k(\omega) = k(\omega_D) + \frac{k'(\omega_D)}{1!}(\omega - \omega_D) + \frac{k''(\omega_D)}{2!}(\omega - \omega_D)^2 + \dots \quad (6.1)$$

where ω_D is the frequency corresponding to Dirac point. If $k(\omega_D) = 0$ and the dispersion curve is almost linear in the vicinity of the Dirac point (as shown in figure 6.3), higher order terms can be neglected and equation 6.1 reduces to

$$k(\omega) = \frac{\omega - \omega_D}{v_D} \quad (6.2)$$

where $v_D = (d\omega/dk)|_{\omega=\omega_D} = 1/k'(\omega_D)$ is the group velocity at Dirac point. It is clearly visible in equation 6.2 that with respect to frequency, the value of $k(\omega)$ varies from negative, through zero, to positive. The refractive index follows the same trend with zero value at ω_D (see figure 6.2(b)). Wang et al. labeled such media as *negative zero positive index* (NZPI) media and advocated the candidature of low loss metamaterial for the purpose.

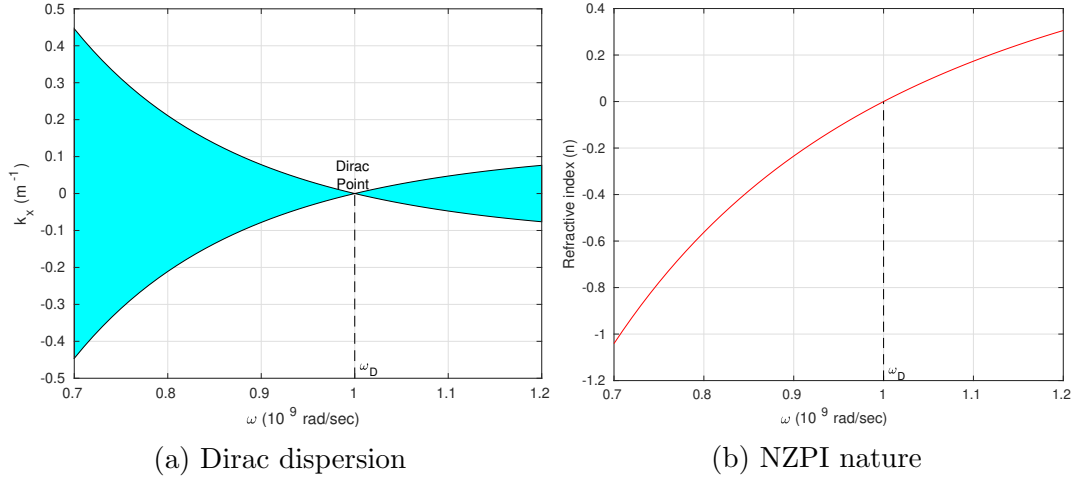


Figure 6.2: A Dirac like dispersion in a negative zero positive index metamaterial

Now, in order to identify the characteristic which imparts linear dispersion and zero index nature, let us assume a metamaterial which exhibits both - electric and magnetic activities and whose effective permittivity (ϵ_{eff}) and permeability, on the basis of Drude's model, are given by

$$\epsilon_{eff}(\omega) = 1 - \frac{\omega_{ep}^2}{\omega^2 + i\omega\gamma} \quad (6.3)$$

$$\mu_{eff}(\omega) = 1 - \frac{\omega_{mp}^2}{\omega^2 + i\omega\gamma} \quad (6.4)$$

where, ω_{ep} and ω_{mp} are the electric and magnetic plasma frequencies, and γ ($\ll \omega_{ep}, \omega_{mp}$) is the loss factor. According to the above equations, when $\omega \rightarrow \omega_{ep}$, $\epsilon_{eff}(\omega) \rightarrow 0$ and when $\omega \rightarrow \omega_{mp}$, $\mu_{eff}(\omega) \rightarrow 0$. Now, if somehow, the magnetic plasma frequency happens to be equal to electric plasma frequency, i.e. $\omega_{mp} = \omega_{ep} = \omega_D$ and $\gamma = 0$; then, for $\omega = \omega_D$ ϵ_{eff} & μ_{eff} simultaneously become

zero. As a result, at the Dirac point frequency $\omega = \omega_D$ effective refractive index $n_{eff} = \sqrt{\epsilon_{eff}}\sqrt{\mu_{eff}}$ also becomes zero. The figure 6.2 depicts this type of system, where, $\omega_{mp} = \omega_{ep} = 1 \times 10^9$ rad/sec and $\gamma = 10^{-5}\omega_{ep}$. Figure 6.2(a) shows dispersion diagram in which the Dirac cones and the Dirac point can be clearly observed and figure 6.2(b) depicts the resultant nature of effective refractive index which is zero at the ω_D . In this way, the basic characteristic of a zero index system have been profoundly understood.

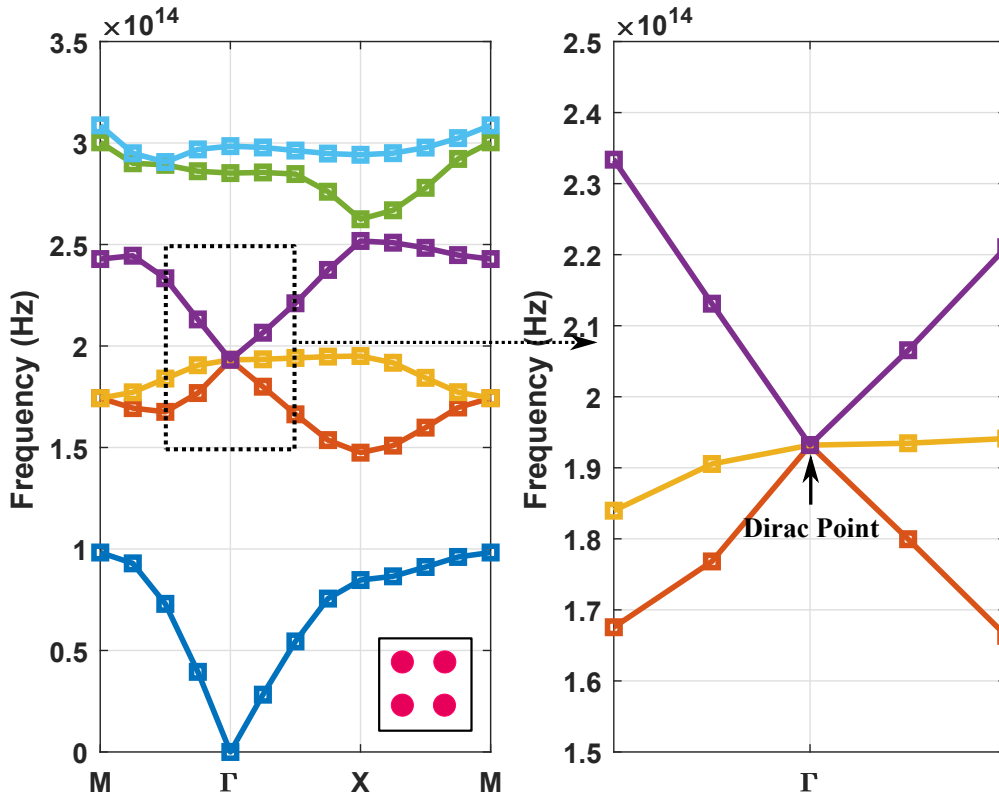


Figure 6.3: Photonic band structure of the ZIM. The inset shows the square shape of the array. The region around the Dirac point has been zoomed to show the linear dispersion in its neighborhood.

Wang et al. presented a beautiful model for ZIM systems, but real design was proposed by Huang et al. [37] in 2011. Huang reported that a square array of dielectric columns of a suitably chosen radius and periodicity can perform as zero index metamaterial as it sustains Dirac cones and linear dispersion near the Dirac point. Moreover, since it involved no metallic components, the design was practically free from resistive losses. Figure 6.3 shows the band diagram of a square lattice of silicon rods having r/a ratio equal to 0.2. The band structure clearly depicts a Dirac point at the center of the Brillouin zone. The conical shape of the dispersion surface becomes more evident in the three dimensional version of the band structure shown in figure 6.4. Huang's design is robust and works

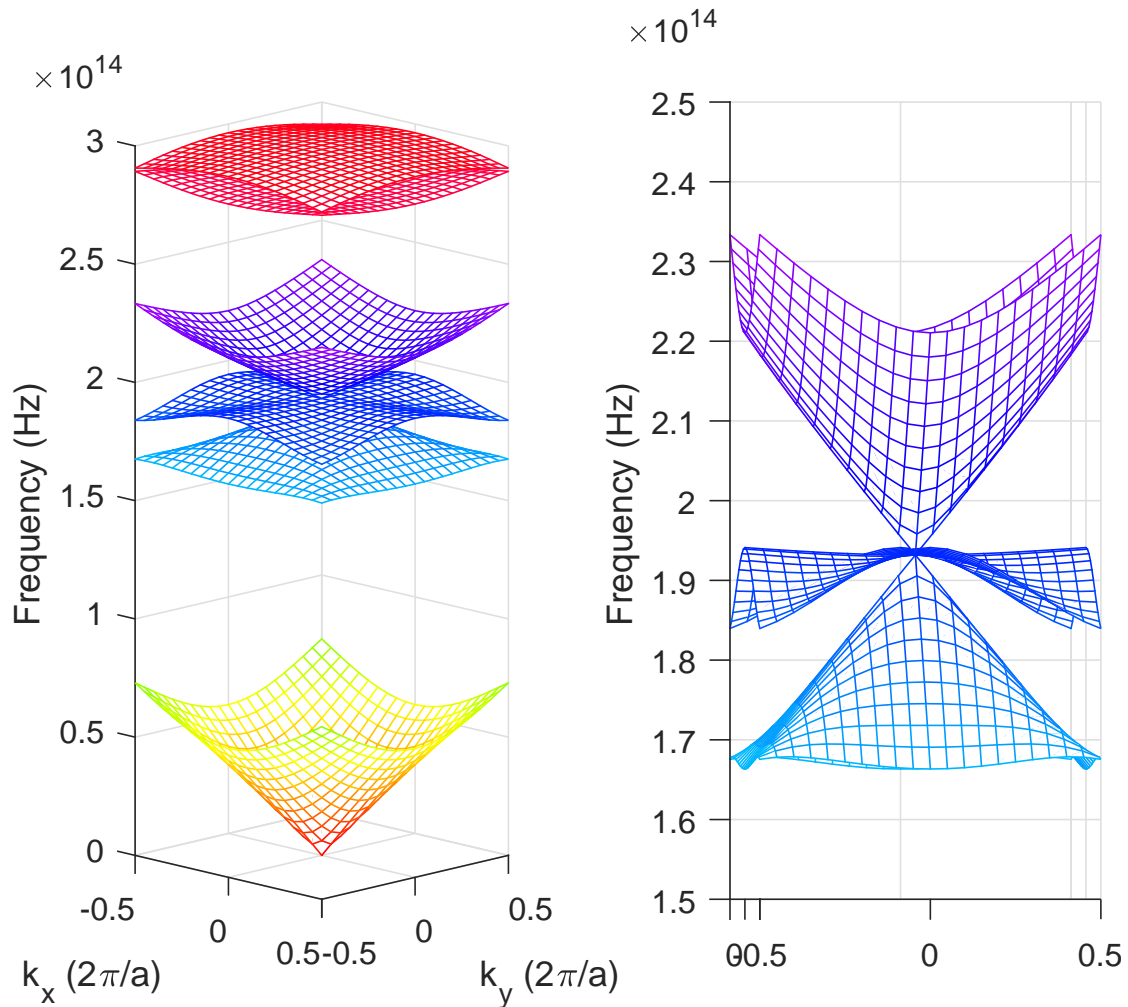


Figure 6.4: 3D dispersion surfaces displaying the formation of Dirac cones

so efficiently well, that since then, its has been investigated, improvised and and utilized in many research works. And for the same reasons, it has been used in the ZIM based nanoantenna, to which this chapter is dedicated.

6.2.2 Rectangular waveguide: A zero index system other than metamaterials

Though above mentioned works proposed the metamaterial route to achieve zero refractive index, the rectangular waveguides have always been showing this property much prior the perception of metamaterials. It is just that nobody pays much attention to it, because, a waveguide is always operated above the cut-off frequency. For better understanding, let us assume a rectangular waveguide like the one shown in figure 6.5(a).

For TE_{mn} mode, where m index corresponds to the larger dimension a and n

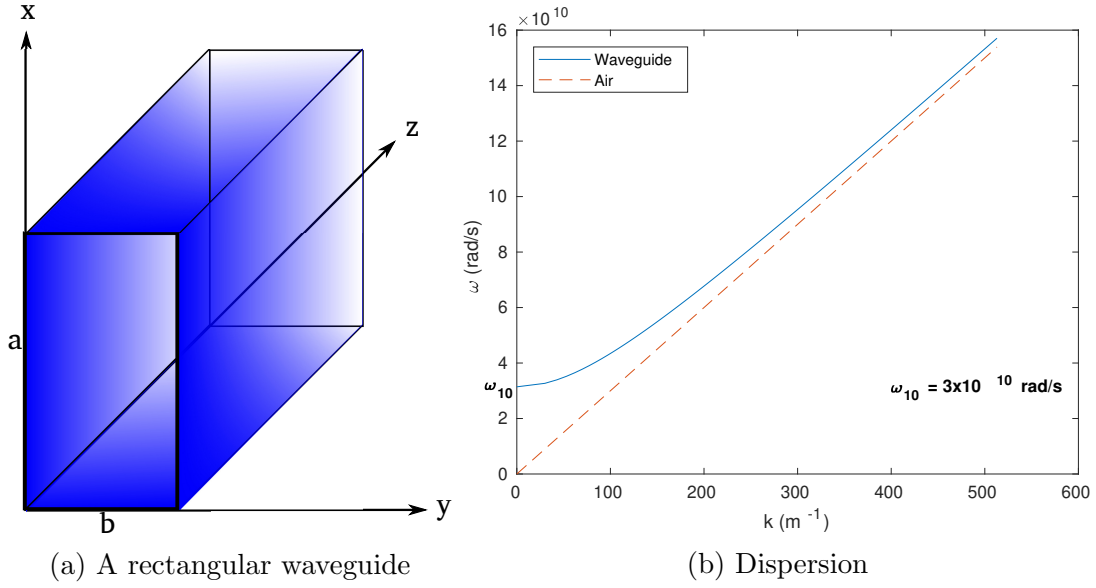


Figure 6.5: Dispersion analysis of a rectangular waveguide indicates zero phase at the cut-off frequency ω_{10}

to the smaller dimension b , the wave number k is given by [30]

$$k = \sqrt{\left(\frac{\omega}{c}\right)^2 - \pi^2 \left[\left(\frac{m}{a}\right)^2 + \left(\frac{n}{b}\right)^2 \right]} \quad (6.5)$$

$$k = \frac{1}{c} \sqrt{\omega^2 - \omega_{mn}^2} \quad (6.6)$$

where,

$$\omega_{mn} = \pi c \sqrt{\left[\left(\frac{m}{a}\right)^2 + \left(\frac{n}{b}\right)^2 \right]} \quad (6.7)$$

is the cutoff-off frequency. The wave velocity or phase velocity is given as,

$$v_p = \frac{\omega}{k} = \frac{c}{\sqrt{1 - (\omega_{mn}/\omega)^2}} \quad (6.8)$$

and the group velocity is given by

$$v_g = \frac{1}{dk/d\omega} = c \sqrt{1 - (\omega_{mn}/\omega)^2} \quad (6.9)$$

Below cut-off frequency ($\omega < \omega_{mn}$), no mode exists as k is imaginary and for very high frequencies ($\omega \gg \omega_{mn}$), propagation becomes similar to that in free space. At very high frequencies, wavelength λ_{mn} is very small compared to the dimensions a & b , so much so that, the incoming wave feels as if its traveling in free space. The

lowest cutoff frequency is ω_{10} , corresponding to TE_{10} mode. Figure 6.5(b) shows the dispersion curve for TE_{10} mode, along with the dispersion of free space (or air). It is visible that as frequency increases the dispersion approaches free space behavior. The curve has been plotted for a waveguide of dimension $a = 3$ cm and $b = 2$ cm, whose lowest cutoff frequency $\omega_{10} = 3 \times 10^{10}$ rad/sec. Below ω_{10} no mode exists, all the higher modes appear at cut-off higher than ω_{10} .

For any mode, At $\omega = \omega_{mn}$ wave vector k is zero, hence, the effective refractive index is zero and the phase velocity is infinite, which, it is free to be. It should be noted that no laws of physics are violated if phase velocity becomes greater than c , or even infinite, as it has no physical significance. The group velocity is the actual rate of transfer of energy, which is always less than c , according to equation 6.9. Hence, it has been understood that zero refractive index is a very natural property of a certain physical systems.

6.3 Design of zero index metamaterial

The ZIM used in this work is the same as the one proposed by Huang et al., a photonic crystal (PhC) made up of Silicon ($\epsilon = 12.5$) rods in air. Figure 6.3 shows the photonic band structure of ZIM in which the location of Dirac point and the linear nature of dispersion is displayed. Linear dispersion manifests itself in the conically shaped dispersion surfaces, referred to as Dirac cones, touching each other at the Dirac point (see figure 6.4). The desired frequency corresponding to Dirac point has been chosen to be 193 THz which translates to 1550 nm wavelength. The periodicity ($a = 840$ nm) of the array and radius ($r = 0.2a$) of each rod have been suitably chosen to achieve Dirac point at 1550 nm.

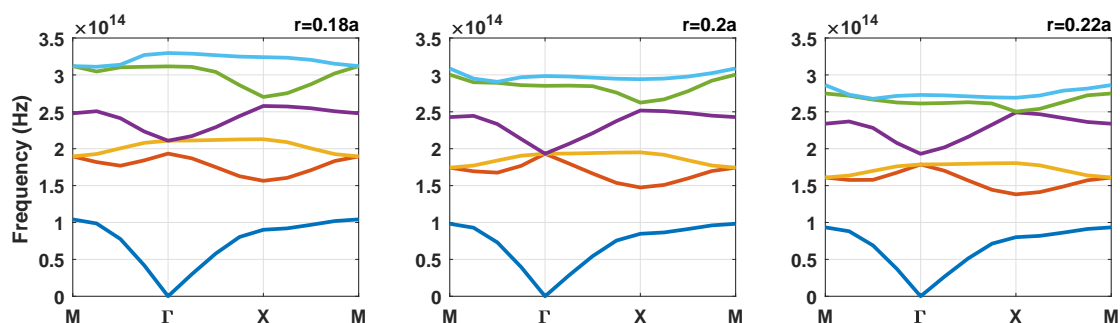


Figure 6.6: Illustration of how critical the r/a ratio is for Dirac like dispersion

This condition is not easy to achieve because wave vector is generally a quadratic function of frequency at the center of Brillouin zone. However, a PhC having a particularly chosen r/a ratio (0.2 in this case, but may differ for a different dielectric) can fulfill the condition of linear dispersion. For any other value, the condition fails and Dirac cones are lost. This has been demonstrated in figure 6.6. It can be observed that even a slight deviation from the appropriate value of r/a ,

substantially disturbs the Dirac cone. It should be noted that the structure can be tuned to different wavelength if one varies the periodicity and radius without disturbing the r/a ratio.

6.3.1 Calculation of effective material parameters

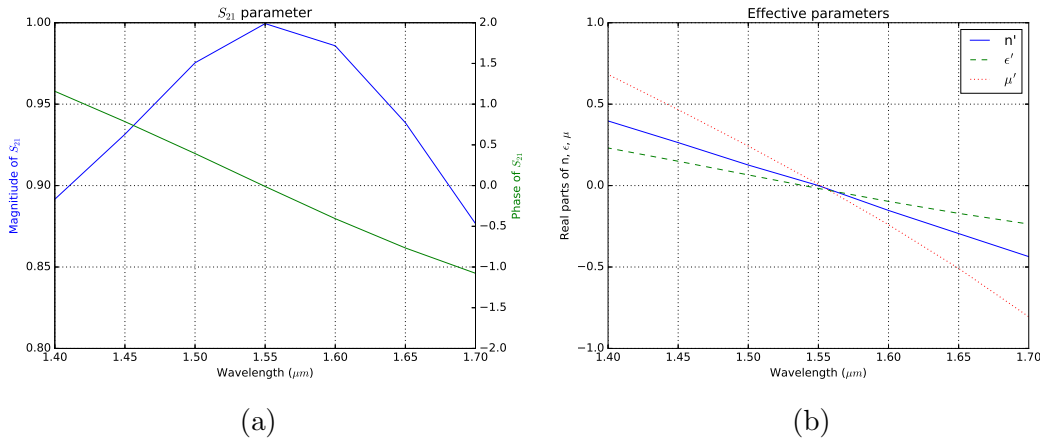


Figure 6.7: (a) Magnitude and phase of scattering parameter S_{21} . (b) Effective material parameters retrieved by s-parameter inversion

To confirm the zero index character, an s-parameter inversion based parameter retrieval technique has been implemented to calculate the effective permittivity, effective permeability and effective refractive index [89]. The calculated material parameters have been plotted with respect to wavelength and are shown in figure 6.7. Figure 6.7(a) shows that, the phase of the S_{21} parameter is zero at $1.55 \mu\text{m}$ and in figure 6.7(b) it is shown that, the refractive index curve passes through zero at $1.55 \mu\text{m}$. It should be noted that, as the wave vector and effective index tend to zero inside a ZIM, the effective wavelength tends to infinity. Hence effective medium theory still holds good and the above-mentioned parameter retrieval technique is absolutely applicable.

6.4 Principle of directional radiation by ZIM

Inside a ZIM, a wave experiences zero change in phase, i.e. all the points on the boundary and in the bulk of a ZIM vibrate in the same phase. This property can be exploited to generate highly directive radiation [1, 53]. If an infinitely long ZIM slab is provided with a current line source embedded inside, highly directive beams can be obtained, as illustrated in figure 6.8. In figure 6.8(a), cross-section of ZIM with an embedded current line source (acting as a point source in 2D) is shown. It can be observed in figure 6.8(c) that, a substantially larger amount of

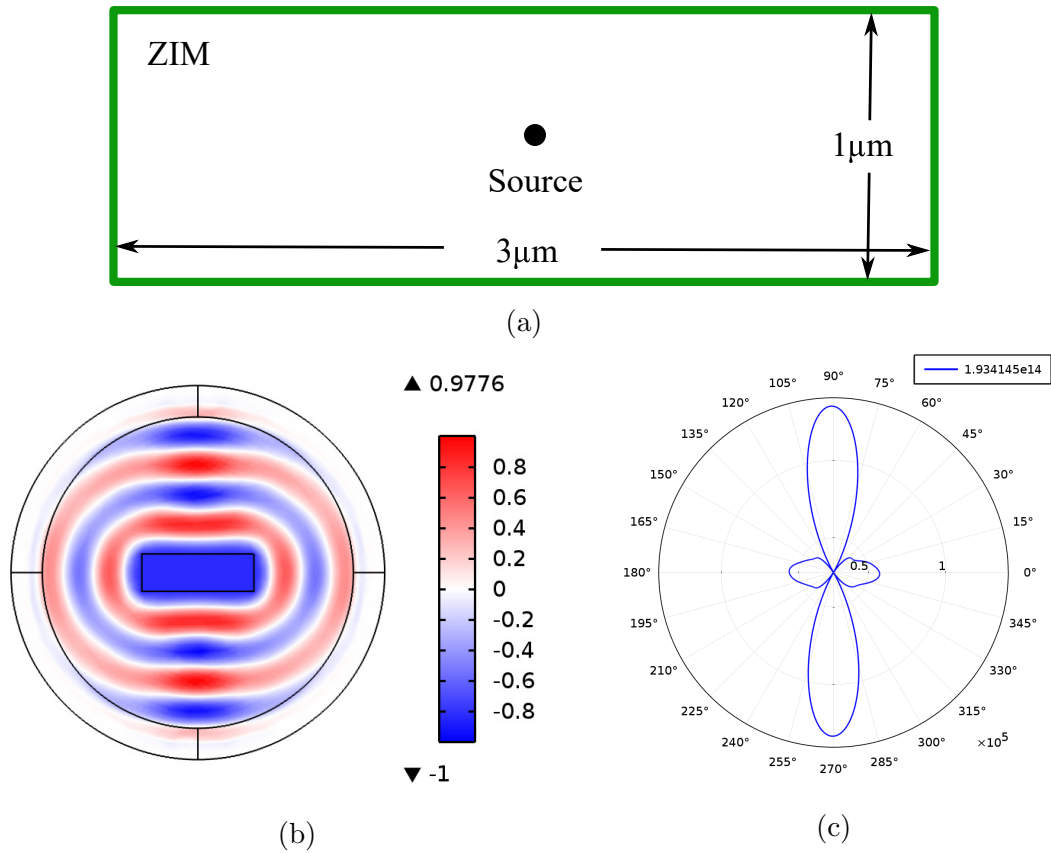


Figure 6.8: Demonstration of the capability of a homogeneous ZIM slab to generate highly directional beams of light. (a) Geometry of the slab with an embedded current line source, (b) Electric field distribution around it, and (c) farfield plot to display the amount power flow w.r.t. the azimuthal coordinate at 193.4 THz (1550 nm).

radiation emerges out of the longer edge of the ZIM slab compared to the shorter one. It is attributed to the fact that every point in ZIM which vibrates in phase with the embedded point source, acts as a source itself. Hence it seems logical that the longer boundary of the slab, which has a greater number of points, gives out a larger amount of radiation compared to the shorter boundary. In this way, the ZIM slab plays the role of a highly directive antenna for an omnidirectional source.

6.5 Design and operation of ZIM nanoantenna

Based on the above principle one can think of ZIM based directive nanoantenna which comprises a 2D array of silicon rods in air operating in TM mode (as discussed in section 2). While calculating the band structure, the rods are assumed

to be infinite in length which seems impractical. Upon fabrication on a substrate, rods will obviously have a finite height hence their behaviour is bound to deviate from the ideal case. However, Li et al. successfully developed an on-chip compatible ZIM in which silicon rods of finite height were made to behave like infinite ones by purposely enclosing them between parallel sheets of a conductor (gold) [52]. In this way the electric field remains along the axis of the rods and TM mode is enforced. Such an arrangement can be used to directionally radiate light generated by nanoscale emitters like quantum dots. Figure 6.9(a) shows the design of the proposed nanoantenna with quantum emitter embedded in it. The nanoantenna contains ZIM to provide high directivity, and Bragg reflector to reduce backward radiation. The ZIM is made up of a 3×7 periodic array of silicon rods whose periodicity $a = 840$ nm, radius $r = 0.2a$ and height $h = 4r$. The central rod has

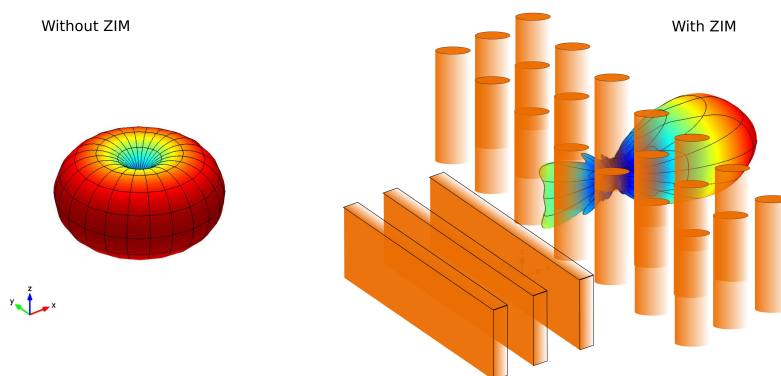
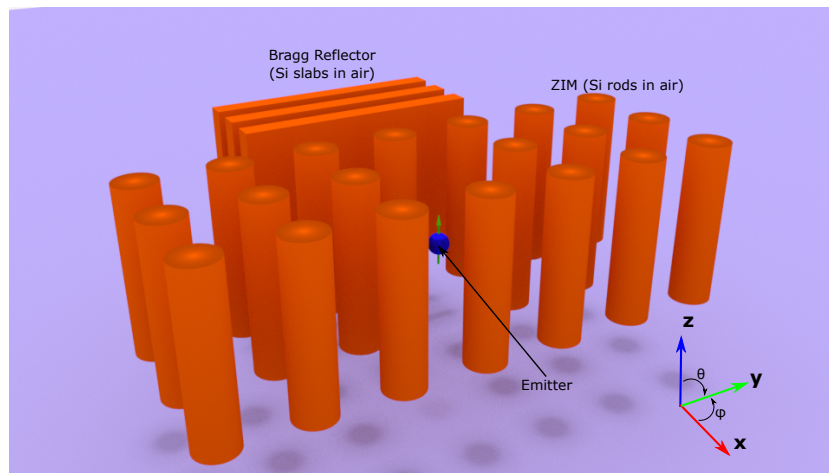


Figure 6.9: (a) Design of ZIM based nanoantenna. (b) radiation pattern of the emitter alone (left), and radiation pattern of the emitter with nanoantenna (right)

been removed and the quantum emitter sits in its place. A point dipole source was used to represent the emitter during computation. The Bragg mirror is made up of periodically placed silicon slabs of quarter-wave thickness. The thickness of each slab is $t_1 = 109$ nm and the air gap between them is $t_2 = 387$ nm. Figure 6.9(b (left)) illustrates the original radiation pattern of the emitter alone in which the power is seen flowing isotropically in H plane. But when the emitter is embedded inside the ZIM, most of the power flows towards the positive x direction, as shown in figure 6.9(b (right)). One can easily notice the large frontal lobe, small back lobe and insignificant side lobes.

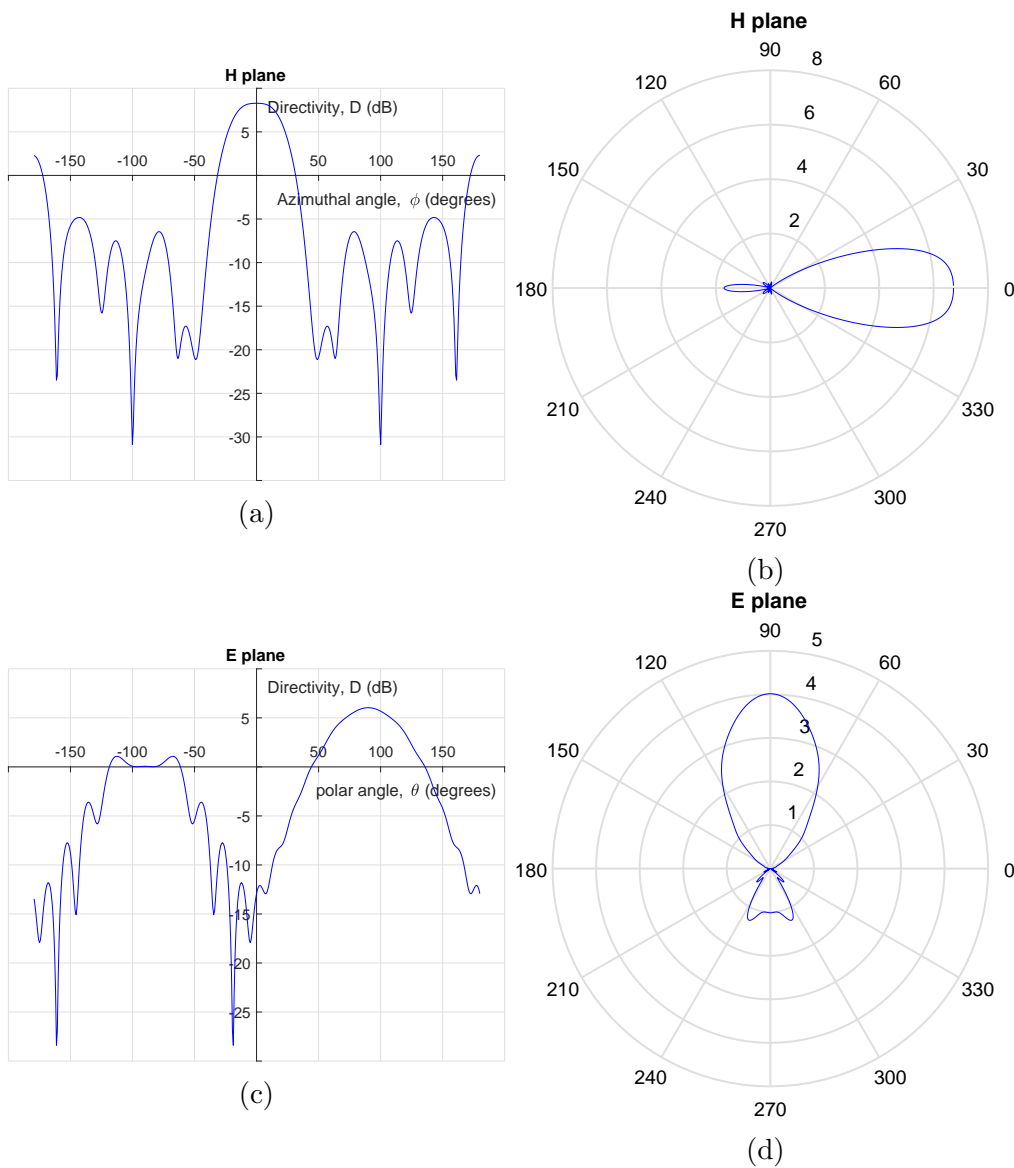


Figure 6.10: Directivity D in H plane - (a) Cartesian plot and (b) Polar plot. Directivity in E plane - (c) Cartesian plot and (d) Polar plot.

From the radiation pattern, other useful parameters such as directivity and beamwidth have also been calculated. The directivity D has been calculated using the formula [48]

$$D(\theta, \phi) = \frac{4\pi p(\theta, \phi)}{P_{rad}} \quad (6.10)$$

where θ and ϕ respectively represent the polar and azimuthal coordinate of a spherical coordinate system, $p(\theta, \phi)$ is the power radiated in a particular direction and P_{rad} is the total power radiated. Plots for directivity D as a function of ϕ in H plane and as a function of θ in E plane respectively are shown in figure 6.9. Maximum directivity in H plane comes out to be 8.28 dB at $\phi = 0^\circ$ and in E plane it is 6.04 dB at $\theta = 90^\circ$. It should be noted that directivity has been expressed in decibels (dB) in figures 6.10(a) & (c) to easily calculate the 3 dB beamwidth. 3 dB beamwidth is 45° in H plane and 63° E plane.

6.6 Effect of the surrounding material

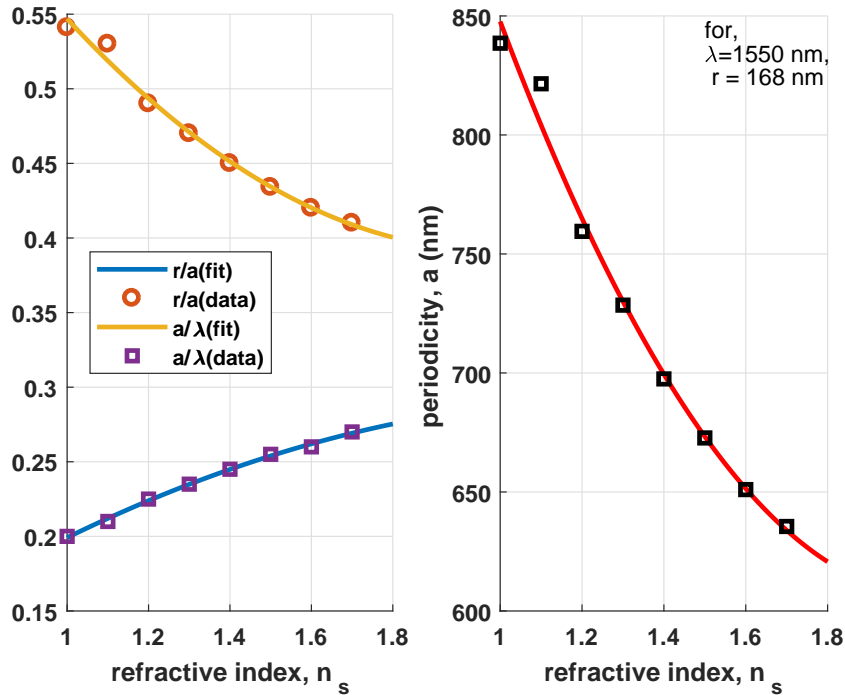


Figure 6.11: (Left) Dependence of required r/a ratio and normalized frequency (a/λ) on the refractive index of the chosen surrounding medium, (Right) Variation of periodicity of the rods with respect to the refractive index of the chosen surrounding medium.

Though air has been taken as the surrounding medium for the sake of simplicity, it is obvious that during on-chip fabrication the rods shall be embedded

in some matrix such as SU-8 [52], poly(methyl methacrylate) (PMMA) [62], etc. Hence it is necessary to study how the design parameters need to be modified according to the choice of the surrounding medium, in order to achieve a proper Dirac Cone. Figure 6.11(a) shows the variation of the required r/a ratio with respect to refractive index, n_s , of the surrounding medium, for the formation of Dirac cone. It also shows the decreasing trend in the normalized frequency (a/λ) corresponding to Dirac point with increase in refractive index. If one intends to keep radius, a constant, the periodicity needs to be decreased with respect to increase in surrounding material's refractive index, as shown in figure 6.11(b), so that the Dirac point and hence zero-index is achieved at 1550.

6.7 Effect of the gap between ZIM and Bragg mirror

It is understandable that since the reflected wave re-enters the ZIM, interference effects are bound to influence that output power. Hence it becomes necessary to study the effect of gap between ZIM and the Bragg mirror, on the output power received. On contemplating figure 6.12, it is noticed that before re-entering the ZIM, wave has undergone path difference of $2g + \lambda/2$. The factor of $\lambda/2$ has been incorporated to include the phase reversal occurred on being reflected by an optically denser medium. Basic understanding of interference phenomenon leads us to the following conditions:

For constructive interference,

$$2g + \lambda/2 = n\lambda \quad (6.11)$$

or

$$g = (2n - 1)\lambda/4 \quad (6.12)$$

For destructive interference,

$$2g + \lambda/2 = (2n + 1)\lambda/2 \quad (6.13)$$

or

$$g = n\lambda/2 \quad (6.14)$$

Constructive interference results in high output power in the farfield zone. Hence the value of gap parameter g should be set accordingly. To determine the most suitable value, the gap parameter was varied from 100 nm to 1500 nm upon which two maxima were observed at 340 nm and 1085 nm. Figure 6.13 shows the variation of electric field intensity in the farfield zone with respect to the variation of the gap parameter. The periodic nature observed is intrinsic property of interference phenomenon. However the values of g corresponding to local maxima in intensity profile are not exactly equal to those predicted by equation 6.12 on assuming $n = 1$ and $n = 2$ respectively.

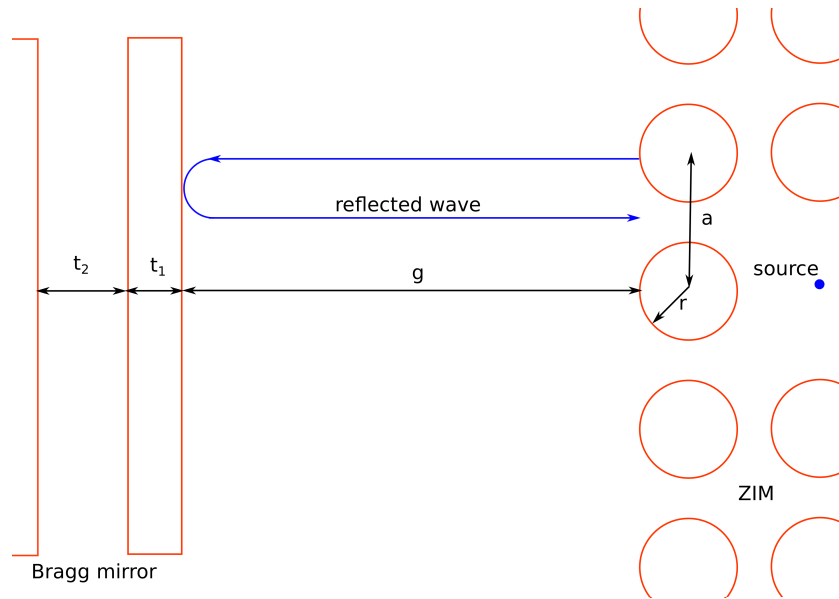


Figure 6.12: Schematic illustration of the design of the nanoantenna showing various geometrical parameters

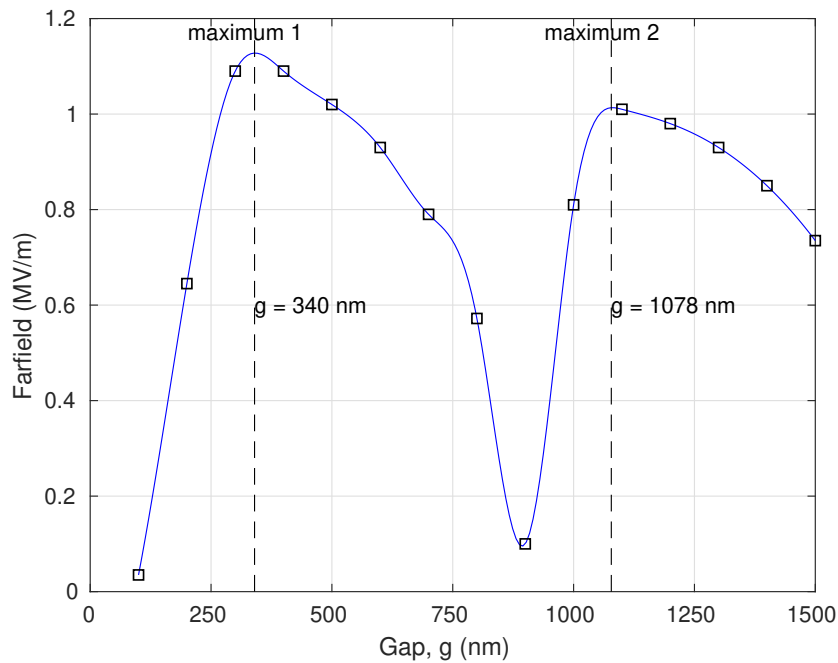


Figure 6.13: Variation of output field with respect to the gap parameter g

Table 6.1 shows the comparison between the values of g according to equation 6.12 and values obtained by numerical analysis shown in figure 6.13. It can be observed that numerically obtained positions of maxima are deviated by 47.5 nm and 77.5 nm respectively, from those predicted by equation 6.12. The reason for

Table 6.1: Values of gap parameter g corresponding to maximum output in the farfield zone

	maximum 1	maximum 2
Present case (Fig 6.12)	340 nm	1085 nm
Ideal case (Eq 6.12)	387.5 nm ($n = 1$)	1162.5 nm ($n = 2$)
Deviation	47.5 nm	77.5 nm

this deviation is the fact the reflector is made up of pure dielectric slabs which cannot offer a sharp perfectly reflecting boundary to the incoming radiation and a small amount of light is always able to slightly penetrate into the first layer. This imperfection leads to the discrepancy that actual gap value comes out to be slightly smaller than that in the ideal case.

6.8 Conclusion

Zero-index metamaterial based nanoantenna has been successfully designed and analyzed. It has been demonstrated that the proposed ZIM nanoantenna can unidirectionally radiate the electromagnetic radiation from an isotropic quantum emitter embedded in it. The proposed structure is simple and compatible with on-chip fabrication techniques. Although the nanoantenna is free from ohmic losses for being made up of dielectric, there will surely be some power dissipation in the parallel conductors. But on the bright side, this is more of an advantage than a limitation, because radiation losses along the z-direction are checked this way.

Chapter 7

All dielectric zero index metamaterial for TE/TM polarization

7.1 Introduction

THE zero index metamaterial used in the previous chapter is a very simple, easy to fabricate, low-loss option for any zero index application. However, despite all advantages, a major limitation of the structure is that it works only in TM mode. Recently, in 2017, Vulis et al. designed and fabricated a complementary structure, in which holes had been drilled in a dielectric slab, acting as a ZIM for TE polarization. The authors labeled it as a CMOS compatible ZIM. But this design was limited to TE polarization only and was nonfunctional in TM polarization. Hence, a structure which can be tuned to operate for both polarizations is seriously needed.

In this chapter, a novel design of ZIM has been proposed which can operate for both transverse magnetic (TM) and transverse electric (TE) polarization. The structure is basically an array of dielectric walls running parallel and perpendicular to each other, as shown in figure 7.1. The structure is commonly called dielectric vein type photonic crystal and unlike a square lattice of dielectric rods, it is a connected structure. Being a connected structure it allows both TM and TE mode to keep most of their energy confined in the high permittivity region [42]. Hence any of the two polarizations can be made to excite Mie resonance by suitably tuning the design parameters. The methods used in this work to demonstrate zero index behavior of the proposed design are – to calculate photonic band structures and seek for Dirac cones in them [43], to calculate effective material parameters by inversion of scattering parameters [89] and to calculate angle of refraction as light travels from ZIM to air.

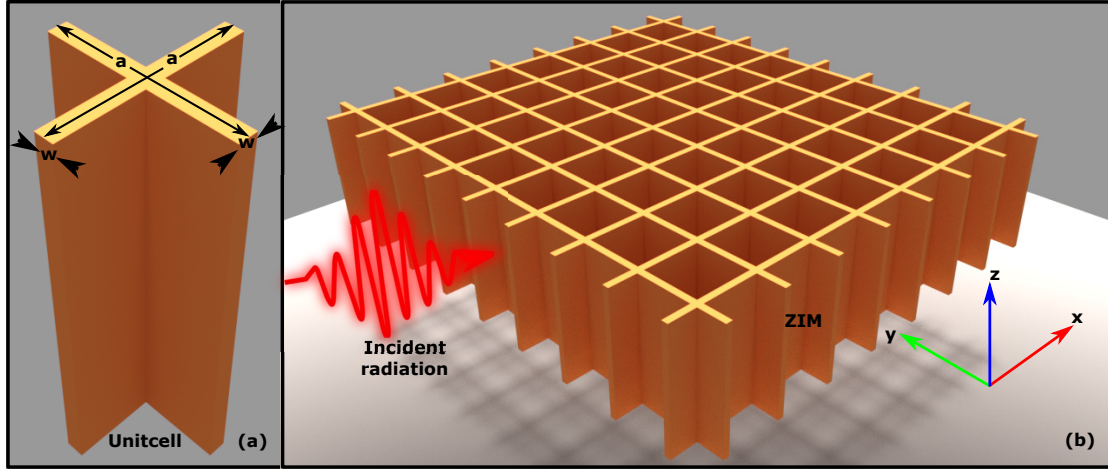


Figure 7.1: Design of the proposed metamaterial (a) Unitcell, (b) two dimensional array

7.2 Design and Numerical Analysis

While designing a ZIM, the choice of geometrical and material parameters play the most crucial role. Formation of Dirac-cone is a requisite for achievement of zero index behavior. The cone can not form for just any value of periodicity and vein width. One needs to carefully choose the vein width w and the periodicity a so that a well defined cone is formed in the photonic band structure. The dielectric used here is Silicon whose permittivity ϵ has been taken as 12.5 and desired wavelength (λ) of operation is $1.55\mu\text{m}$. The design of the proposed ZIM is shown in figure 7.1.

7.2.1 Calculation of band structure

A photonic band structure is a graphical representation of frequency eigenvalues at different wave vectors. It is calculated for both polarizations viz. transverse electric and transverse magnetic. A transverse magnetic (TM) mode has electric field normal to the plane of propagation ($\vec{E} = E(\rho)\hat{z}$) and magnetic field in the plane ($\vec{H}(\rho)\cdot\hat{z} = 0$) [42]. The TM band structure for the unit cell, shown in figure 7.1(a), was calculated for different values of w/a (width/periodicity) ratio using a plane wave expansion method based open-source software package called MIT Photonic Bands (MPB) [43]. It was found that a well-defined Dirac cone was achieved when $w = 0.22a$, $a = 0.40\lambda$ and where $\lambda = 1.55\mu\text{m}$. Figures 7.2(a) & (b) show the photonic band structure of the said geometrical parameters, in which, the bands number 3, 4 and 5 intersect each other at a triple degenerate Dirac point. In a different mode of representation in which the three dimensional dispersion surfaces are plotted, one gets a better visualization of the Dirac cone (see figure 7.2(c) & (d)).

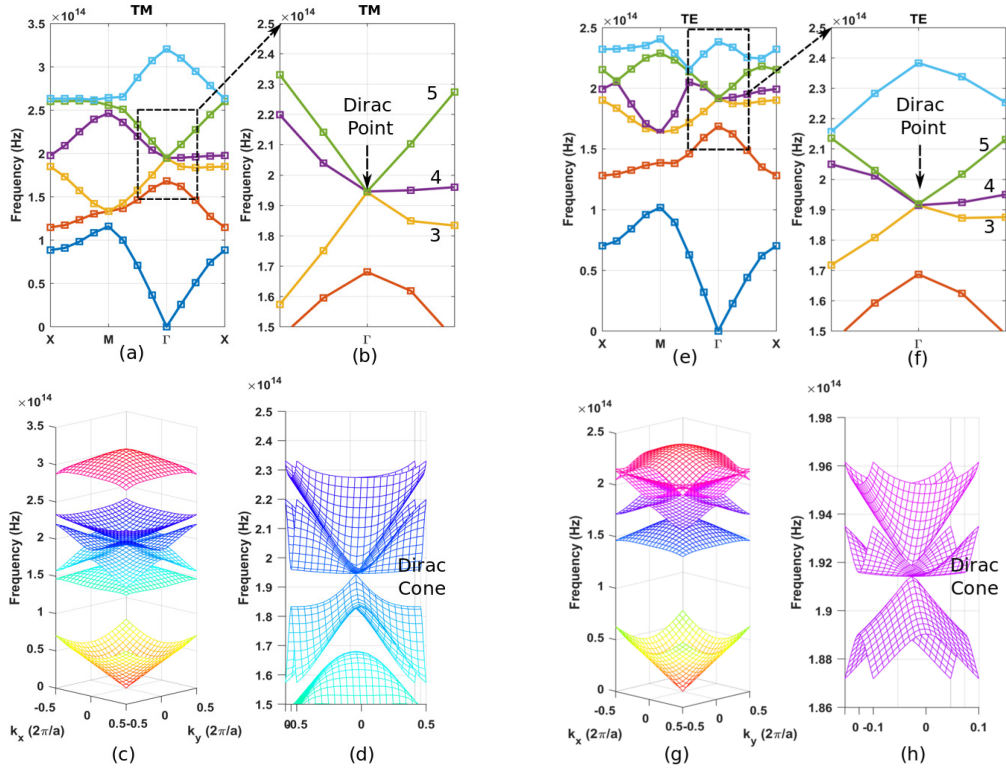


Figure 7.2: (a) TM mode Photonic band structure of proposed ZIM, (b) zoomed-in image of the band structure to get a better view of intersection of bands, (c) band structure in terms of 3D dispersion surfaces & (d) zoomed-in version of 3D surfaces of for closer look of the Dirac cone. (e)-(h) similar band plots for TE mode.

On the similar lines, photonic bands were also calculated for TE mode and a well defined Dirac cone was obtained at $w = 0.3a$ and $a = 0.46\lambda$. The plots for TE modes are shown in figure 7.2(e)-(h)

7.2.2 Interpretation of fields

The E_z and H_z field profiles corresponding to different bands at the Dirac point have been obtained for TM and TE polarization respectively and are shown in figure 7.3. In case of transverse magnetic polarization, the bands 3, 4 and 5 correspond to a transverse electric monopole, a longitudinal magnetic dipole and a transverse magnetic dipole respectively. To identify the transverse or longitudinal nature, the fields were calculated not at the exact center of the Brillouin zone but in its vicinity, where x component of the wavevector is extremely small $k_x = 0.01(2\pi/a)$ and y component is zero ($k_y = 0$). It can be noticed that while magnetic dipole of band 4 is aligned parallel to x-axis, its alignment is perpendicular in band 5. Hence, it is inferred that band 4 and 5 correspond to longitudinal dipole mode

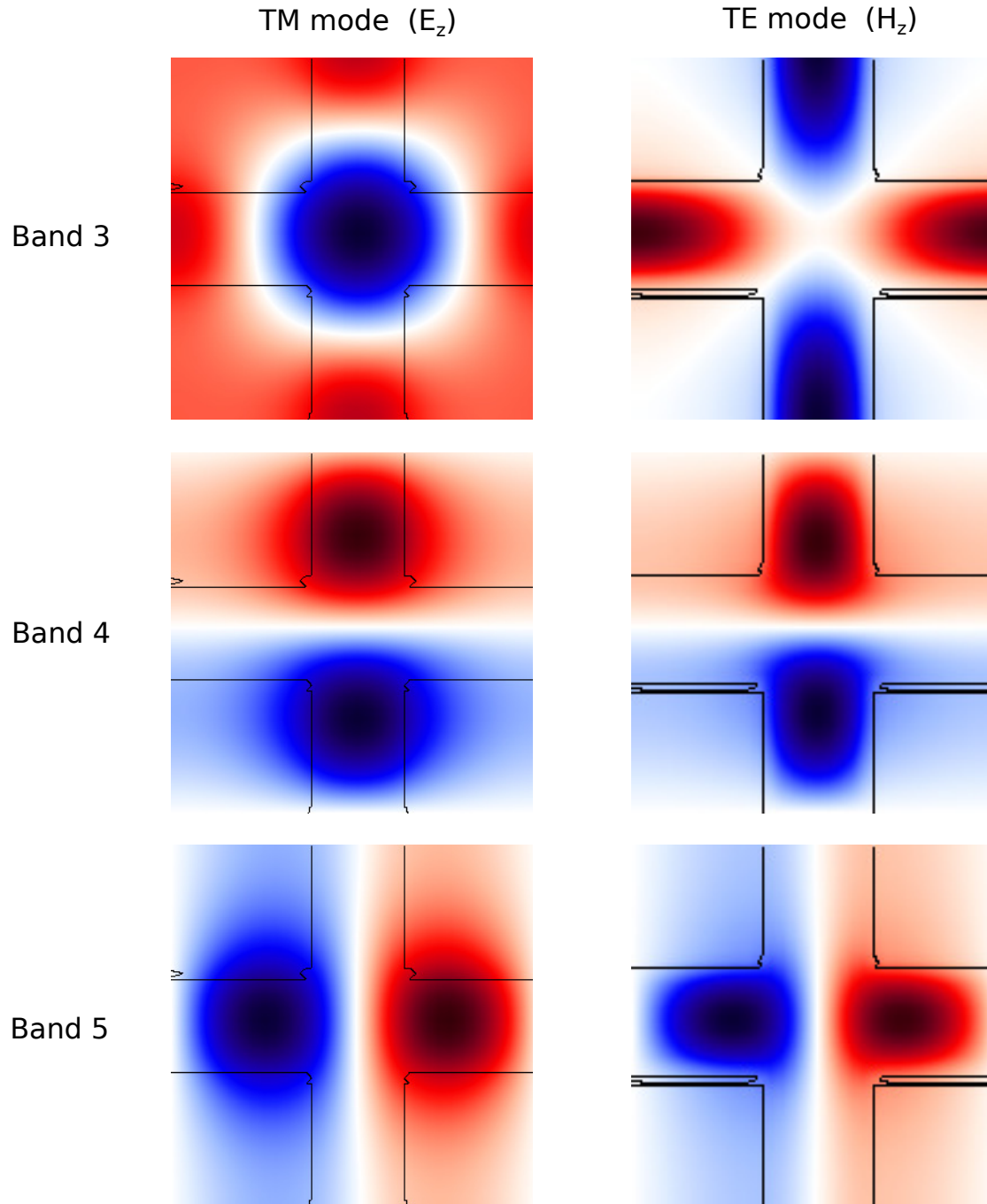


Figure 7.3: Distribution of normalized E_z and H_z at the triple degenerate Dirac point for TM and TE polarization respectively.

and transverse dipole mode respectively.

Similarly, for transverse electric polarization it has been identified that the field profiles of bands 3, 4 and 5 represent a magnetic quadrupole, a longitudinal electric dipole (flat band) and a transverse electric dipole respectively.

7.2.3 Calculation of effective parameters

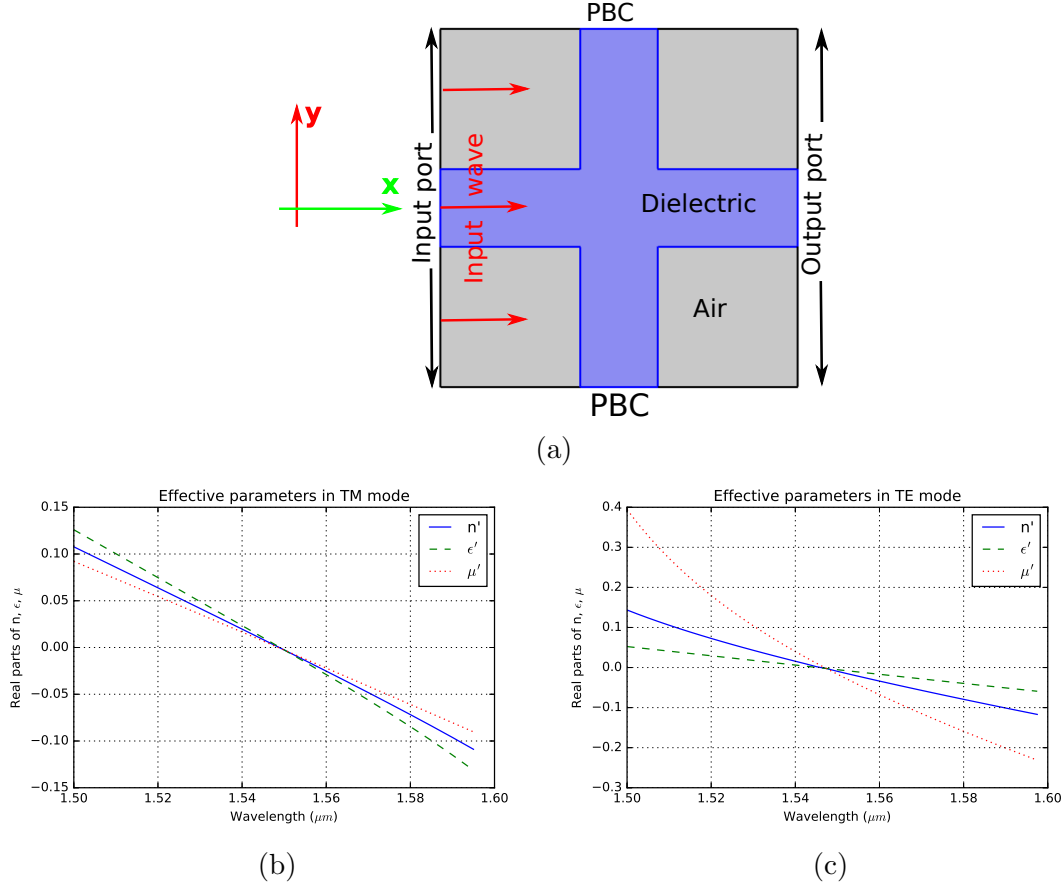


Figure 7.4: Calculation of effective material parameters by s-parameter inversion technique [89]. (a) Two dimensional unit cell used for s parameter calculation. Effective material parameters calculated for (a) TM and (b) TE polarizations. In both the cases ϵ , μ and n tend to zero at 1.55 μm .

Although the Dirac like dispersion is an indication of a zero-index system, it is necessary to confirm it by calculating the effective material parameters. The effective parameters – refractive index (n), permittivity (ϵ) and permeability (μ), have been retrieved by s-parameters inversion technique proposed by Smith et al. in 2005 [89]. Figure 7.4(a) shows the two dimensional unit cell whose boundaries were defined as illustrated. An electromagnetic wave of a specific polarization (E_z for TM and E_y for TE mode) is fed into the system from the input port and is collected at the output port. The other two boundaries have been assigned periodic boundary condition (PBC) to simulate the response of an array. The s-parameters data thus obtained has been used to determine effective parameters.

Since operating wavelength is not very large compared to the size of the unit cell, one may wonder whether it is possible to calculate effective parameters using

the above method. However, it should be noted that the zero index behavior is exhibited in the vicinity of the Dirac point at the center of the Brillouin zone where the wave vector is approximately zero, as a result, effective wavelength approaches infinity making it possible to accurately calculate the effective parameters. Figure 7.4(b) and (c) show the variation of effective material parameters with respect to wavelength for transverse magnetic and transverse electric polarizations respectively. It can be noticed that in both the cases ϵ , μ and n all approach zero simultaneously around 1550 nm.

7.2.4 Verification by Snell's Law

Although the above exercise proves the predicted zero refraction, for an additional confirmation it was examined whether the proposed structure satisfies the Snell's law or not. It can be comprehended that, for a wave traveling from ZIM to air,

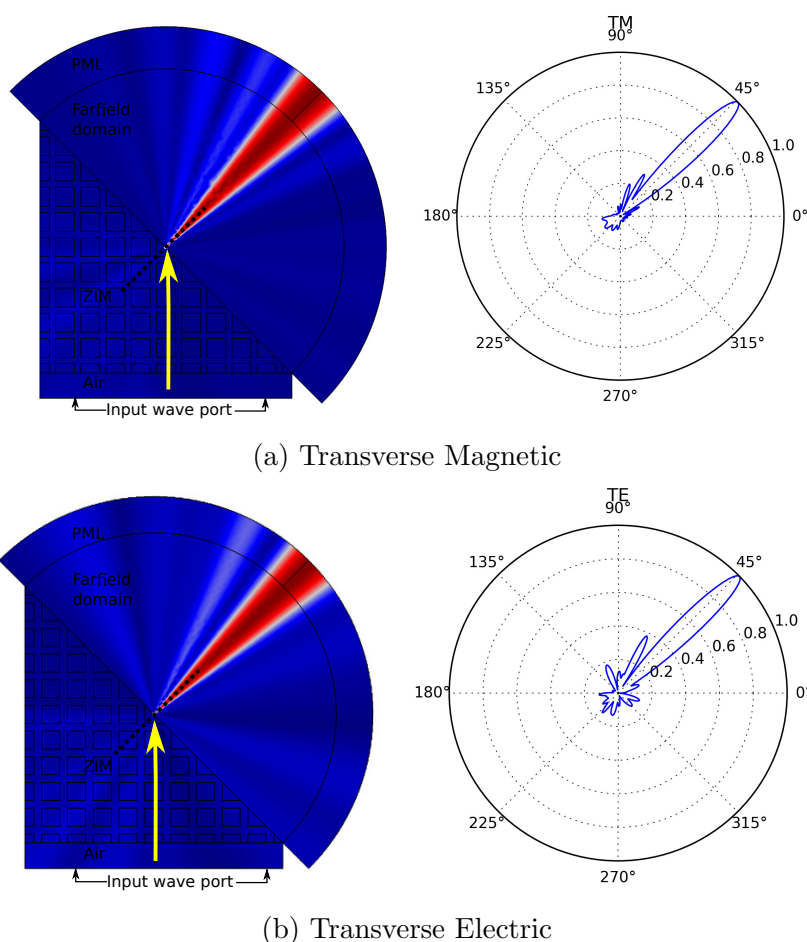


Figure 7.5: Demonstration of normal emergence of light from a prism of the proposed zero index metamaterial in TM and TE mode at $1.54 \mu\text{m}$

angle of refraction should be almost zero irrespective of the angle of incidence. For this analysis, two right-angled prisms of the ZIM (shown in figure 7.5) have been designed having respective geometrical features according to the polarization they are meant to operate for. Length of each of the two sides forming the right angle is $10a$. There is an air gap of width 385 nm between prism boundary and the input port. The hypotenuse acts as the interface between ZIM and air at which refraction takes place and the angle of incidence is 45° owing to the geometry of the prism. Farfield calculations show that angle of refraction is -1.1° and -1.7° for TM and TE mode respectively, which implies that, in both cases the wave emerges almost normally from the prism. This observation is a strong evidence in support of the claimed zero refraction.

7.3 Result and Discussion

It is a commonly known fact that in case of a square lattice of dielectric rods, the electric field vector lies mostly inside the dielectric in TM mode, but penetrates substantially into the air region in TE mode. Hence, it is easier to excite Mie resonance in rods in TM mode but not in TE mode. On the contrary, in holes-in-dielectric type structure TE modes are more strongly confined in the dielectric region than TM modes. Hence excitation of Mie resonance by TE polarized light is easier in holes-in-dielectric type structure. Consequently, the rods-in-air ZIM is appropriate for TM mode only, while the holes-in-dielectric type ZIM is more suitable for TE polarization. However, it has been shown in the above sections that the design proposed in this chapter is equally suitable for both polarizations. It is the specialty of the dielectric vein type structure that field can remain confined inside the dielectric region for both polarizations as it is a well-connected structure. The TM mode confines the field at crosses whereas the TE mode confines the field in veins without leaving the high permittivity region. As a result, Mie resonance can be excited by both the polarizations.

The proposed metamaterial can be fabricated by electron beam lithography and reactive ion etching technique [51, 47]. The fabricated metamaterial will have a finite height in z direction hence its response will certainly be different from 2D simulation results for TM mode. However, Li, et al. [51] suggested that such a structure with a finite height can pretend to be infinitely extended, if it is confined between two parallel conductors spread normal to z direction, making the enforcement of TM mode possible.

7.4 Conclusion

The novel design of an effectively zero-index metamaterial has been proposed. Compared to the other existing structures whose zero-index is limited to only one of two (TM or TE) polarizations, the proposed design can be tuned to work for

any of the two polarizations by appropriately choosing the design parameters. On top of that, the proposed design is mechanically more stable and easier to fabricate than the well-known rods-in-air type ZIM.

Chapter 8

Summary and future scope

Metamaterials kick-started a completely new branch of electrodynamics, which drew enormous attention from the scientific community due to their intriguing and extraordinary properties, which many times challenge the common sense. A broad spectrum of phenomena such as, negative refraction, electromagnetic cloaking, perfect reflection, perfect absorption, electromagnetic induced transparency, directional radiation, wavefront engineering, zero refraction, etc, have been investigated and reported by various research groups around the globe. This thesis presents a detailed account of the research work conducted by the author in the area of metamaterials which includes certain novel application specific designs, as well as, a few unanticipated applications of the existing designs of metamaterials. In chapter 2, a broad classification of metamaterials on the basis of dimensions, constituent material, resonance and refractive index have been presented, and it is claimed that all the metamaterial proposed or employed in this research work, fall in at least one of the mentioned categories.

The chapter 3 suggests a unique application of an existing design of metamaterial perfect reflector (reported by Moitra et al.), in designing a compact and high quality laser cavity. The quality factor of the proposed cavity has been found to be 5 times greater than a Bragg mirror based cavity, considered for comparison purposes. The reflectance of a single layer of the metamaterial (metasurface) is superior to 25 layers thick Bragg's mirror, which is the main reason behind its compactness and high quality factor. Since line-width is inversely proportional to quality factor [28], its higher value results in a reduced line-width and in improved monochromaticity. The proposed cavity design not just overcomes losses due to finite reflectivity, but is also free from ohmic loss due to pure dielectric nature of the metamaterial. This work, serving as a primordial design, can pave way for more sophisticated and compact laser cavities based on metamaterials.

In chapter 4, a novel design of negative refractive index metamaterial has been proposed which is based on an ingenious and a unique type of magnetic meta-atom, referred to as a *split-nanotube*. Split-nanotube is an elongated form of a split ring resonator (SRR), which inherits SRR's strong magnetic activity towards

axial magnetic field but subjugates its nanoscale fabrication impediments. By this metamaterial, refractive index as low as -2 has been achieved with a fairly good figure of merit (FOM) of 8. As it has already been discussed in chapter 2, that negative index metamaterial can facilitate subwavelength imaging by collecting evanescent waves, the imaging devices equipped with *metamaterial perfect lenses* can be possibly able to image a DNA, the internal processes of viruses and even biomolecules like proteins, in the near future.

In chapter 5, an absolutely unique type of metamaterial perfect absorber has been analyzed, which shows 99.9% absorbance at 88 μm and the absorbance remains more than 90% for the angle of incidence up to 55° . Unlike other contemporary absorbers which are based on plasmonic resonance, this absorber employs LiTaO_3 (a lossy dielectric) and utilizes Mie resonance to aid absorption, which makes it a broadband broad-angle device. The most significant application of the proposed metamaterial perfect absorber can be infrared imaging. On being paired with a thermal sensitive resistor, it can work as a broadband sensor for thermal imaging. Another probable future application of Mie resonance based metamaterial perfect absorbers can be in photovoltaics. The presently used solar cells are made up of silicon, which is a lossy dielectric in the visible region. Hence, it is worthwhile to investigate the possibility of enhancing the efficiency of photovoltaics, by means of a silicon based metamaterial perfect absorber of the proposed configuration.

The chapters 6 and 7 deal with a special class of metamaterials called the *zero index metamaterials (ZIM)*, which have gained popularity very recently. The chapter 6 presents a zero index metamaterial based highly directive nanoantenna for the on-chip nanoscale applications. The nanoantenna successfully transforms the radiation from an otherwise omnidirectional quantum emitter, into a unidirectional beam. This happens because of *no change in phase* property of the zero index metamaterial, which has been thoroughly discussed in chapter 6. The directivity as good as 8.28 dB in H-plane and 6.04 dB in E-plane has been achieved, which translates into 3 dB beamwidth of 45° in H plane and of 63° E plane. The work can be further extended by trying to couple the directive beams to nanoscale plasmonic or dielectric waveguides in all-optical nanoscale circuits. The ZIM employed in this work is a well known design proposed by Huang et al. in 2011, which has been chosen for it is free from resistive losses in spectrum of interest. However, a major drawback of the ZIM is that it is limited to the transverse magnetic (TM) polarization only and cannot function for the transverse electric (TE) polarization. This challenge has been successfully tackled in chapter 7, in which a novel design of an all-dielectric zero index metamaterial has been proposed, which can be tuned to operate in both – TM and TE polarizations by slight variation in the geometry. Besides operational flexibility, it also has a certain mechanical stability in comparison to Huang's rods in air type design. The applications of the zero index metamaterials can be as many as one can think of. A wonderful property of ZIM which may be cultivated into powerful defense technology of the future, is

electromagnetic cloaking. An electromagnetically cloaked combat aircraft or Unmanned Ariel Vehicle (UAV) can be of substantial tactical advantage by the virtue of being undetectable. Likewise, the phase preservation by ZIM can be beneficial for nonlinear applications where phase matching is a requisite. Hence, the work of chapter 7 can be extended to realization of nonlinear phenomena such as second harmonic generation, four wave mixing, electromagnetic switching, etc.

Mentioned above are a very few ambitious applications of the metamaterials envisioned for the future. Beside these, optical computing, wireless power transfer, holography, radiative sky cooling, field enhancement in magnetic resonance imaging (MRI), augmented reality, etc, are the areas where metamaterials can open numerous possibilities. Most of these technologies are presently in infancy, but are worthy of investigation and experimentation, because if accomplished, they can substantially enhance the state of the art of the current technology. For instance, a revolutionary application can be the *radiative sky cooling*. Radiative sky cooling means cooling down of a sky-facing object by radiative transfer of heat into the universe, which remains at an ambient temperature of at 4 K like an infinite and eternal heat sink. This process happens naturally at night but is not possible during the day because of solar radiation. The earth whose ambient temperature is 300 K, acts as a heat sink for the sun whose surface temperature is around 6000 K. Radiation peak of the solar radiation lies at $\approx 0.5\mu\text{m}$, while that for the earth's radiations fall in range $8 - 13 \mu\text{m}$. Hence a metamaterial panel which reflects back the solar radiation but allows transmission of the earth's heat rays into the universe, can make the process of radiative cooling possible during the daytime as well. This technique can help in keeping the sophisticated outdoor electronic equipments cool, specially in equatorial regions. This is a very attractive application, which may be beneficial to the communication industry. Besides communication systems, metamaterials can be useful in healthcare and medicine too. For example, the usage of metamaterial field enhancers can generate high contrast magnetic resonance images allowing detection of minute imperfections, so that, any ailment can be handled in very early stage, before it gets too complicated to be cured.

Though all these possibilities are very promising, one aspect that needs to be kept in mind during their development is the cost-effectiveness. A wonderful technology can only be beneficial to the society, if it can be commercialized. Hence, the design and development technique should be such, that it allows the large scale production of the device. In light of all the research work presented in this thesis, and the above discussion, it is stated that metamaterials hold a tremendous scope for future development.

Bibliography

- [1] Andrea Alu, Mário G Silveirinha, Alessandro Salandrino, and Nader Engheta. Epsilon-near-zero metamaterials and electromagnetic sources: Tailoring the radiation phase pattern. *Physical review B*, 75(15):155410, 2007.
- [2] Amir Arbabi, Ryan M Briggs, Yu Horie, Mahmood Bagheri, and Andrei Faraon. Efficient dielectric metasurface collimating lenses for mid-infrared quantum cascade lasers. *Optics Express*, 23(26):33310–33317, 2015.
- [3] Amir Arbabi, Yu Horie, Mahmood Bagheri, and Andrei Faraon. Dielectric metasurfaces for complete control of phase and polarization with subwavelength spatial resolution and high transmission. *Nature Nanotechnology*, 10:937–943, 2015.
- [4] Amir Arbabi, Yu Horie, Alexander J Ball, Mahmood Bagheri, and Andrei Faraon. Subwavelength-thick lenses with high numerical apertures and large efficiency based on high-contrast transmitarrays. *Nature communications*, 6, 2015.
- [5] Koray Aydin, Kaan Guven, Nikos Katsarakis, Costas M Soukoulis, and Ekmel Ozbay. Effect of disorder on magnetic resonance band gap of split-ring resonator structures. *Optics Express*, 12(24):5896–5901, 2004.
- [6] Juan D Baena, Ricardo Marqués, Francisco Medina, and Jesús Martel. Artificial magnetic metamaterial design by using spiral resonators. *Physical review B*, 69(1):014402, 2004.
- [7] Reuben M Bakker, Dmitry Permyakov, Ye Feng Yu, Dmitry Markovich, Ramón Paniagua-Domínguez, Leonard Gonzaga, Anton Samusev, Yuri Kivshar, Boris Lukyanchuk, and Arseniy I Kuznetsov. Magnetic and electric hotspots with silicon nanodimers. *Nano Letters*, 15(3):2137–2142, 2015.
- [8] PR Berman. Goos-hänchen shift in negatively refractive media. *Physical Review E*, 66(6):067603, 2002.
- [9] Craig F Bohren and Donald R Huffman. *Absorption and scattering of light by small particles*. John Wiley & Sons, 2008.

- [10] Nicolas Bonod. Silicon photonics: Large-scale dielectric metasurfaces. *Nature materials*, 14(7):664–665, 2015.
- [11] Robert W Boyd. *Nonlinear optics*. Academic press, 2003.
- [12] Wenshan Cai, Uday K Chettiar, Hsiao-Kuan Yuan, Vashista C de Silva, Alexander V Kildishev, Vladimir P Drachev, and Vladimir M Shalaev. Metamagnetics with rainbow colors. *Optics express*, 15(6):3333–3341, 2007.
- [13] Wenshan Cai and Vladimir M Shalaev. *Optical metamaterials*, volume 10. Springer, 2010.
- [14] Martín Caldarola, Pablo Albella, Emiliano Cortés, Mohsen Rahmani, Tyler Roschuk, Gustavo Grinblat, Rupert F Oulton, Andrea V Bragas, and Stefan A Maier. Non-plasmonic nanoantennas for surface enhanced spectroscopies with ultra-low heat conversion. *Nature Communications*, 6:7915, 2015.
- [15] Antonio Capretti, Yu Wang, Nader Engheta, and Luca Dal Negro. Comparative study of second-harmonic generation from epsilon-near-zero indium tin oxide and titanium nitride nanolayers excited in the near-infrared spectral range. *Acs Photonics*, 2(11):1584–1591, 2015.
- [16] Antonio Capretti, Yu Wang, Nader Engheta, and Luca Dal Negro. Enhanced third-harmonic generation in si-compatible epsilon-near-zero indium tin oxide nanolayers. *Optics letters*, 40(7):1500–1503, 2015.
- [17] Bybi P Chacko, Gijo Augustin, and Tayeb A Denidni. A high-gain antenna based on zero-index metamaterial superstrate. In *Antennas and Propagation Society International Symposium (APSURSI), 2013 IEEE*, pages 122–123. IEEE, 2013.
- [18] Jierong Cheng, Davood Ansari-Oghol-Beig, and Hossein Mosallaei. Wave manipulation with designer dielectric metasurfaces. *Optics Letters*, 39(21):6285–6288, 2014.
- [19] W Dallenbach and W Kleinstaub. Reflection and absorption of decimeter-waves by plane dielectric layers. *Hochfreq. u Elektroak*, 51:152–156, 1938.
- [20] Manuel Decker, Isabelle Staude, Matthias Falkner, Jason Dominguez, Dragomir N Neshev, Igal Brener, Thomas Pertsch, and Yuri S Kivshar. High-efficiency dielectric huygens’ surfaces. *Advanced Optical Materials*, 3(6):813–820, 2015.
- [21] Ricardo A Depine and Akhlesh Lakhtakia. A new condition to identify isotropic dielectric-magnetic materials displaying negative phase velocity. *Microw. Opt. Technol. Lett.*, 41, 2004.

- [22] Pavel A. Dmitriev, Denis G. Baranov, Valentin A. Milichko, Sergey V. Makarov, Ivan S. Mukhin, Anton K. Samusev, Alexander E. Krasnok, Pavel A. Belov, and Yuri S. Kivshar. Resonant raman scattering from silicon nanoparticles enhanced by magnetic response. *Nanoscale*, 8:9721–9726, 2016.
- [23] Gunnar Dolling, Christian Enkrich, Martin Wegener, Costas M Soukoulis, and Stefan Linden. Low-loss negative-index metamaterial at telecommunication wavelengths. *Optics letters*, 31(12):1800–1802, 2006.
- [24] Stefan Enoch, Gérard Tayeb, Pierre Sabouroux, Nicolas Guérin, and Patrick Vincent. A metamaterial for directive emission. *Physical Review Letters*, 89(21):213902, 2002.
- [25] Andrey B Evlyukhin, Sergey M Novikov, Urs Zywiets, Rene? Lyng Eriksen, Carsten Reinhardt, Sergey I Bozhevolnyi, and Boris N Chichkov. Demonstration of magnetic dipole resonances of dielectric nanospheres in the visible region. *Nano Letters*, 12(7):3749–3755, 2012.
- [26] Aitzol García-Etxarri, R Gómez-Medina, Luis S Froufe-Pérez, Cefe López, L Chantada, Frank Scheffold, J Aizpurua, M Nieto-Vesperinas, and Juan José Sáenz. Strong magnetic response of submicron silicon particles in the infrared. *Optics Express*, 19(6):4815–4826, 2011.
- [27] Andre K Geim and Konstantin S Novoselov. The rise of graphene. *Nature materials*, 6(3):183, 2007.
- [28] Ajoy Kumar Ghatak and K Thyagarajan. *Optical electronics*. Cambridge University Press, 1989.
- [29] Fritz Goos and H Hänchen. Ein neuer und fundamentaler versuch zur total-reflexion. *Annalen der Physik*, 436(7-8):333–346, 1947.
- [30] David J Griffiths. *Introduction to electrodynamics*. AAPT, 2005.
- [31] Hongcang Guo, Na Liu, Liwei Fu, Heinz Schweizer, Stefan Kaiser, and Harald Giessen. Thickness dependence of the optical properties of split-ring resonator metamaterials. *physica status solidi (b)*, 244(4):1256–1261, 2007.
- [32] Philipp Gutruf, Chengjun Zou, Withawat Withayachumnankul, Madhu Bhaskaran, Sharath Sriram, and Christophe Fumeaux. Mechanically tunable dielectric resonator metasurfaces at visible frequencies. *ACS Nano*, 10(1):133–141, 2015.
- [33] Jiaming Hao, Jing Wang, Xianliang Liu, Willie J Padilla, Lei Zhou, and Min Qiu. High performance optical absorber based on a plasmonic metamaterial. *Applied Physics Letters*, 96(25):251104, 2010.

- [34] Jiaming Hao, Wei Yan, and Min Qiu. Super-reflection and cloaking based on zero index metamaterial. *Applied Physics Letters*, 96(10):101109, 2010.
- [35] WN Hardy and LA Whitehead. Split-ring resonator for use in magnetic resonance from 200–2000 mhz. *Review of Scientific Instruments*, 52(2):213–216, 1981.
- [36] Christopher L Holloway, Edward F Kuester, Joshua A Gordon, John O Hara, Jim Booth, and David R Smith. An overview of the theory and applications of metasurfaces: The two-dimensional equivalents of metamaterials. *Antennas and Propagation Magazine, IEEE*, 54(2):10–35, 2012.
- [37] Xueqin Huang, Yun Lai, Zhi Hong Hang, Huihuo Zheng, and CT Chan. Dirac cones induced by accidental degeneracy in photonic crystals and zero-refractive-index materials. *Nature materials*, 10(8):582, 2011.
- [38] Saman Jahani and Zubin Jacob. All-dielectric metamaterials. *Nature Nanotechnology*, 11(1):23–36, 2016.
- [39] B Jensen and A Torabi. Refractive index of quaternary in1- xgaxasy1- y lattice matched to inp. *Journal of applied physics*, 54(6):3623–3625, 1983.
- [40] Zhi Hao Jiang, Qi Wu, Donovan E Brocker, Peter E Sieber, and Douglas H Werner. A low-profile high-gain substrate-integrated waveguide slot antenna enabled by an ultrathin anisotropic zero-index metamaterial coating. *IEEE Transactions on Antennas and Propagation*, 62(3):1173–1184, 2014.
- [41] Jian-Ming Jin. *The finite element method in electromagnetics*. John Wiley & Sons, 2015.
- [42] John D Joannopoulos, Steven G Johnson, Joshua N Winn, and Robert D Meade. *Photonic crystals: molding the flow of light*. Princeton university press, 2011.
- [43] Steven G Johnson and JD Joannopoulos. The mit photonic-bands package. *from Internet Homepage <http://abinitio.mit.edu/mpb>*, 2008.
- [44] MI Katsnelson. Zitterbewegung, chirality, and minimal conductivity in graphene. *The European Physical Journal B-Condensed Matter and Complex Systems*, 51(2):157–160, 2006.
- [45] Alexander V Kildishev, Alexandra Boltasseva, and Vladimir M Shalaev. Planar photonics with metasurfaces. *Science*, 339(6125):1232009, 2013.
- [46] Kamal Kishor, Monu Nath Baitha, RK Sinha, and Basudev Lahiri. Tunable negative refractive index metamaterial from v-shaped srr structure: fabrication and characterization. *JOSA B*, 31(7):1410–1414, 2014.

- [47] Shota Kita, Yang Li, Philip Camayd-Muñoz, Orad Reshef, Daryl I Vulis, Robert W Day, Eric Mazur, and Marko Lončar. On-chip all-dielectric fabrication-tolerant zero-index metamaterials. *Optics Express*, 25(7):8326–8334, 2017.
- [48] Aleksandr E Krasnok, Ivan S Maksymov, Andrei I Denisyuk, Pavel Alexandrovich Belov, Andrei E Miroschnichenko, Constantin R Simovski, and Yu S Kivshar. Optical nanoantennas. *Physics-Uspekhi*, 56(6):539, 2013.
- [49] Alexander Krasnok, Sergey Makarov, Mikhail Petrov, Roman Savelev, Pavel Belov, and Yuri Kivshar. Towards all-dielectric metamaterials and nanophotonics. *Proceedings SPIE 9502, Metamaterials X*, 9502:950203, 2015.
- [50] Lev Davidovich Landau, LP Pitaevskii, and EM Lifshitz. *Electrodynamics of continuous media*. Pergamon Press, 1984.
- [51] Sergey V Li, Denis G Baranov, Alexander E Krasnok, and Pavel A Belov. All-dielectric nanoantennas for unidirectional excitation of electromagnetic guided modes. *Applied Physics Letters*, 107(17):171101, 2015.
- [52] Yang Li, Shota Kita, Philip Muñoz, Orad Reshef, Daryl I Vulis, Mei Yin, Marko Lončar, and Eric Mazur. On-chip zero-index metamaterials. *Nature Photonics*, 9(11):738, 2015.
- [53] Iñigo Liberal and Nader Engheta. Near-zero refractive index photonics. *Nature Photonics*, 11(3):149, 2017.
- [54] Dianmin Lin, Pengyu Fan, Erez Hasman, and Mark L Brongersma. Dielectric gradient metasurface optical elements. *Science*, 345(6194):298–302, 2014.
- [55] Stefan Linden, Christian Enkrich, Martin Wegener, Jiangfeng Zhou, Thomas Koschny, and Costas M Soukoulis. Magnetic response of metamaterials at 100 terahertz. *Science*, 306(5700):1351–1353, 2004.
- [56] Ruopeng Liu, Qiang Cheng, Thomas Hand, Jack J Mock, Tie Jun Cui, Steven A Cummer, and David R Smith. Experimental demonstration of electromagnetic tunneling through an epsilon-near-zero metamaterial at microwave frequencies. *Physical review letters*, 100(2):023903, 2008.
- [57] Yahong Liu, Xiaojing Guo, Shuai Gu, and Xiaopeng Zhao. Zero index metamaterial for designing high-gain patch antenna. *International Journal of Antennas and Propagation*, 2013, 2013.
- [58] Nadia Mattiucci, Mark J Bloemer, and Giuseppe D’Aguanno. Phase-matched second harmonic generation at the dirac point of a 2-d photonic crystal. *Optics Express*, 22(6):6381–6390, 2014.

- [59] Andrey E Miroshnichenko, Andrey B Evlyukhin, Ye Feng Yu, Reuben M Bakker, Arkadi Chipouline, Arseniy I Kuznetsov, Boris Lukyanchuk, Boris N Chichkov, and Yuri S Kivshar. Nonradiating anapole modes in dielectric nanoparticles. *Nature Communications*, 6:8069, 2015.
- [60] Parikshit Moitra, Brian A Slovick, Wei Li, Ivan I Kravchenko, Dayrl P Briggs, S Krishnamurthy, and Jason Valentine. Large-scale all-dielectric metamaterial perfect reflectors. *ACS Photonics*, 2(6):692–698, 2015.
- [61] Parikshit Moitra, Brian A Slovick, Zhi Gang Yu, S Krishnamurthy, and Jason Valentine. Experimental demonstration of a broadband all-dielectric metamaterial perfect reflector. *Applied Physics Letters*, 104(17):171102, 2014.
- [62] Parikshit Moitra, Yuanmu Yang, Zachary Anderson, Ivan I Kravchenko, Dayrl P Briggs, and Jason Valentine. Realization of an all-dielectric zero-index optical metamaterial. *Nature Photonics*, 7(10):791, 2013.
- [63] Edward D Palik. *Handbook of optical constants of solids*, volume 3. Academic press, 1998.
- [64] Or Peleg, Guy Bartal, Barak Freedman, Ofer Manela, Mordechai Segev, and Demetrios N Christodoulides. Conical diffraction and gap solitons in honeycomb photonic lattices. *Physical review letters*, 98(10):103901, 2007.
- [65] John B Pendry, A J_ Holden, DJ Robbins, and WJ Stewart. Magnetism from conductors and enhanced nonlinear phenomena. *IEEE transactions on microwave theory and techniques*, 47(11):2075–2084, 1999.
- [66] John B Pendry, AJ Holden, DJ Robbins, and WJ Stewart. Low frequency plasmons in thin-wire structures. *Journal of Physics: Condensed Matter*, 10(22):4785, 1998.
- [67] John B Pendry, AJ Holden, WJ Stewart, and I Youngs. Extremely low frequency plasmons in metallic mesostructures. *Physical review letters*, 76(25):4773, 1996.
- [68] Bogdan-Ioan Popa and Steven A Cummer. Compact dielectric particles as a building block for low-loss magnetic metamaterials. *Physical Review Letters*, 100(20):207401, 2008.
- [69] David Pozar. Scattered and absorbed powers in receiving antennas. *IEEE Antennas and Propagation Magazine*, 46(1):144–145, 2004.
- [70] S Anantha Ramakrishna. Physics of negative refractive index materials. *Reports on progress in physics*, 68(2):449, 2005.

- [71] Y Ra'Di, CR Simovski, and SA Tretyakov. Thin perfect absorbers for electromagnetic waves: theory, design, and realizations. *Physical Review Applied*, 3(3):037001, 2015.
- [72] Carsten Rockstuhl, Christoph Menzel, Thomas Paul, Thomas Pertsch, and Falk Lederer. Light propagation in a fishnet metamaterial. *Physical Review B*, 78(15):155102, 2008.
- [73] Walter Rotman. Plasma simulation by artificial dielectrics and parallel-plate media. *IRE Transactions on Antennas and Propagation*, 10(1):82–95, 1962.
- [74] Matthew NO Sadiku. *Numerical techniques in electromagnetics with MATLAB*. CRC press, 2018.
- [75] Kazuaki Sakoda. Dirac cone in two-and three-dimensional metamaterials. *Optics Express*, 20(4):3898–3917, 2012.
- [76] CM Saleh, D Bensafieddine, EM Laamari, and M Bouzouad. A zero-index metamaterial single layer superstrate for patch antenna gain enhancement. *Acta Physica Polonica A*, 128(2B), 2015.
- [77] Winfield W Salisbury. Absorbent body for electromagnetic waves, June 10 1952. US Patent 2,599,944.
- [78] Jurgen Sautter, Isabelle Staude, Manuel Decker, Evgenia Rusak, Dragomir N Neshev, Igal Brener, and Yuri S Kivshar. Active tuning of all-dielectric metasurfaces. *ACS Nano*, 9(4):4308–4315, 2015.
- [79] EF Schubert, Jong Kyu Kim, and J-Q Xi. Low-refractive-index materials: A new class of optical thin-film materials. *physica status solidi (b)*, 244(8):3002–3008, 2007.
- [80] Martin F Schubert, J-Q Xi, Jong Kyu Kim, and E Fred Schubert. Distributed bragg reflector consisting of high-and low-refractive-index thin film layers made of the same material. *Applied physics letters*, 90(14):141115, 2007.
- [81] John M Senior and M Yousif Jamro. *Optical fiber communications: principles and practice*. Pearson Education, 2009.
- [82] RA Sepkhanov, Ya B Bazaliy, and CWJ Beenakker. Extremal transmission at the dirac point of a photonic band structure. *Physical Review A*, 75(6):063813, 2007.
- [83] Mikhail I Shalaev, Jingbo Sun, Alexander Tsukernik, Apra Pandey, Kirill Nikolskiy, and Natalia M Litchinitser. High-efficiency all-dielectric metasurfaces for ultracompact beam manipulation in transmission mode. *Nano Letters*, 15(9):6261–6266, 2015.

- [84] Richard A Shelby, David R Smith, and Seldon Schultz. Experimental verification of a negative index of refraction. *science*, 292(5514):77–79, 2001.
- [85] Brian Slovick, Zhi Gang Yu, Marcy Berding, and Srini Krishnamurthy. Perfect dielectric-metamaterial reflector. *Physical Review B*, 88(16):165116, 2013.
- [86] David R Smith, Willie J Padilla, DC Vier, Syrus C Nemat-Nasser, and Seldon Schultz. Composite medium with simultaneously negative permeability and permittivity. *Physical review letters*, 84(18):4184, 2000.
- [87] David R. Smith and John B. Pendry. Homogenization of metamaterials by field averaging. *Journal of Optical Society of America B*, 23(3):391–402, 2006.
- [88] David R Smith, John B Pendry, and Mike CK Wiltshire. Metamaterials and negative refractive index. *Science*, 305(5685):788–792, 2004.
- [89] DR Smith, DC Vier, Th Koschny, and CM Soukoulis. Electromagnetic parameter retrieval from inhomogeneous metamaterials. *Physical review E*, 71(3):036617, 2005.
- [90] Haim Suchowski, Kevin O’Brien, Zi Jing Wong, Alessandro Salandrino, Xiaobo Yin, and Xiang Zhang. Phase mismatch-free nonlinear propagation in optical zero-index materials. *Science*, 342(6163):1223–1226, 2013.
- [91] Mei Sun, Zhi Ning Chen, and Xianming Qing. Gain enhancement of 60-ghz antipodal tapered slot antenna using zero-index metamaterial. *IEEE Transactions on Antennas and Propagation*, 61(4):1741–1746, 2013.
- [92] O Sydoruk, E Tatartschuk, E Shamonina, and L Solymar. Analytical formulation for the resonant frequency of split rings. *Journal of Applied Physics*, 105(1):014903, 2009.
- [93] Zsolt Szabo, Gi-Ho Park, Ravi Hedge, and Er-Ping Li. A unique extraction of metamaterial parameters based on kramers–kronig relationship. *IEEE Transactions on Microwave Theory and Techniques*, 58(10):2646–2653, 2010.
- [94] Allen Taflove and Susan C Hagness. *Computational electrodynamics: the finite-difference time-domain method*. Artech house, 2005.
- [95] Burak Temelkuran, Mehmet Bayindir, Ekmel Ozbay, Rana Biswas, MM Sigalas, Gary Tuttle, and Kai-Ming Ho. Photonic crystal-based resonant antenna with a very high directivity. *Journal of applied physics*, 87(1):603–605, 2000.

- [96] Jeremiah P Turpin, Qi Wu, Douglas H Werner, Bonnie Martin, Matt Bray, and Erik Lier. Near-zero-index metamaterial lens combined with amc meta-surface for high-directivity low-profile antennas. *IEEE Transactions on Antennas and Propagation*, 62(4):1928–1936, 2014.
- [97] Mohammad Habib Ullah, Mohammad Tariqul Islam, and Mohammad Rashed Iqbal Faruque. A near-zero refractive index meta-surface structure for antenna performance improvement. *Materials*, 6(11):5058–5068, 2013.
- [98] Jason Valentine, Shuang Zhang, Thomas Zentgraf, and Xiang Zhang. Development of bulk optical negative index fishnet metamaterials: Achieving a low-loss and broadband response through coupling. *Proceedings of the IEEE*, 99(10):1682–1690, 2011.
- [99] Viktor G Veselago. The electrodynamics of substances with simultaneously negative values of ϵ and μ . *Soviet Physics Uspekhi*, 10(4):509, 1968.
- [100] Li-Gang Wang, Zhi-Guo Wang, Jun-Xiang Zhang, and Shi-Yao Zhu. Realization of dirac point with double cones in optics. *Optics letters*, 34(10):1510–1512, 2009.
- [101] Mark S Wheeler, J Stewart Aitchison, and Mohammad Mojahedi. Coated nonmagnetic spheres with a negative index of refraction at infrared frequencies. *Physical Review B*, 73(4):045105, 2006.
- [102] J-Q Xi, Martin F Schubert, Jong Kyu Kim, E Fred Schubert, Minfeng Chen, Shawn-Yu Lin, Wayne Liu, and Joe A Smart. Optical thin-film materials with low refractive index for broadband elimination of fresnel reflection. *Nature photonics*, 1(3):176, 2007.
- [103] Yuanmu Yang, Ivan I Kravchenko, Dayrl P Briggs, and Jason Valentine. All-dielectric metasurface analogue of electromagnetically induced transparency. *Nature Communications*, 5:5753, 2014.
- [104] Ta-Jen Yen, WJ Padilla, Nicholas Fang, DC Vier, DR Smith, JB Pendry, DN Basov, and Xiang Zhang. Terahertz magnetic response from artificial materials. *Science*, 303(5663):1494–1496, 2004.
- [105] Nanfang Yu and Federico Capasso. Flat optics with designer metasurfaces. *Nature Materials*, 13(2):139–150, 2014.
- [106] Ye Feng Yu, Alexander Y Zhu, Ramón Paniagua-Domínguez, Yuan Hsing Fu, Boris Luk'yanchuk, and Arseniy I Kuznetsov. High-transmission dielectric metasurface with 2π phase control at visible wavelengths. *Laser & Photonics Reviews*, 9(4):412–418, 2015.

- [107] Hsiao-Kuan Yuan, Uday K Chettiar, Wenshan Cai, Alexander V Kildishev, Alexandra Boltasseva, Vladimir P Drachev, and Vladimir M Shalaev. A negative permeability material at red light. *Optics Express*, 15(3):1076–1083, 2007.
- [108] Qian Zhao, Ji Zhou, Fuli Zhang, and Didier Lippens. Mie resonance-based dielectric metamaterials. *Materials Today*, 12(12):60–69, 2009.
- [109] Bin Zhou and Tie Jun Cui. Directivity enhancement to vivaldi antennas using compactly anisotropic zero-index metamaterials. *IEEE Antennas and Wireless Propagation Letters*, 10:326–329, 2011.
- [110] Hang Zhou, Zhibin Pei, Shaobo Qu, Song Zhang, Jiafu Wang, Zhangshan Duan, Hua Ma, and Zhuo Xu. A novel high-directivity microstrip patch antenna based on zero-index metamaterial. *IEEE Antennas and wireless propagation letters*, 8:538–541, 2009.
- [111] Jingtao Zhu, Guanghua Lu, Jianlin Zhang, and Bo Li. Gain enhancement for planar quasi-yagi antenna with zero-index metamaterial. In *Microwave and Millimeter Wave Technology (ICMMT), 2016 IEEE International Conference on*, volume 2, pages 549–551. IEEE, 2016.

Author's Bio-data

NISHANT SHANKHWAR

AFFILIATION

TIFAC-Centre of Relevance and Excellence in Fiber Optics and Optical Communication, Department of Applied Physics, Delhi Technological University, Shahbad Daultapur, Main Bawana Road Delhi, 110042 INDIA

PERMANENT ADDRESS

2156, Shora Kothi, Subzi Mandi, Delhi, 110007 INDIA

PHONE: +91-9971403768

E-MAIL: nishant.shankhwar@gmail.com

EDUCATION

- M.Sc. in Electronics, 2013, University of Delhi.
- B.Sc.(Hons) in Electronic Science, 2011, University of Delhi

AREAS OF INTEREST

- Photonic Crystals, Plasmonics and Metamaterials
- Fiber Optics and Optical Communication
- Computational Electrodynamics
- Network analysis and Circuit Theory
- Semiconductors and Solid State Physics
- Quantum Electrodynamics

COMPUTATIONAL SKILLS

- **Programming Languages Known:** Proficiency in MATLAB and basic knowledge of C, FORTRAN and Python.
- **Computational Methods Known:** Finite Difference Time Domain Method, Finite Element Method, Transfer Matrix Method, Fast Fourier Transform Algorithm.
- **Computational and Designing Tools Known:** MEEP (MIT's open-source FDTD program), COMSOL Multiphysics, Ansys HFSS, Blender3D, Inkscape.

PROFESSIONAL SOCIETY MEMBERSHIP

- SPIE - The international society of optics and photonics
- OSA - The Optical Society

AWARDS/ FELLOWSHIPS

- UGC NET – Junior Research Fellowship (DEC- 2013).
- SPIE Officer Travel Grant to participate in Optics and Photonics 2017 at San Diego, USA.

NUMBER OF PUBLICATIONS

- **International Journals:** 5
- **International Conferences:** 23

INTERNET FOOTPRINT

- **Google scholar profile:**
<https://scholar.google.co.in/citations?user=5X9WyfMAAAAJ&hl=en&oi=ao>
- **Youtube channel:**
<https://www.youtube.com/channel/UCFPkI4p4ONJKQ170TI614pw/videos>